

2008

Joint super-resolution and scene-based nonuniformity correction using maximum a posteriori estimation

Douglas R. Droege
University of Dayton

Follow this and additional works at: https://ecommons.udayton.edu/graduate_theses

Recommended Citation

Droege, Douglas R., "Joint super-resolution and scene-based nonuniformity correction using maximum a posteriori estimation" (2008). *Graduate Theses and Dissertations*. 2431.
https://ecommons.udayton.edu/graduate_theses/2431

This Dissertation is brought to you for free and open access by the Theses and Dissertations at eCommons. It has been accepted for inclusion in Graduate Theses and Dissertations by an authorized administrator of eCommons. For more information, please contact mschlange1@udayton.edu, ecommons@udayton.edu.

JOINT SUPER-RESOLUTION AND SCENE-BASED NONUNIFORMITY CORRECTION
USING MAXIMUM *A POSTERIORI* ESTIMATION

Dissertation

Submitted to

The School of Engineering of the
UNIVERSITY OF DAYTON

in Partial Fulfillment of the Requirements for

The Degree

Doctor of Philosophy in Electrical Engineering

by

Douglas Ryan Droege

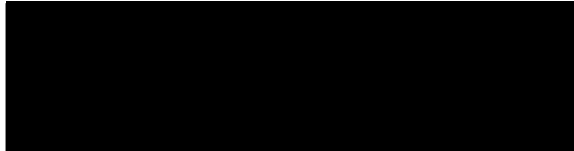
UNIVERSITY OF DAYTON

Dayton, OH

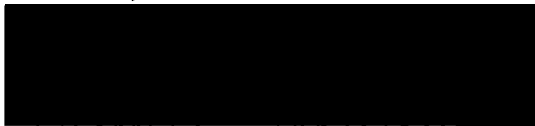
May 2008

JOINT SUPER-RESOLUTION AND SCENE-BASED NONUNIFORMITY CORRECTION
USING MAXIMUM *A POSTERIORI* ESTIMATION

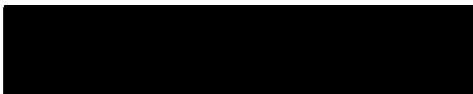
APPROVED BY:



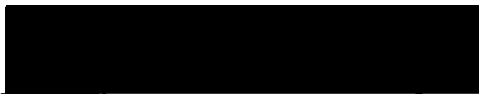
Russell Hardie, Ph.D.
Advisory Committee Chairperson
Professor, Electrical and Computer Engineering Department



John Weber, Ph.D.
Committee Member
Professor, Electrical and Computer Engineering Department



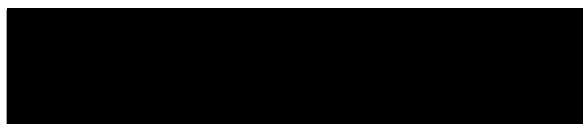
John Loomis, Ph.D.
Committee Member
Professor, Electrical and Computer Engineering Department



Peter Hovey, Ph.D.
Committee Member
Associate Professor, Mathematics Department



Malcolm Daniels, Ph.D.
Associate Dean, School of Engineering



Joseph Saliba, Ph.D., P.E.
Dean, School of Engineering

© Copyright by
Douglas Ryan Droege
All rights reserved
2008

ABSTRACT

A single infrared focal plane array (FPA) is made up of thousands of individual infrared detectors that convert photons into a digital value. Unfortunately, variability in an FPA causes different individual detectors to report different digital values when exposed to the same signal level. This nonuniformity limits imaging performance because it interferes with the spatial information of the true scene. It is possible to compensate for nonuniformity if the gain and bias coefficients of the linear model are known for each detector. Simple one-time factory calibration and even field calibration can be problematic, so scene-based nonuniformity correction (NUC) techniques have been proposed to perform the calibration using only the normal scene information captured by the imager.

In addition to detector nonuniformity, effects such as undersampling, blur and noise may degrade imagery. These can lead to a reduction in spatial resolution, which is often the most important characteristic of an imaging system. Standard approaches for increasing spatial resolution, such as modifying the optical design or reducing the detector size, require the system to sacrifice performance, are generally more costly, and may not be technologically possible. Alternatively, super-resolution (SR) signal processing techniques have been shown to improve resolution without physically altering the optical system or sensor.

In this dissertation, the scene-based NUC and SR problems are simultaneously addressed using a maximum *a posteriori* (MAP) estimation framework. This approach, termed the MAP SR-NUC algorithm, jointly estimates an HR image and gain and bias detector nonuniformity parameters using a sequence of observed frames. By combining scene-based NUC and SR in this fashion, it is demonstrated that superior results are possible compared with the more conventional

approach of performing scene-based NUC followed by independent SR. Additionally, when the MAP algorithm is applied without SR, the algorithm represents a novel and promising scene-based NUC technique that accurately corrects for gain and bias nonuniformity. The text presents two alternative solution methods, the first based on a gradient descent optimization and the second based on a conjugate-gradient optimization. Assumptions made during algorithm development are supported by a nonuniformity analysis of numerous actual FPAs.

DEDICATION

My fondest memories are sharing "special breakfasts" with Natalie, watching Ryan tear into his "hot dog and cheese," and hearing a serious "Oh, no!" come out of Allison's little mouth. My special thank you goes to you, Amy, for all your support. You "absolutely" make my life complete. This Dissertation and all my love are dedicated to each of you.

ACKNOWLEDGEMENTS

I would like to acknowledge the guidance and motivation Dr. Russ Hardie has offered over the past four years. He has challenged me to tackle and rigorously address difficult problems while also considering my needs as a non-traditional graduate student. Dr. Hardie's dedication to students at the University of Dayton has allowed me and so many other students to progress further than we thought possible.

TABLE OF CONTENTS

ABSTRACT.....	iii
DEDICATION.....	v
ACKNOWLEDGEMENTS.....	vi
LIST OF FIGURES	ix
LIST OF TABLES.....	xii
CHAPTER I. INTRODUCTION.....	1
CHAPTER II. FOCAL PLANE ARRAY NONUNIFORMITY	7
A. Nonuniformity Observation and Nonuniformity Correction Models.....	8
B. Nonuniformity and Residual Nonuniformity	9
C. Focal Plane Array Characterization	14
CHAPTER III. THE MAP SR-NUC ALGORITHM	27
A. Observation Model.....	28
B. MAP Estimation.....	30
C. Gradient Descent Optimization	31
D. Conjugate-Gradient Optimization.....	34
E. Bias-Only Simplification.....	36
CHAPTER IV. EXPERIMENTAL RESULTS	38

A. Simulated Data	38
B. Infrared Video	63
CHAPTER V. CONCLUSIONS	74
APPENDIX A. OPTIMUM STEP SIZE DERIVATION.....	77
1. Gradient Descent Step Size.....	77
2. Conjugate-Gradient Step Size.....	81
BIBLIOGRAPHY	86

LIST OF FIGURES

1. Block diagram modeling both the corruption caused by FPA nonuniformity and the correction performed by NUC algorithms.....	8
2. Frames of FPA data containing nonuniformity.....	12
3. Output responses and MAE of five pixels plotted against input signal level prior to corruption by nonuniformity.....	13
4. Nonuniformity of FPA 1.....	17
5. Nonuniformity of FPA 2.....	17
6. Nonuniformity of FPA 3.....	18
7. Nonuniformity of FPA 4.....	18
8. Nonuniformity of FPA 5.....	19
9. For a large number of FPAs, fraction of gain parameters that fall within N standard deviations of the mean.....	20
10. For a large number of FPAs, fraction of bias parameters that fall within N standard deviations of the mean.....	21
11. Spatial correlation of the gain parameters of a single FPA.....	22
12. Spatial correlation of the bias parameters of a single FPA.....	22
13. Correlation coefficient calculated between gain and bias parameters.....	23
14. Frame of noise data collected using an IR FPA.....	24
15. Spatial correlation of the noise of a single frame.....	25
16. Correlation coefficients calculated between adjacent noise frames.....	25
17. Observation model for simultaneous super-resolution and nonuniformity correction.....	27

18. Création of the simulated data set.	44
19. Random pixel shifts used to create the set of $P = 64$ simulated frames	45
20. Nonuniformity parameters used to create the set of simulated frames.....	45
21. Value of the MAP SR-NUC cost function when processing the $P = 64$ frame simulated data set.	46
22. MAP SR-NUC estimates of the HR image, gain parameters, and bias parameters.	47
23. Mean absolute error of the gain and bias estimates as a function of the number of input frames P	48
24. Images corrected for nonuniformity.....	49
25. Absolute error of the nonuniformity correction.	50
26. Mean absolute error of the set of simulated LR frames corrected using estimated NUC parameters.	51
27. Simulated 150 count blackbody image nonuniformity corrected.....	52
28. Mean absolute error of simulated blackbody frames corrected using estimated NUC parameters.	53
29. HR image output of registration-based NUC followed by bilinear interpolation when $P = 64$ frames.	56
30. HR image output of local constant statistics NUC followed by bilinear interpolation when $P = 64$ frames.....	56
31. HR image output of MAP NUC followed by bilinear interpolation when $P = 64$ frames.	57
32. HR image output of MAP SR-NUC when $P = 64$ frames.....	57
33. HR image output of MAP NUC followed by MAP SR when $P = 64$ frames.	58
34. HR image output of Bias-Only MAP SR-NUC when $P = 64$ frames.	58
35. HR image output of Bias-Only MAP NUC followed by Bias-Only MAP SR when $P = 64$ frames.....	59

36. Mean absolute error of the HR image estimates of five combinations of NUC and HR image estimation approaches.	60
37. Mean absolute error of the HR image estimates of four MAP approaches that perform both NUC and HR image estimation.	60
38. HR image output of MAP NUC followed by MAP SR when $P = 7$ frames.	61
39. HR image output of MAP SR-NUC when $P = 7$ frames.	61
40. HR image output of Bias-Only MAP NUC followed by MAP SR when $P = 7$ frames.	62
41. HR image output of Bias-Only MAP SR-NUC when $P = 7$ frames.	62
42. First uncorrected image sequence.	66
43. First image sequence frame one region of interest restored.	67
44. First image sequence frame one region of interest restored using alternate versions of the MAP SR-NUC algorithm.	68
45. First image sequence frame one region of interest restored using benchmark NUC algorithms then enlarged using bilinear interpolation.	69
46. First image sequence frame one license plate region of interest	70
47. Second uncorrected image sequence	71
48. Second image sequence frame one restored using alternate versions of the MAP SR-NUC algorithm.	72
49. Second image sequence frame one restored using benchmark NUC algorithms then enlarged using bilinear interpolation.	73

LIST OF TABLES

1. Typical levels of gain nonuniformity, bias nonuniformity, and noise based on a 14-bit dynamic range.	26
2. Variations of the MAP SR-NUC Algorithm.	38

CHAPTER I

INTRODUCTION

Infrared focal plane arrays (IR FPAs) are similar to the charge-coupled devices used in commercial digital cameras and camcorders, but they sense radiated heat energy instead of visible light [1]. They are essential in military, commercial, astronomical, and law-enforcement applications. A single FPA is made up of thousands of individual infrared detectors that operate by converting photons into electrons. The irradiance on an individual detector is estimated by counting the number of electrons generated by the detector in a certain period of time. This number is converted to a digital value that is combined with the digital values of other detectors to produce an image.

Unfortunately, variability in the production of the detectors, electronic readout devices, and structural state of the FPA causes different individual detectors to report different digital values when exposed to the same level of irradiance [2-4]. This nonuniformity limits imaging performance because it interferes with the spatial information of the true scene. It is possible to compensate for nonuniformity using a linear correction if the gain and bias coefficients of the linear model are known for each detector. But complicating matters, the nonuniformity tends to drift over time, changing over a nominal time period of minutes or hours [2]. This precludes a simple one-time factory nonuniformity correction (NUC) from completely eradicating the problem. Periodic calibration techniques can be employed to address the problem in the field. These, however, require halting normal operation while the imager is aimed at uniform calibration targets. They can also add significant size and cost to the system.

Many "scene-based" techniques have been proposed to perform NUC using only the normal scene information captured by the imager [5-25]. These signal processing techniques do not require calibration targets and therefore do not require halting the normal operation of the imager. Instead they utilize multiple video frames that have different amounts of relative motion with respect to the scene. This implies that different detectors in the FPA sample the same point in the scene at different frame times. By comparing the scene information in these frames, the FPA can be corrected so that each detector reports the same irradiance level when viewing the same point in the scene.

Scene-based NUC techniques can be classified as "constant statistics" techniques or "motion compensated" techniques. Constant statistics scene-based NUC techniques [6-16] are based on the assumption that some statistic that measures the output of a given detector should be the same as that of other detectors. Implicitly, this requires relative motion between the imager and the scene over a sufficient number of frames. In [6-9], offset and gain correction coefficients are estimated by assuming that the temporal mean and variance of each detector are identical over time. In [10-12], it is assumed that in the presence of constant motion, the irradiance incident upon each detector constantly changes but the spatial nonuniformity is stationary. The nonuniformity is then temporally low-pass in nature, so an offset correction is used to force the output of all detectors in the FPA to average the same value over time. Another approach presented in [10-12] relies on a local constant statistics assumption. Here, steepest descent is used to force the output of a pixel to be similar to that of its neighbors. The technique presented in [13] utilizes local constant statistics to treat the nonuniformity at the detector level separately from the nonuniformity in the readout electronics. A nonlinear filter based method that relies in part on the median of a pixel and its neighbors is described in [14]. Other approaches assume that the output of each detector should exhibit a constant range of values [15,16]. Constant statistics techniques generally work well when motion in a relatively large number of frames distributes diverse scene intensities across the FPA.

Motion compensated scene-based NUC techniques utilize specific knowledge of the relative motion from one frame to the next [5, 17–25]. When relative motion exists between the imager and the scene, the same point in the scene will be imaged on different FPA detectors at different frame times. Matching the scene information across multiple frames allows these techniques to distinguish between scene information and nonuniformity errors. In [17], a motion compensated temporal average approach is presented. Algebraic scene-based NUC techniques are developed in [18–20]. A regularized least squares method, closely related to this work, is presented in [21]. These motion compensated techniques are generally able to operate successfully with fewer frames than constant statistics techniques. Note that many motion compensated techniques utilize interpolation to treat subpixel motion. If the observed imagery is undersampled, the ability to perform accurate interpolation is compromised, and these NUC techniques can be adversely affected.

In addition to detector nonuniformity, effects such as undersampling, blur and noise may degrade imagery. These can lead to a reduction in spatial resolution, i.e. the minimum distance between distinguishable features in an image [26]. Spatial resolution may be the most important characteristic of an imaging system because utilizing the detail in an image is a shared goal of most imaging applications. For example, improving resolution increases range performance in military targeting applications [27]. There are many ways to increase spatial resolution. One method is to reduce the size of each detector, but this likewise reduces the collection area of the detector and therefore reduces signal-to-noise ratio. Reducing detector size can also be prohibitive because of limits in current technology and cost constraints. Other options are to increase the focal length of the optical system to magnify the scene on the FPA or to decrease the f-number to reduce the width of the optical point spread function. However, each of these leads to larger, heavier, and more expensive optical configurations.

Alternatively, super-resolution techniques [5, 24–25, 28–39] have been shown to improve resolution [44] without physically altering the optical system or sensor. A super-resolution

algorithm is a signal processing approach that discerns a high resolution (HR) image using the information contained in multiple low resolution (LR) images. For example, assume that a video sequence captured by an imager consists of multiple frames of the same scene but that each frame is shifted by a different subpixel amount relative to the scene. Then each frame in the sequence is afforded a similar but unique "look" at the same scene. SR techniques are able to combine the information in these multiple "looks" to identify an undegraded HR image of the scene. Note that the relative motion cannot simply be integer pixel shifts and that the imagery must be undersampled; otherwise, no new information would exist from frame to frame. It should also be noted that interpolation is not an SR technique since it does not recover any information not already contained in the original LR image. SR techniques are advantageous over other methods of increasing resolution because of their relative low cost and their ability to use the imagery from existing LR imaging systems. A good survey of the field can be found in [28, 29].

Two classifications of SR techniques are "interpolation-deconvolution" and "statistical estimation". Interpolation-deconvolution SR techniques interleave multiple LR images on a common HR pixel grid, then perform subsequent processing to remove diffraction and sampling effects. Relative motion between frames is compensated for using image registration, and nonuniform interpolation is used to estimate each HR pixel value. The resulting HR image is blurred because the system point spread function has not yet been considered. So deconvolution, typically performed using a Wiener filter, is used to remove the effects of diffraction and detector size and produce the final HR image. In [30], a weighted nearest neighbor approach is used to perform nonuniform interpolation. Nonuniform interpolation and deconvolution are performed simultaneously in [31]. The technique presented in [32] utilizes an adaptive Wiener filter to accomplish the deconvolution. In [33], localized optical flow is used to improve the accuracy of motion estimation. Interpolation-deconvolution approaches are typically less computational in nature, but do not provide the performance offered by other SR techniques.

Statistical estimation SR techniques define a statistical model that relates the LR image sequence with the single HR image, then use the model to fit the HR image to the actual LR image data. Those derived using a Bayesian framework, similar to the present technique, include [34–39]. When significant levels of both nonuniformity and aliasing are present, most approaches treat the nonuniformity and undersampling separately. In particular, some type of calibration or scene-based NUC is employed initially. This is followed by applying an SR algorithm to the corrected image [41, 42]. One pioneering paper developed a maximum likelihood estimator to jointly estimate a high resolution (HR) image, shift parameters, and nonuniformity parameters [25]. In general, statistical estimation techniques are somewhat complicated but fairly robust.

In this dissertation, the scene-based NUC and SR problems are simultaneously addressed using a maximum *a posteriori* (MAP) estimation framework. Using this approach, an HR image and gain and bias detector nonuniformity parameters are jointly estimated using a sequence of observed frames. This is referred to as the MAP SR-NUC algorithm. By combining NUC and SR in this fashion, it is demonstrated that superior results are possible compared with the more conventional approach of performing scene-based NUC followed by independent SR. This is because access to an HR image can make interpolation more accurate, leading to improved nonuniformity parameter estimation. Similarly, HR image estimation requires accurate knowledge of the detector nonuniformity parameters.

If the gain nonuniformity parameters are assumed to be unity, the MAP estimation framework reduces to a useful version of the MAP SR-NUC algorithm that estimates only the HR image and the bias nonuniformity parameters. This approach can be very effective when gain nonuniformity is at a low or even moderate level, and it requires fewer calculations. This approach, referred to here as the Bias-Only MAP SR-NUC algorithm, was co-developed by the author and published in [5]. When gain nonuniformity levels are larger, the full SR-NUC

algorithm is able to correct for both gain and bias nonuniformity while estimating an HR image that shows significant improvement over the original LR images.

The proposed MAP algorithm can be applied with or without SR, depending on the application and computational resources available. Without SR, the proposed algorithm represents a novel and promising scene-based NUC technique. This version, called the MAP NUC algorithm, can accurately correct for both gain and bias nonuniformity and support subsequent HR image estimation.

In addition to the Introduction, this Dissertation contains four chapters. Chapter II provides an in-depth examination of FPA nonuniformity by developing nonuniformity models, proposing metrics for quantifying nonuniformity, and characterizing the behavior of a large set of actual IR FPAs. The MAP SR-NUC algorithm, including variations of the algorithm and optimization techniques, is outlined in Chapter III. Chapter IV presents the experimental results derived from a simulated data set and two real infrared data sets. Finally, the body of work is summarized and conclusions are presented in Chapter V.

CHAPTER II

FOCAL PLANE ARRAY NONUNIFORMITY

A single FPA is made up of thousands of individual infrared detectors that operate by converting photons into electrons. The irradiance on an individual detector is estimated by counting the number of electrons generated by the detector in a certain period of time. This number is converted to a digital value that is combined with the digital values of other detectors to produce an image.

Unfortunately, variability in the production of the detectors, electronic readout devices, and structural state of the FPA causes different individual detectors to report different digital values when exposed to the same level of irradiance [2-4]. This nonuniformity limits imaging performance because it interferes with the spatial information of the true scene.

It is possible to compensate for nonuniformity using a linear correction if the gain and bias coefficients of the linear model are known for each detector. This process is called nonuniformity correction, or NUC. There are both standard and scene-based NUC approaches. Standard NUC approaches utilize uniform calibration targets. "Scene-based" NUC techniques use only the normal scene information captured by the imager.

This chapter examines focal plane nonuniformity. First, the processes of nonuniformity corruption and subsequent nonuniformity correction are modeled. Second, metrics are proposed that measure both raw nonuniformity and the residual nonuniformity that is present after NUC is applied. Third, FPA nonuniformity is characterized both to support mathematical assumptions made during the development of the MAP SR-NUC algorithm and to estimate values for algorithm parameters.

A. Nonuniformity Observation and Nonuniformity Correction Models

A continuous image incident upon the FPA is free from detector nonuniformity. Individual detectors with different responses sample the incident image, resulting in the FPA reporting an observed frame that is corrupted by nonuniformity. Nonuniformity correction, or NUC, attempts to compensate for this detector nonuniformity and restore the corrupted frame to the original, undegraded frame.

The process of nonuniformity corruption followed by nonuniformity correction is represented by the model in Figure 1. An original frame, assumed to have already been sampled by the FPA but not yet corrupted by nonuniformity, is represented in lexicographical notation as the $M \times 1$ vector \tilde{y}_k , where $k = 1, 2, \dots, P$. FPA nonuniformity is characterized using a gain and bias model. The gains are represented by the $M \times 1$ vector \mathbf{a} , where M is the number of pixels in the FPA. The biases are represented by the $M \times 1$ vector \mathbf{b} . Together, these produce an observed frame \mathbf{y}_k that is reported by the FPA. The full nonuniformity corruption process is

$$\mathbf{y}_k = \mathbf{A}\tilde{\mathbf{y}}_k + \mathbf{b}, \quad (1)$$

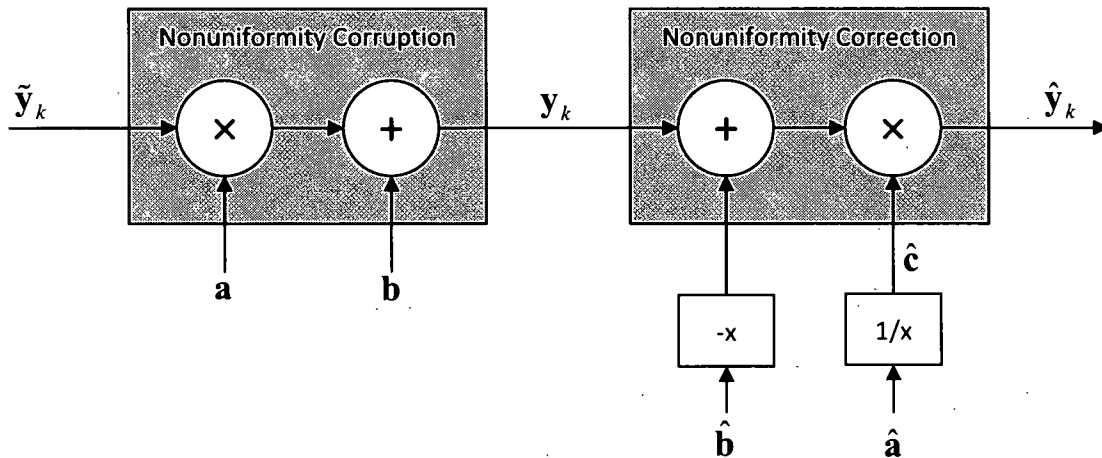


Figure 1. Block diagram modeling both the corruption caused by FPA nonuniformity and the correction performed by NUC algorithms.

where \mathbf{A} is the $M \times M$ diagonal matrix that contains the elements of \mathbf{a} on its main diagonal (and zeros elsewhere).

Nonuniformity correction is likewise characterized using a gain and bias model. An estimate of the gain nonuniformity is introduced using the $M \times 1$ vector $\hat{\mathbf{a}}$. An estimate of the bias nonuniformity is the $M \times 1$ vector $\hat{\mathbf{b}}$. To perform a correction, the estimated nonuniformity must be removed from the observed frame \mathbf{y}_k . Thus, the bias estimate $\hat{\mathbf{b}}$ must be subtracted from \mathbf{y}_k and the result divided element-by-element by the gain estimate $\hat{\mathbf{a}}$. The result is a corrected frame $\hat{\mathbf{y}}_k$ that is an estimate of the original, undegraded frame $\tilde{\mathbf{y}}_k$. The full nonuniformity correction process is

$$\hat{\mathbf{y}}_k = \hat{\mathbf{C}}(\mathbf{y}_k - \hat{\mathbf{b}}), \quad (2)$$

where $\hat{\mathbf{C}}$ is the $M \times M$ diagonal matrix that contains on its diagonal the elements of an $M \times 1$ vector $\hat{\mathbf{c}}$ whose elements are

$$\hat{c}_l = \frac{1}{\hat{a}_l}, \quad (3)$$

where $l = 1, 2, \dots, M$.

B. Nonuniformity and Residual Nonuniformity

Figures 2(a-c) show three frames of actual FPA data that have been degraded by FPA nonuniformity. They were created using a blackbody device that produced a uniform temperature scene at three different signal levels. Although the three frames are captured using the same FPA, each frame is different because nonuniformity is dependent on input signal level. In Figure 3(a), the output responses of five pixels from this FPA are plotted against the input signal level prior to corruption by nonuniformity. The 14-bit dynamic range shown on the axes represents the range of values reported by this FPA. Also shown as a dashed line is the ideal uniform response that each pixel would have in the absence of nonuniformity.

The nonuniformity error at a given input signal level is the deviation from the ideal uniform response. This is quantified using mean absolute error (MAE). For an image containing $l=1, 2, \dots, M$ pixels, the nonuniformity MAE is defined as

$$MAE_{y_k} = \frac{1}{M} \sum_{l=1}^M |y_k(l) - \tilde{y}_k(l)|. \quad (4)$$

Assuming that the average of the nonuniform responses of several pixels yields an estimate of the ideal uniform response, nonuniformity MAE can be calculated as

$$MAE_{y_k} = \frac{1}{M} \sum_{l=1}^M \left| y_k(l) - \frac{1}{M} \sum_{p=1}^M y_k(p) \right|. \quad (5)$$

Figure 3(a) shows the MAE of the nonuniform image at different points across the dynamic range.

A nonuniformity correction consisting of bias and gain corrections is generally able to remove the bulk of the nonuniformity across the majority of the dynamic range. However, imperfections in the linear model allow some post-correction nonuniformity to remain. This residual nonuniformity is measured by

$$MAE_{\hat{y}_k} = \frac{1}{M} \sum_{l=1}^M \left| \hat{y}_k(l) - \frac{1}{M} \sum_{p=1}^M \hat{y}_k(p) \right|. \quad (6)$$

Residual nonuniformity is typically greatest at those points in the dynamic range that are furthest from the correction point.

Consider for a moment a bias-only nonuniformity correction performed near the middle of the dynamic range. Figures 2(d-f) show that the corrected FPA data at the bias correction point is extremely uniform, but that the corrected FPA data at the ends of the dynamic range remain nonuniform. The effect of the correction is further demonstrated in Figure 3(b), which shows that corrected pixel responses closely match the ideal uniform response near the bias correction point but strongly deviate from the ideal uniform response near the ends of the dynamic range. In fact, at the low end of the dynamic range, the bias-only correction residual nonuniformity is actually

greater than the uncorrected nonuniformity. The MAE plot in Figure 3(b) also shows that the error of the bias-corrected image is larger at locations far from the bias correction point.

Next consider a gain and bias correction. There is a multitude of ways to define a linear correction. Here, three points are used. The bias correction is first performed at a point near the near 50% of the dynamic range maximum. Gain parameters are then defined using two points, one near 25% of the dynamic range maximum and one near 75% of the dynamic range maximum, and are applied after the bias corrections. The result is a linear correction that almost perfectly matches the ideal uniform response near the bias correction point and closely matches the ideal response across the rest of the dynamic range. The corrected data images in Figures 2(g-i) show that the correction output remains uniform across the dynamic range. Additionally, Figure 3(c) shows that the corrected output response closely matches the ideal uniform response.

In contrast with standard calibration approaches, in which the locations of correction points are typically fixed, a scene-based NUC algorithm performs its correction at the average signal level of the scene. This is a significant advantage because the portion of the dynamic range that is most accurately corrected is the portion that is currently being utilized by the scene.

A nuance of nonuniformity correction occurs when a bias-only nonuniformity model is used to estimate the nonuniformity in data that contains both gain and bias nonuniformity. The result is a bias nonuniformity estimate that corresponds to the total amount of nonuniformity at the correction point, including contributions from both gain and bias nonuniformity. When this occurs for a bias-only scene-based NUC algorithm that estimates corrections at the current scene operating point, it is beneficial because the algorithm attempts to address the current level of nonuniformity in the scene and not just the bias nonuniformity.

In summary, for typical levels of FPA nonuniformity, both gain and bias corrections are necessary. Additionally, scene-based NUC algorithms have the potential to outperform standard NUC approaches because they perform the correction at the current scene operating point.

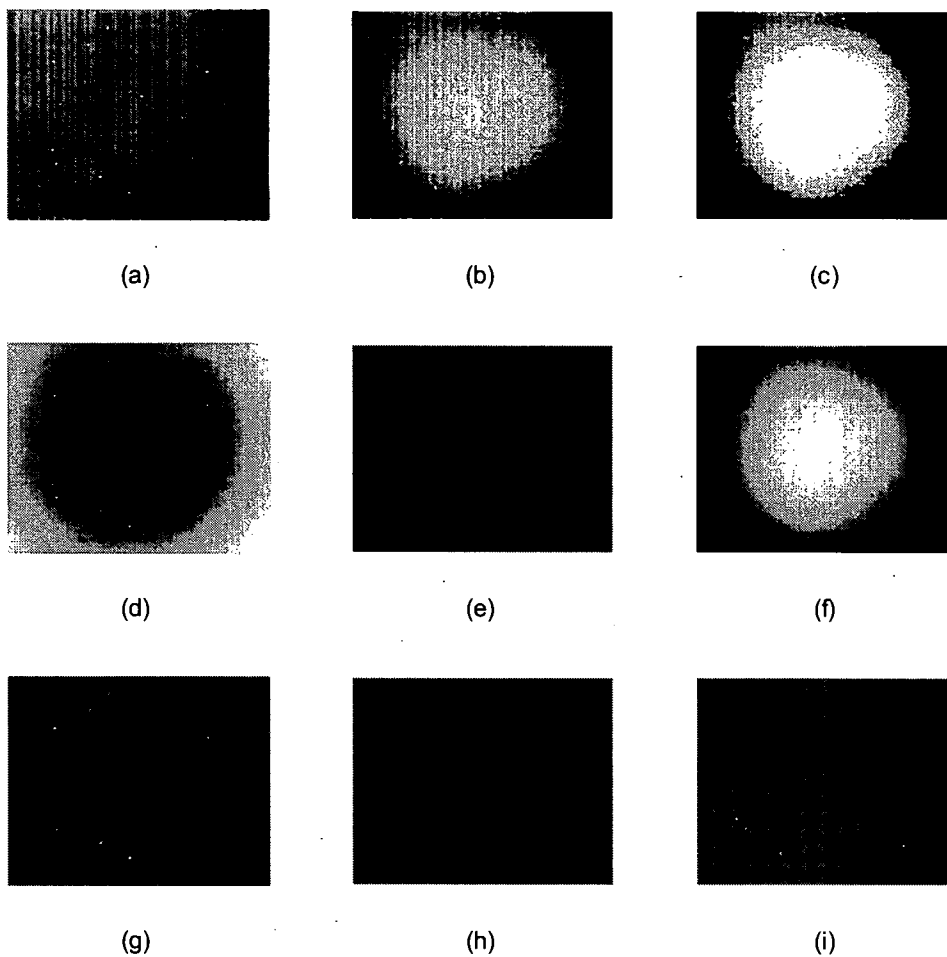
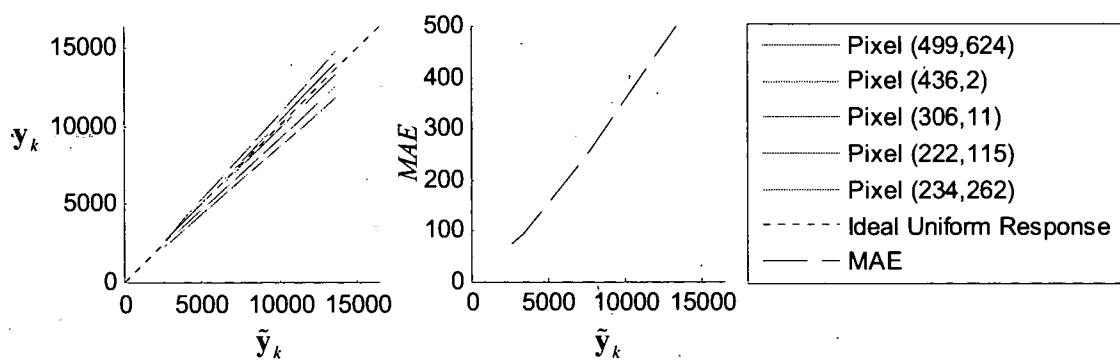
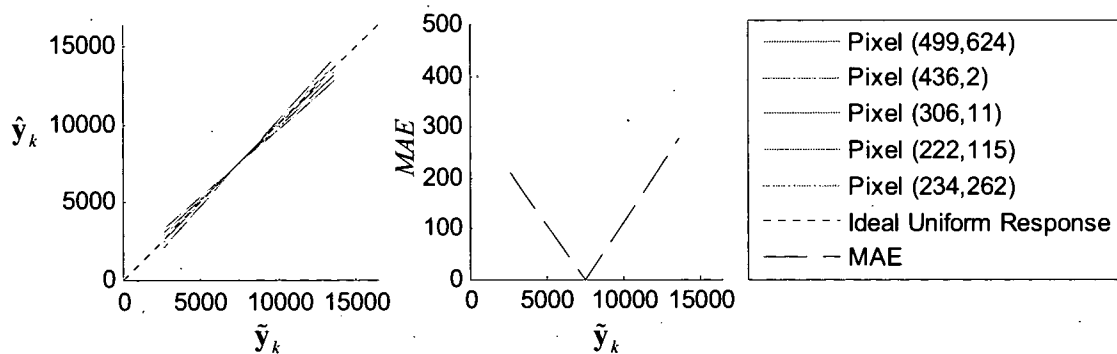


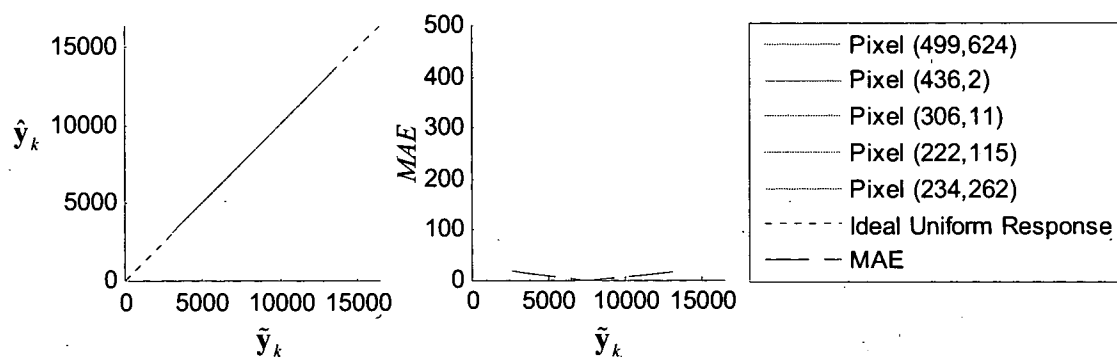
Figure 2. Frames of FPA data containing nonuniformity, created using a blackbody set to a (a) low scene temperature (b) medium scene temperature (c) high scene temperature. Bias corrected frames at (d) low scene temperature (e) medium scene temperature (f) high scene temperature. Gain and bias corrected frames at (g) low scene temperature (h) medium scene temperature (i) high scene temperature.



(a)



(b)



(c)

Figure 3. Output responses and MAE of five pixels plotted against input signal level prior to corruption by nonuniformity when (a) uncorrected (b) bias corrected (c) gain and bias corrected.

C. Focal Plane Array Characterization

A detailed characterization of IR FPAs is essential to the MAP SR-NUC algorithm for two reasons. First, several mathematical assumptions must be made during the theoretical development of the MAP estimator, and the validity of these assumptions (or lack thereof) should be understood. Second, practical use of the algorithm on real infrared data requires the specification of several parameter values.

To accomplish these goals, 983 IR FPAs are characterized. Each FPA is composed of Indium-Antimonide (InSb) detectors with a wavelength spectral response of $3\mu\text{m} - 5\mu\text{m}$. The array of 640×512 detectors is set on a $28\mu\text{m}$ pitch and produces output pixel data with 14-bit precision. To test an individual FPA, it is mounted in an $f/4$ test dewar and cooled to a cryogenic temperature. A blackbody is used to collect data at different reference temperatures. Significantly bad pixels are removed from the calculations and the data is compensated for an irregularity in the test dewar that causes additional spurious signal. In general, it is expected that certain effects, such as $\cos^4\theta$ doming, will be similar from FPA to FPA as long as format, pitch, f-number, and read out structure are similar. It is expected that other effects will vary from FPA to FPA.

One mathematical assumption made in the development of the MAP estimator is that the gain and bias parameters can be modeled as Gaussian random vectors. This assumption is made to regularize the estimation process and therefore avoid arriving at an estimated result that is obviously incorrect. This model generally does not need to be perfectly satisfied to be useful. There are many methods for validating an assumption of normality. These include visually examining a histogram of the data values for the well-known bell shape, examining a normal plot of ordered data values for linearity, evaluating whether the three sigma rule holds, and using formal statistical tests [43]. Two of these methods are employed here. First, the gain and bias parameters of five of the FPAs are histogrammed in Figures 4-8 along with a Gaussian fitted to the data using the peak histogram count and the mean and standard deviation of the parameters.

The data do seem to have a generally Gaussian shape, even though they deviate in some cases. Second, the gain and bias parameters of all 983 FPAs are analyzed to determine the fraction of values that fall within one standard deviation, two standard deviations, and three standard deviations of the mean. The results are histogrammed in Figures 9-10. The results are similar to the 68%, 95%, and 99% expected for a Gaussian distribution. Overall, the Gaussian model is not perfect but is probably close enough to be useful. Additionally, the Gaussian model may be as good as any model that can be developed for a general set of FPAs with varying distributions.

Another mathematical assumption made in the development the proposed MAP estimator is that the gain and bias parameters are assumed to be independent and identically distributed (i.i.d.). This means that gain parameter for each pixel in the FPA, which is a random variable, has the same probability density function as the gain parameters for the other pixels and that the value of each gain parameter is independent of the other gain parameters. Likewise, it is assumed that the bias nonuniformity parameter for each pixel in the FPA has the same probability density function as the bias parameters for the other pixels and that the value of each bias parameter is independent of the other bias parameters. From the images in Figures 4-8, it is apparent that the gain and bias parameters are not i.i.d. For example, a circularly symmetric pattern known as $\cos^4\theta$ doming extends outwards from the center of the FPA on each of the images. For a single FPA, the spatial correlation between the gains is shown in Figure 11 and the spatial correlation between the biases is shown in Figure 12. Both indicate strong levels of spatial correlation.

It also simplifies the underlying mathematics of the MAP estimator if it is assumed that the prior distributions of the gains and biases are independent. To evaluate this assumption, the gains and biases of the 983 tested FPAs are compared by calculating the correlation coefficient between the gain vector and bias vector of each FPA. The histogrammed results in Figure 13 show that there is often a high level of correlation between the gains and biases. This is supported by a qualitative evaluation of the images in Figures 4-8 which show that many of the features in the gains and biases appear similar. In general, the assumption that the gains and

biases are independent does not hold. However, a useful and tractable solution can be obtained under this assumption. Future work may seek to exploit such correlation using more complex models.

Similar assumptions are made about the system noise. To analyze these assumptions, a sequence of 500 frames is captured using a single FPA. The frames are corrected for spatial nonuniformity, leaving only the frame-to-frame temporal noise variations. The histogram of the single noise frame in Figure 14(b) indicates that the noise parameters can be modeled as a Gaussian random vector with a mean of zero. Additionally, measurements showing that 70.9% of noise values fall within one standard deviation of the mean, 95.5% of values fall within two standard deviations, and 99.8% of values fall within three standard deviations support the assumption that the noise is Gaussian. Visual inspection of the noise frame shown in Figure 14(a) indicates that the noise parameters can be assumed to be independent and identically distributed. This conclusion is supported by the mesh plot in Figure 15 that shows little spatial correlation. Finally, the noise is assumed to vary independently from frame-to-frame. This is confirmed by Figure 16, which shows that the correlation coefficient calculated between the 500 adjacent frames is only slightly above zero.

Finally, this FPA data is used to aid in the choice of the default values for parameters used in the MAP SR-NUC algorithm. The gain parameters for all the FPAs are histogrammed then added together. Assuming that the distributions are independent, the Central Limit Theorem states that the result will be approximately Gaussian. Likewise, the bias parameters are histogrammed then added together to produce an approximately Gaussian result. The statistics of these distributions are listed in Table 1. The variances are used in Chapter IV as default parameters when applying the MAP SR-NUC algorithm to a real FPA frame sequence.

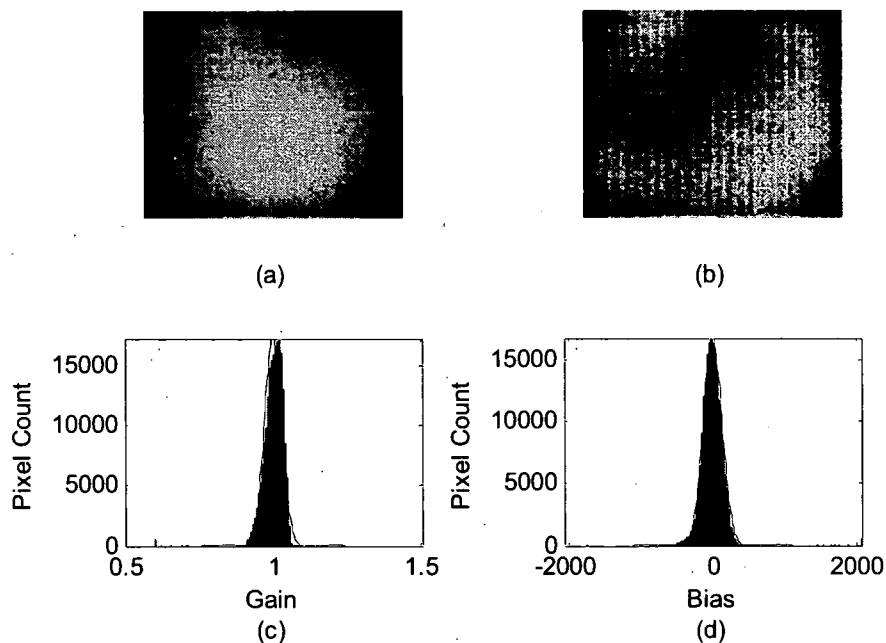


Figure 4. Nonuniformity of FPA 1 (a) gain nonuniformity parameters (b) bias nonuniformity parameters (c) histogram of gain nonuniformity parameters with Gaussian fit (d) histogram bias nonuniformity parameters with Gaussian fit.

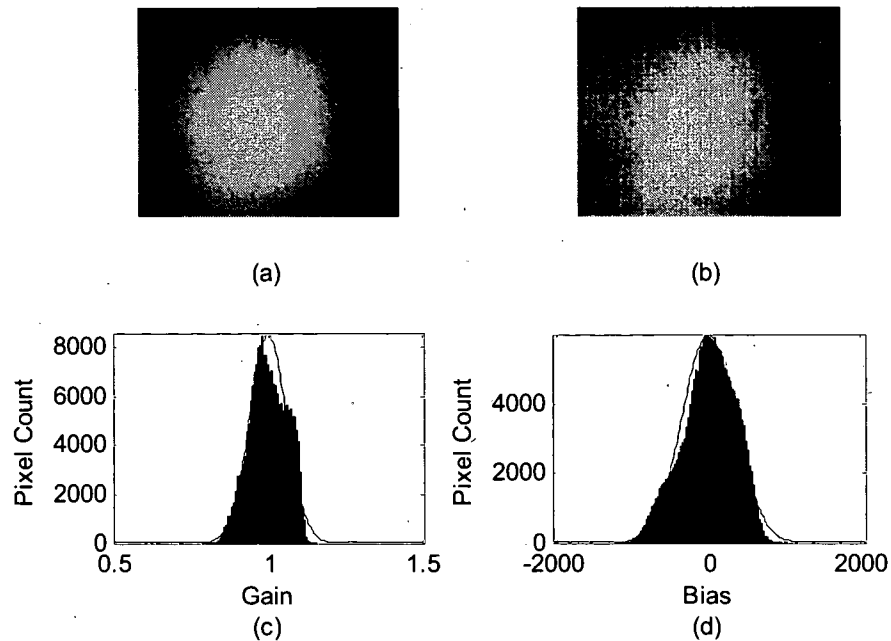


Figure 5. Nonuniformity of FPA 2 (a) gain nonuniformity parameters (b) bias nonuniformity parameters (c) histogram of gain nonuniformity parameters with Gaussian fit (d) histogram bias nonuniformity parameters with Gaussian fit.

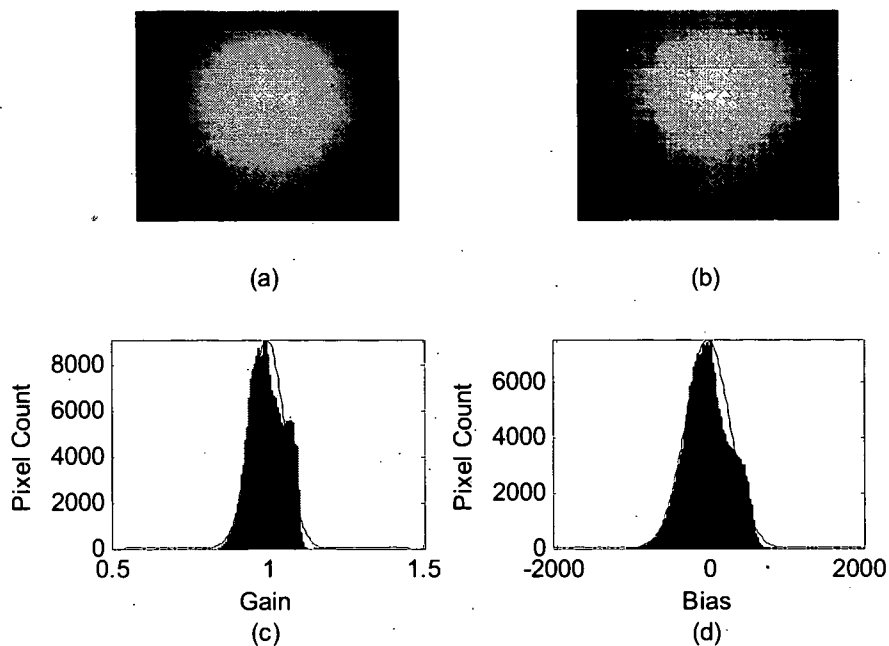


Figure 6. Nonuniformity of FPA 3 (a) gain nonuniformity parameters (b) bias nonuniformity parameters (c) histogram of gain nonuniformity parameters with Gaussian fit (b) histogram bias nonuniformity parameters with Gaussian fit.

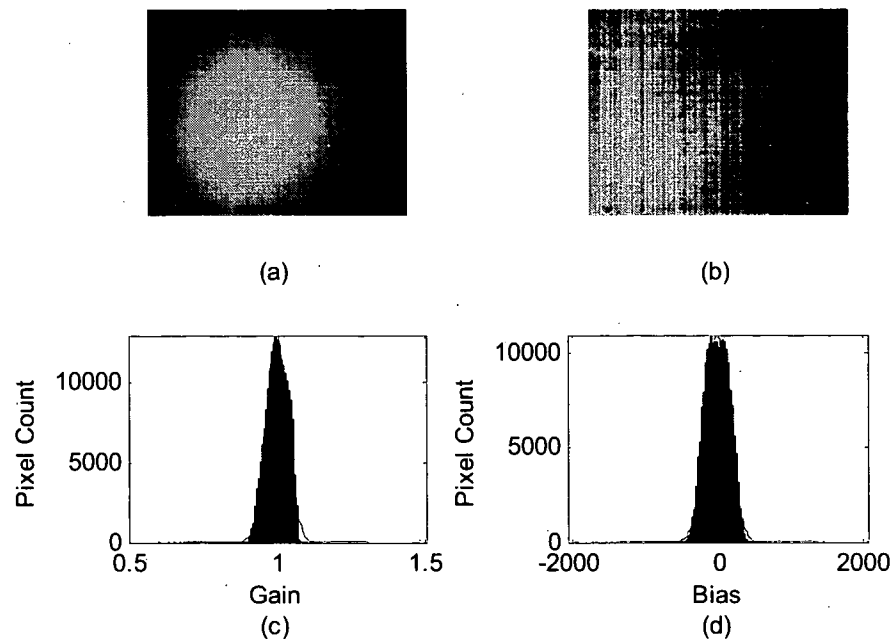


Figure 7. Nonuniformity of FPA 4 (a) gain nonuniformity parameters (b) bias nonuniformity parameters (c) histogram of gain nonuniformity parameters with Gaussian fit (b) histogram bias nonuniformity parameters with Gaussian fit.

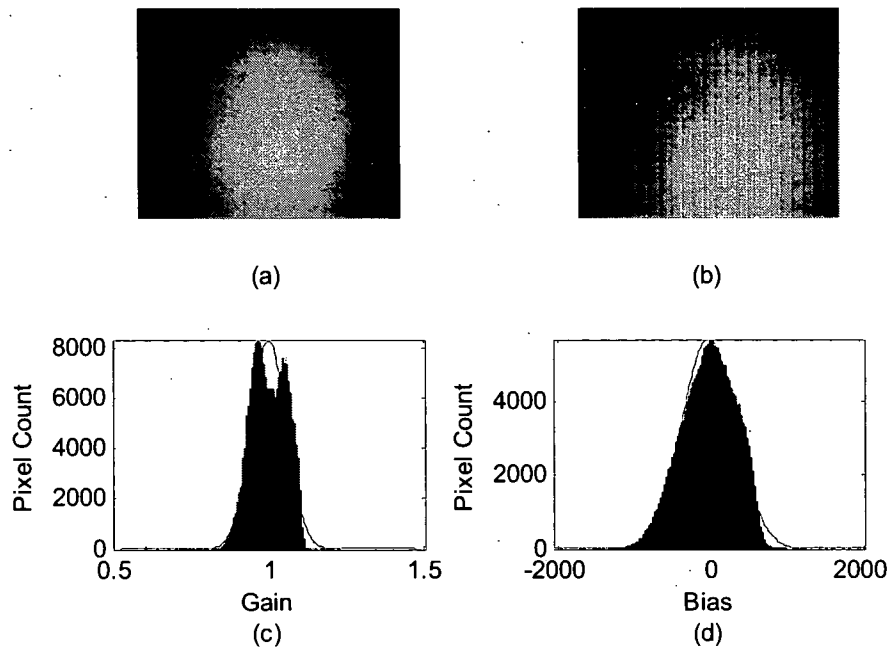


Figure 8. Nonuniformity of FPA 5 (a) gain nonuniformity parameters (b) bias nonuniformity parameters (c) histogram of gain nonuniformity parameters with Gaussian fit (d) histogram bias nonuniformity parameters with Gaussian fit.

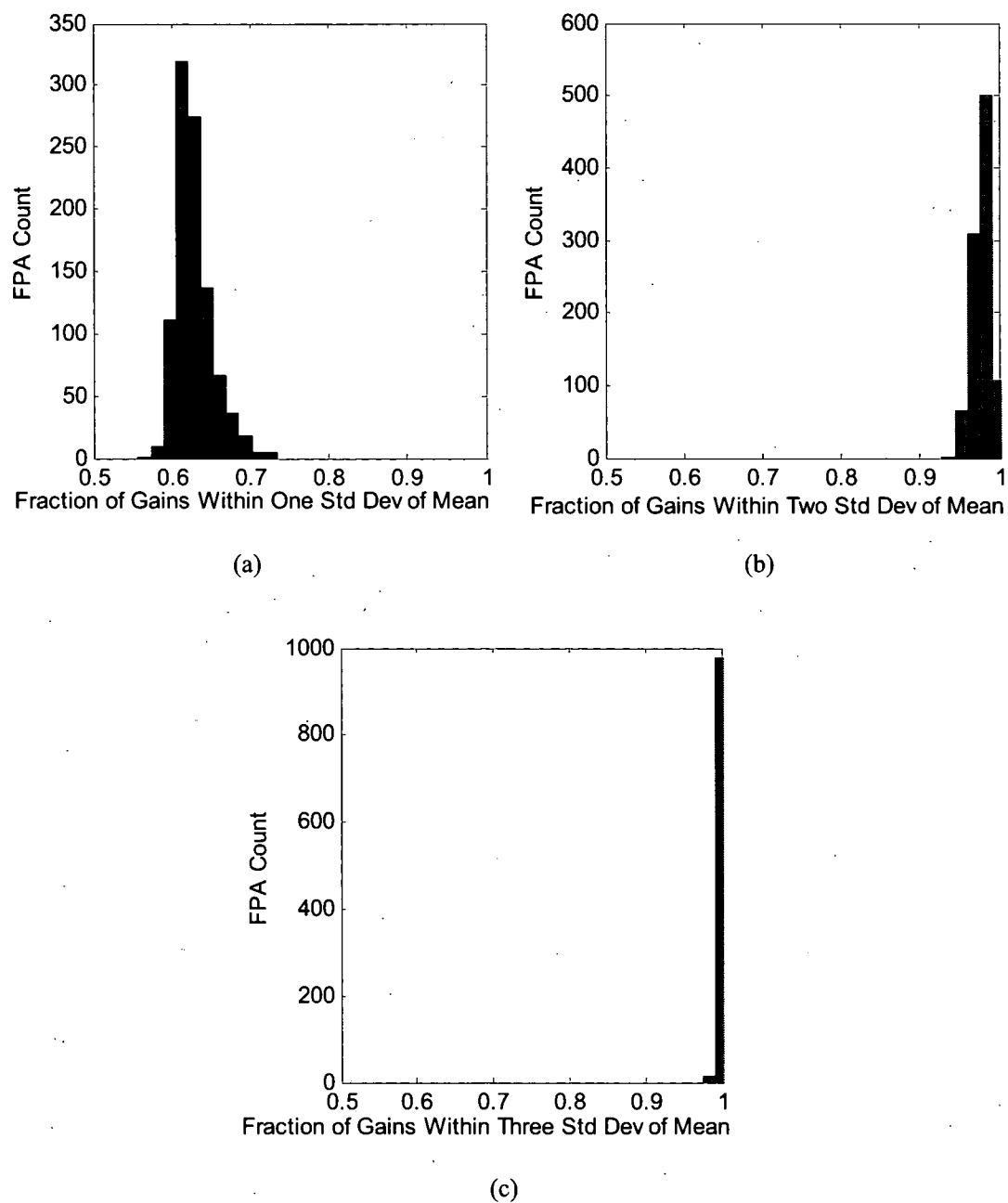


Figure 9. For a large number of FPAs, fraction of gain parameters that fall within (a) one standard deviation of the mean (b) two standard deviations of the mean (c) three standard deviations of the mean.

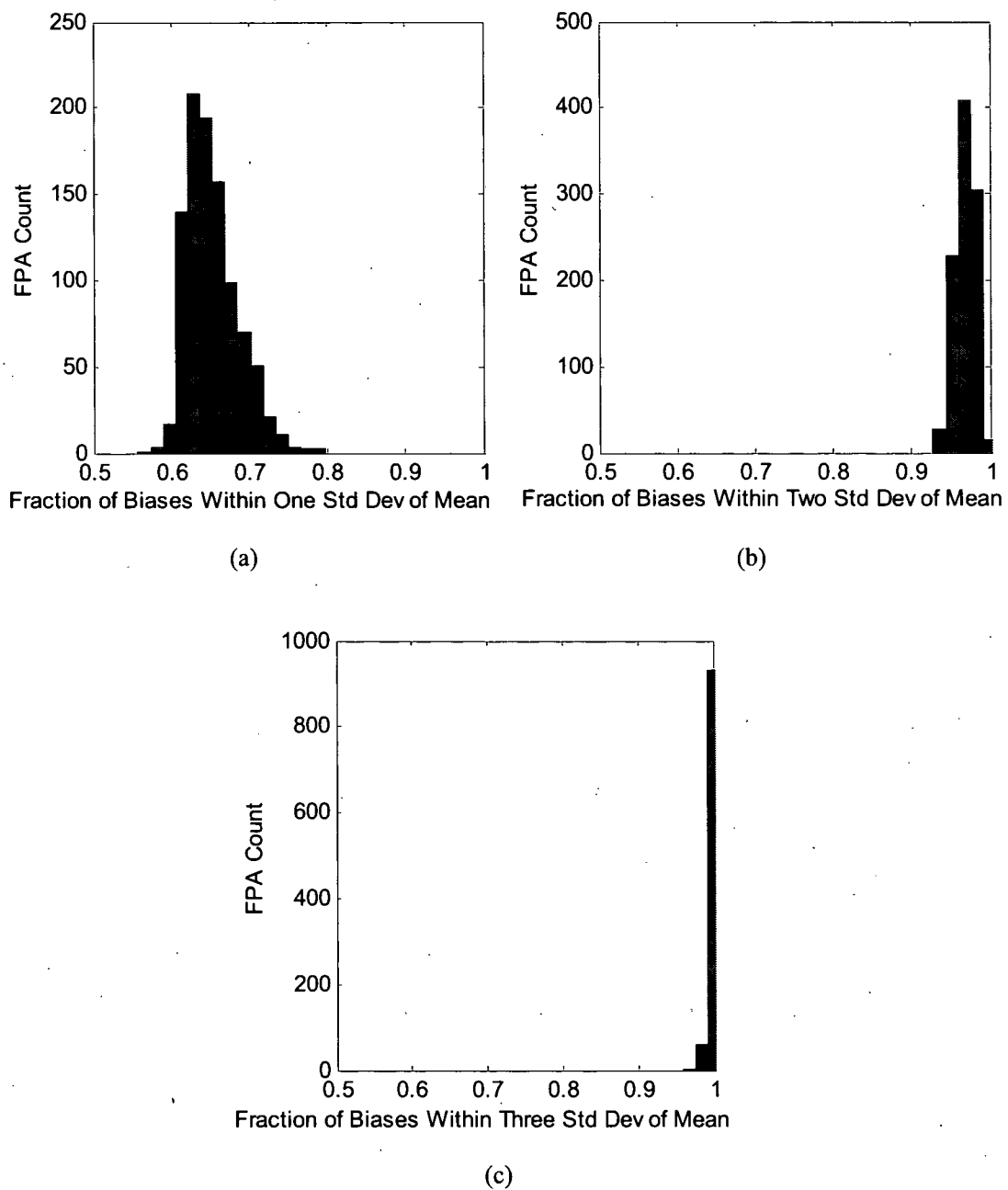


Figure 10. For a large number of FPAs, fraction of bias parameters that fall within (a) one standard deviation of the mean (b) two standard deviations of the mean (c) three standard deviations of the mean.

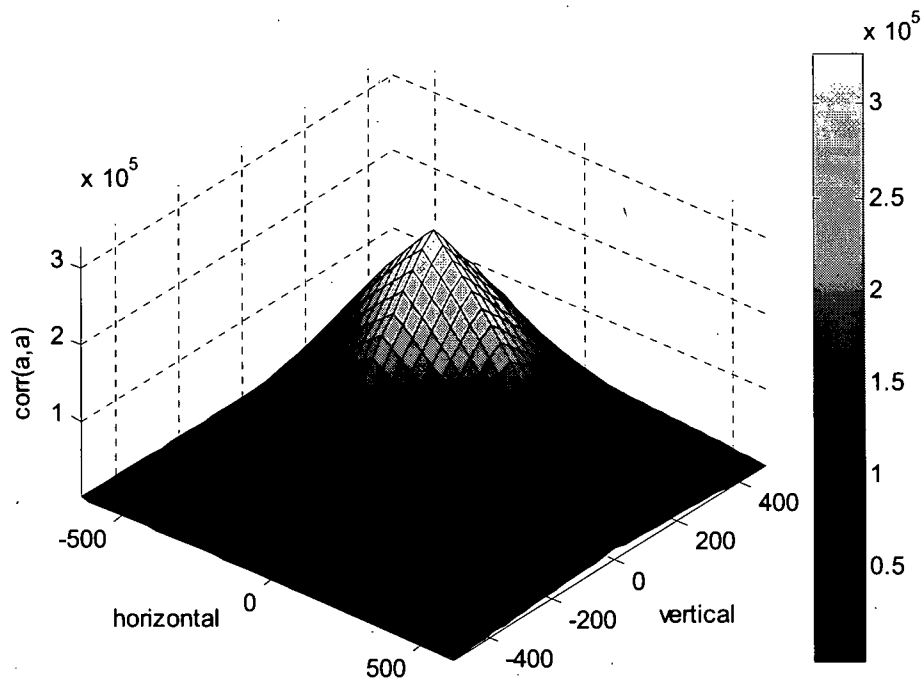


Figure 11. Spatial correlation of the gain parameters of a single FPA.

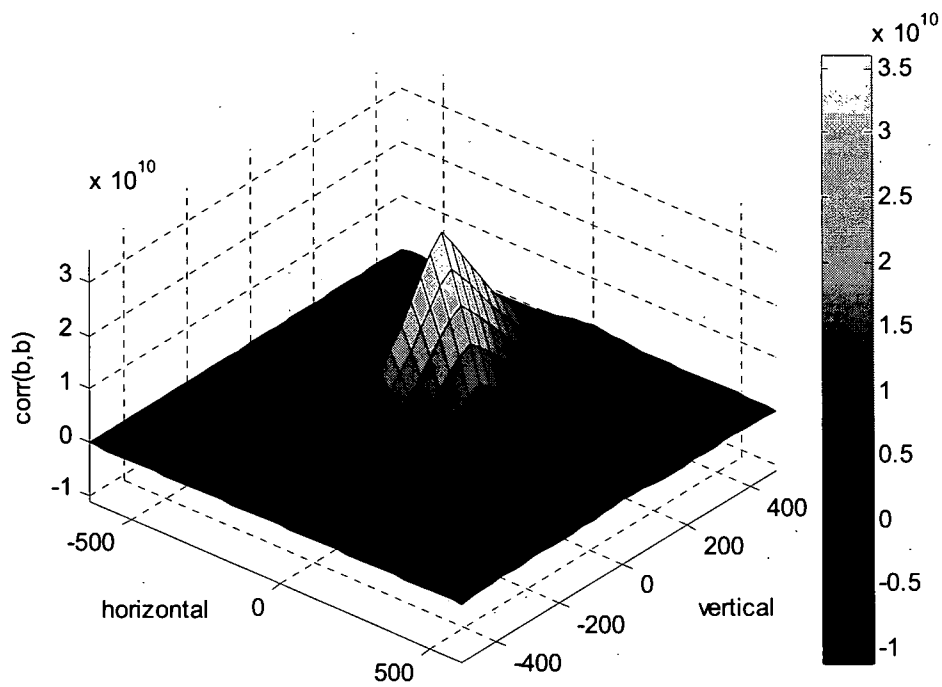


Figure 12. Spatial correlation of the bias parameters of a single FPA.

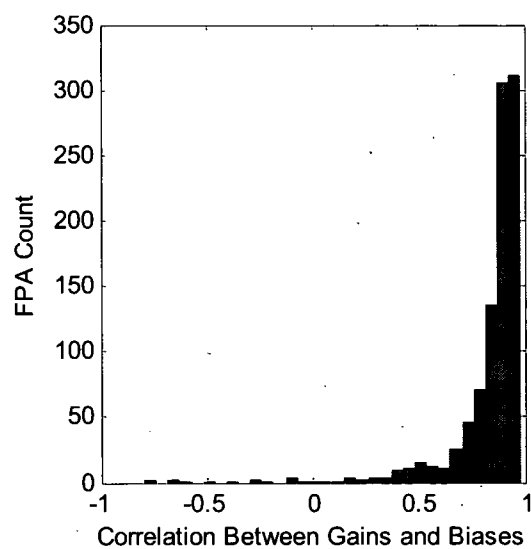
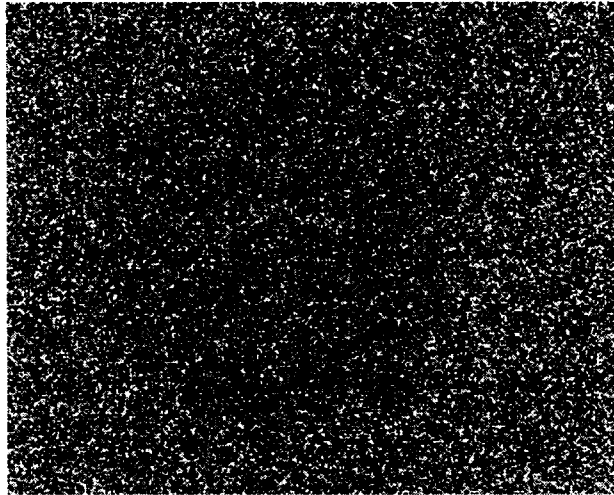
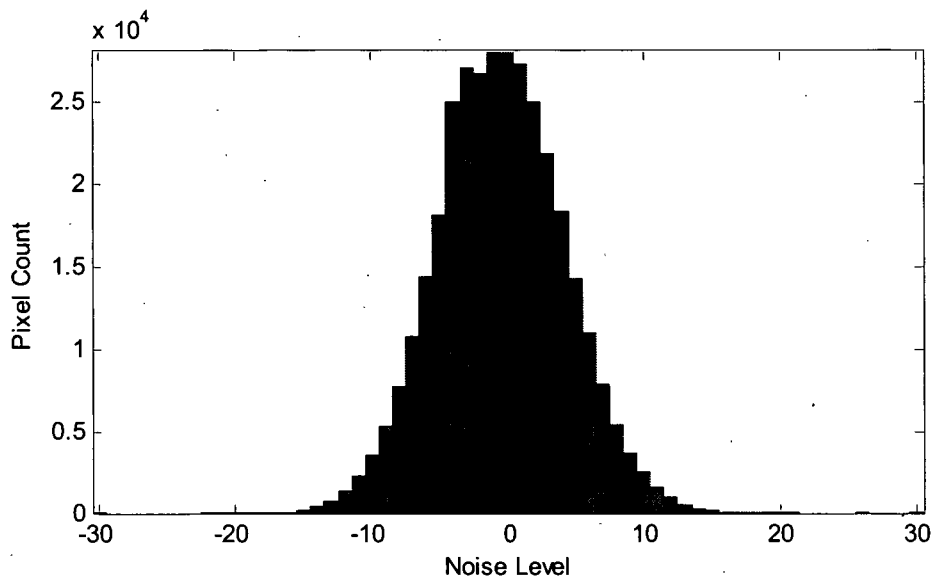


Figure 13. Correlation coefficient calculated between gain and bias nonuniformity parameters. Results for a large number of FPAs are compiled in the histogram.



(a)



(b)

Figure 14. Frame of noise data collected using an IR FPA. (a) image (b) histogram

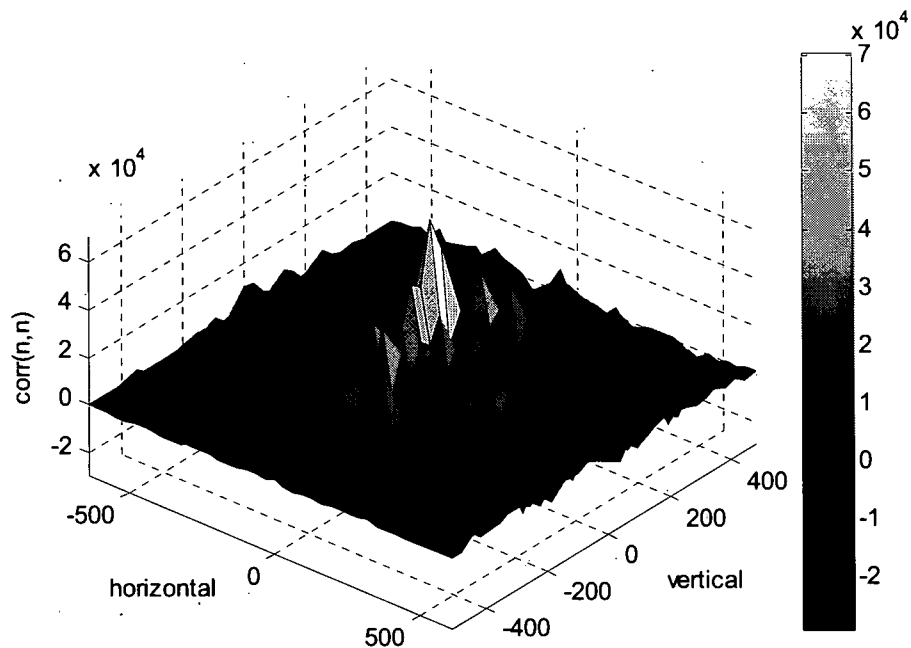


Figure 15. Spatial correlation of the noise of a single frame.

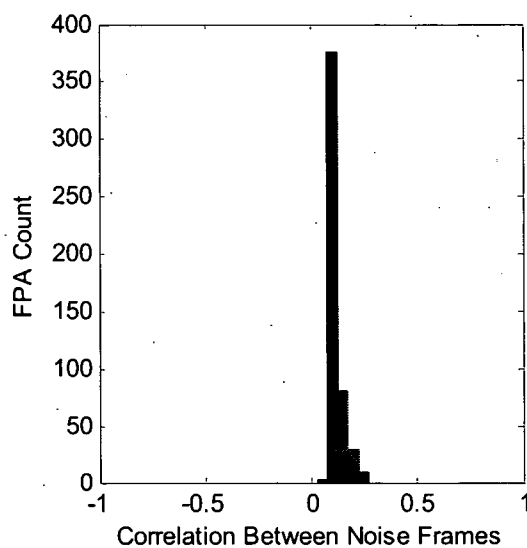


Figure 16. Correlation coefficients calculated between adjacent noise frames.

	Standard Deviation	Variance
Gain Nonuniformity	0.062	0.0038
Bias Nonuniformity	479.3 counts	229725 counts
Noise	9.995 counts	99.906 counts

Table 1. Typical levels of gain nonuniformity, bias nonuniformity, and noise based on a 14-bit dynamic range.

CHAPTER III

THE MAP SR-NUC ALGORITHM

The MAP SR-NUC algorithm uses a maximum *a posteriori* (MAP) estimation framework to jointly estimate an SR image and gain and offset nonuniformity parameters from a sequence of observed frames. Gaussian prior models are employed and a gradient descent optimization is utilized to identify estimates for the HR image and nonuniformity parameters. This algorithm uniquely solves the SR and scene-based NUC problems in a joint fashion, producing better results than performing SR and NUC separately. Even when performing NUC alone, this algorithm offers a novel approach to scene-based NUC.

Section A presents the observation model that relates an HR image and gain and bias nonuniformity parameters to a set of observed LR images. Section B formulates a MAP estimator that is able to estimate the HR image, gain nonuniformity parameters, and bias nonuniformity parameters from the set of LR images. Two methods for finding the optimal solutions for the estimated parameters are outlined in Sections C and D. Finally, Section E offers a bias-only version of the SR-NUC algorithm that estimates only the HR image and the bias nonuniformity parameters.

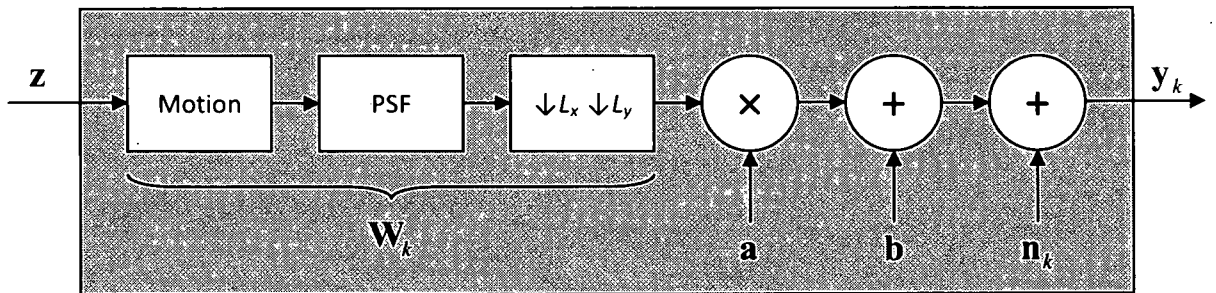


Figure 17. Observation model for simultaneous super-resolution and nonuniformity correction.

A. Observation Model

The goal of the MAP SR-NUC algorithm is to recover an original HR image from a set of observed, uncorrected LR frames. The LR frames are related to the original image but have been degraded by multiple effects. These effects are represented in the observation model shown in Figure 17. The original HR frame, assumed to have been sampled at or above the Nyquist rate, is represented in lexicographical notation as the $N \times 1$ vector \mathbf{z} . The $M \times N$ matrix \mathbf{W}_k introduces a geometric transformation modeling relative motion between the FPA and the scene, 2-D convolution by the point spread function, and downsampling by factors of L_x horizontally and L_y vertically. FPA nonuniformity is characterized using a gain and bias model. The gains are represented by the $M \times 1$ vector \mathbf{a} , where $M = N / (L_x L_y)$. The biases are represented by the $M \times 1$ vector \mathbf{b} . Finally, additive Gaussian noise is introduced by the $M \times 1$ vector \mathbf{n}_k . Together, these produce an observed frame \mathbf{y}_k , where $k = 1, 2, \dots, P$. The full observation model is

$$\mathbf{y}_k = \mathbf{A}\mathbf{W}_k\mathbf{z} + \mathbf{b} + \mathbf{n}_k, \quad (7)$$

where \mathbf{A} is the $M \times M$ diagonal matrix that contains the elements of \mathbf{a} on its main diagonal (and zeros elsewhere).

To complete the statistical model that will be used by the MAP estimator, the HR image \mathbf{z} , gains \mathbf{a} , biases \mathbf{b} , and noise vectors \mathbf{n}_k are modeled as Gaussian random vectors. Introducing this *a priori* knowledge helps to regularize the estimation process, avoiding potential solutions for \mathbf{z} , \mathbf{a} , \mathbf{b} , and \mathbf{n}_k that are obviously incorrect. The noise is assumed to vary independently from frame-to-frame and have a mean of zero and constant variance σ_n^2 . It is therefore represented by the multivariate pdf

$$\Pr(\mathbf{n}_k) = \frac{1}{(2\pi)^{\frac{M}{2}} \sigma_n^M} \exp \left\{ -\frac{1}{2\sigma_n^2} \mathbf{n}_k^T \mathbf{n}_k \right\}. \quad (8)$$

The gains and biases are assumed to be constant across the P observed frames. Modeling the gain parameters as a Gaussian vector with variance σ_a^2 and a mean of 1, the resulting pdf is

$$\Pr(\mathbf{a}) = N(1, \sigma_a^2 \mathbf{I}) = \frac{1}{(2\pi)^{M/2} \sigma_a^M} \exp\left\{-\frac{1}{2\sigma_a^2} (\mathbf{a} - 1)^T (\mathbf{a} - 1)\right\} \quad (9)$$

Similarly, the bias parameters are modeled as the zero mean Gaussian vector with variance σ_b^2

$$\Pr(\mathbf{b}) = \frac{1}{(2\pi)^{M/2} \sigma_b^M} \exp\left\{-\frac{1}{2\sigma_b^2} \mathbf{b}^T \mathbf{b}\right\}. \quad (10)$$

The single desired HR image is modeled as

$$\Pr(\mathbf{z}) = \frac{1}{(2\pi)^{N/2} |C_z|^{1/2}} \exp\left\{-\frac{1}{2} \mathbf{z}^T |C_z|^{-1} \mathbf{z}\right\}, \quad (11)$$

where C_z is the $N \times N$ covariance matrix of \mathbf{z} . Factoring the exponential term into a sum of products, Equation (11) is rewritten as

$$\Pr(\mathbf{z}) = \frac{1}{(2\pi)^{N/2} |C_z|^{1/2}} \exp\left\{-\frac{1}{2\sigma_z^2} \sum_{i=1}^N \mathbf{z}^T \mathbf{d}_i \mathbf{d}_i^T \mathbf{z}\right\}, \quad (12)$$

where $\mathbf{d}_i = [d_{i,1}, d_{i,2}, \dots, d_{i,N}]^T$ is a set of coefficients. The sum of products is then expressed as

$$\Pr(\mathbf{z}) = \frac{1}{(2\pi)^{N/2} |C_z|^{1/2}} \exp\left\{-\frac{1}{2\sigma_z^2} \sum_{i=1}^N \left(\sum_{j=1}^N d_{i,j} z_j\right)^2\right\}. \quad (13)$$

Natural scenes are characteristically smooth. Therefore a pixel in an image is likely to have a value similar to that of its neighbors. Choosing the coefficient vectors \mathbf{d}_i to be

$$d_{i,j} = \begin{cases} 1 & \text{for } i = j \\ -1/4 & \text{for } j: z_j \text{ is a cardinal neighbor of } z_i \\ 0 & \text{otherwise} \end{cases} \quad (14)$$

emphasizes smoothness in the image by modeling z_i as the average of its four cardinal neighbors plus a Gaussian random variable of variance σ_z^2 .

To simplify the subsequent mathematical development, it is assumed that the observed frames of data $\mathbf{y} = [\mathbf{y}_1, \mathbf{y}_2, \dots, \mathbf{y}_P]^T$ have a mean of 0. If this is not the case, the mean of \mathbf{y} can be subtracted from each frame \mathbf{y}_k prior to applying the algorithm to the set of frames.

B. MAP Estimation

A MAP estimator is used to estimate the values of the HR image \mathbf{z} , nonuniformity gains \mathbf{a} , and nonuniformity biases \mathbf{b} based on the observed frames of data \mathbf{y} and the priors $\Pr(\mathbf{z})$, $\Pr(\mathbf{a})$, and $\Pr(\mathbf{b})$. The maximum *a posteriori* estimate of the HR image \mathbf{z} , gains \mathbf{a} , and biases \mathbf{b} given the observed frames \mathbf{y} can be expressed as

$$\hat{\mathbf{z}}, \hat{\mathbf{a}}, \hat{\mathbf{b}} = \arg \max_{\mathbf{z}, \mathbf{a}, \mathbf{b}} \Pr(\mathbf{z}, \mathbf{a}, \mathbf{b} | \mathbf{y}). \quad (15)$$

where $\hat{\mathbf{z}}$, $\hat{\mathbf{a}}$, and $\hat{\mathbf{b}}$ are estimates of \mathbf{z} , \mathbf{a} , and \mathbf{b} respectively. Applying Bayes' rule, Equation (15) can be rewritten as

$$\hat{\mathbf{z}}, \hat{\mathbf{a}}, \hat{\mathbf{b}} = \arg \max_{\mathbf{z}, \mathbf{a}, \mathbf{b}} \frac{\Pr(\mathbf{y} | \mathbf{z}, \mathbf{a}, \mathbf{b}) \Pr(\mathbf{z}, \mathbf{a}, \mathbf{b})}{\Pr(\mathbf{y})}. \quad (16)$$

Since $\Pr(\mathbf{y})$ is not a function of \mathbf{z} , \mathbf{a} or \mathbf{b} and assuming that the prior distributions of \mathbf{z} , \mathbf{a} and \mathbf{b} are independent, Equation (16) reduces to

$$\hat{\mathbf{z}}, \hat{\mathbf{a}}, \hat{\mathbf{b}} = \arg \max_{\mathbf{z}, \mathbf{a}, \mathbf{b}} \Pr(\mathbf{y} | \mathbf{z}, \mathbf{a}, \mathbf{b}) \Pr(\mathbf{z}) \Pr(\mathbf{a}) \Pr(\mathbf{b}). \quad (17)$$

Since a logarithmic function is monotonically increasing, the MAP estimate in (17) can be expressed as

$$\hat{\mathbf{z}}, \hat{\mathbf{a}}, \hat{\mathbf{b}} = \arg \max_{\mathbf{z}, \mathbf{a}, \mathbf{b}} \left\{ \log \left(\Pr(\mathbf{y} | \mathbf{z}, \mathbf{a}, \mathbf{b}) \Pr(\mathbf{z}) \Pr(\mathbf{a}) \Pr(\mathbf{b}) \right) \right\}. \quad (18)$$

This in turn can be rewritten as

$$\hat{\mathbf{z}}, \hat{\mathbf{a}}, \hat{\mathbf{b}} = \arg \min_{\mathbf{z}, \mathbf{a}, \mathbf{b}} \left\{ L(\mathbf{z}, \mathbf{a}, \mathbf{b}) \right\}, \quad (19)$$

which is a minimization of the cost function L given by

$$L(\mathbf{z}, \mathbf{a}, \mathbf{b}) = -\log[\Pr(\mathbf{y} | \mathbf{z}, \mathbf{a}, \mathbf{b})] - \log[\Pr(\mathbf{z})] - \log[\Pr(\mathbf{a})] - \log[\Pr(\mathbf{b})]. \quad (20)$$

The latter three terms of the cost function in (20) have been previously defined in (11), (9) and (10), but an expression for $\Pr(\mathbf{y} | \mathbf{z}, \mathbf{a}, \mathbf{b})$ must be derived. The observation model in (7) relates an observed frame \mathbf{y}_k to an unknown HR image \mathbf{z} , a set of gains \mathbf{a} , and a set of biases \mathbf{b} .

However, if \mathbf{z} , \mathbf{a} , and \mathbf{b} are known, then the observed frame \mathbf{y}_k reduces to the noise with its mean shifted to the value $(\mathbf{A}\mathbf{W}_k\mathbf{z} + \mathbf{b})$. Therefore, the pdf of \mathbf{y} when \mathbf{z} , \mathbf{a} , and \mathbf{b} are known is

$$\Pr(\mathbf{y} | \mathbf{z}, \mathbf{a}, \mathbf{b}) = \prod_{k=1}^P \frac{1}{(2\pi)^{\frac{M}{2}} \sigma_n^M} \exp \left\{ -\frac{1}{2\sigma_n^2} (\mathbf{y}_k - \mathbf{A}\mathbf{W}_k\mathbf{z} - \mathbf{b})^T (\mathbf{y}_k - \mathbf{A}\mathbf{W}_k\mathbf{z} - \mathbf{b}) \right\}, \quad (21)$$

which is equivalent to

$$\Pr(\mathbf{y} | \mathbf{z}, \mathbf{a}, \mathbf{b}) = \frac{1}{(2\pi)^{\frac{PM}{2}} \sigma_n^{PM}} \exp \left\{ -\sum_{k=1}^P \frac{1}{2\sigma_n^2} (\mathbf{y}_k - \mathbf{A}\mathbf{W}_k\mathbf{z} - \mathbf{b})^T (\mathbf{y}_k - \mathbf{A}\mathbf{W}_k\mathbf{z} - \mathbf{b}) \right\}. \quad (22)$$

By substituting the quantities in (22), (11), (9) and (10) into (20), and removing terms that are not functions of either \mathbf{z} , \mathbf{a} or \mathbf{b} , the cost function becomes

$$L(\mathbf{z}, \mathbf{a}, \mathbf{b}) = \frac{1}{2\sigma_n^2} \sum_{k=1}^P (\mathbf{y}_k - \mathbf{A}\mathbf{W}_k\mathbf{z} - \mathbf{b})^T (\mathbf{y}_k - \mathbf{A}\mathbf{W}_k\mathbf{z} - \mathbf{b}) + \frac{1}{2} \mathbf{z}^T \mathbf{C}_z^{-1} \mathbf{z} + \frac{1}{2\sigma_a^2} (\mathbf{a} - \mathbf{1})^T (\mathbf{a} - \mathbf{1}) + \frac{1}{2\sigma_b^2} \mathbf{b}^T \mathbf{b}. \quad (23)$$

This cost function is a combination of four terms, all of which have a logical purpose. The first term is minimized when a candidate HR image \mathbf{z} , when transformed by the observation model and corrupted by a possible set of gains \mathbf{a} and possible set of biases \mathbf{b} , best matches the set of observed frames \mathbf{y} . The second term is minimized when a potential solution for the HR image is smooth. The third term is small when the gains are centered about one. The fourth term is small when the biases are centered about zero. The variances σ_n^2 , σ_z^2 , σ_a^2 , and σ_b^2 determine the relative weights of the four terms.

The goal of the MAP SR-NUC process is to find a solution for the HR image \mathbf{z} , gains \mathbf{a} , and biases \mathbf{b} that minimizes the cost function in (23). The next two sections present methods for finding such a solution.

C. Gradient Descent Optimization

One approach to finding an optimal solution for the HR image \mathbf{z} , gains \mathbf{a} , and biases \mathbf{b} is to apply a gradient descent procedure. To perform gradient descent, the gradient of the cost

function with respect to \mathbf{z} , the gradient of the cost function with respect to \mathbf{a} , and the gradient of the cost function with respect to \mathbf{b} must first be known.

The gradient of the function in (23) with respect to the vector \mathbf{z} is

$$\nabla_{\mathbf{z}} L(\mathbf{z}, \mathbf{a}, \mathbf{b}) = \frac{1}{\sigma_n^2} \sum_{k=1}^P \mathbf{W}_k^T \mathbf{A}^T (\mathbf{y} - \mathbf{A} \mathbf{W}_k \mathbf{z} - \mathbf{b}) + \mathbf{C}_z^{-1} \mathbf{z}. \quad (24)$$

The final term in (24) can be expressed as

$$\mathbf{C}_z^{-1} \mathbf{z} = [\bar{z}_1, \bar{z}_2, \dots, \bar{z}_N]^T, \quad (25)$$

where

$$\bar{z}_k = \frac{1}{\sigma_z^2} \sum_{i=1}^N d_{i,k} \left(\sum_{j=1}^N d_{i,j} z_j \right). \quad (26)$$

The gradient of the cost function with respect to the vector \mathbf{a} is

$$\nabla_{\mathbf{a}} L(\mathbf{z}, \mathbf{a}, \mathbf{b}) = \frac{1}{\sigma_n^2} \sum_{k=1}^P \mathbf{z}^T \mathbf{W}_k^T (\mathbf{A} \mathbf{W}_k \mathbf{z} + \mathbf{b} - \mathbf{y}_k) + \frac{1}{\sigma_a^2} (\mathbf{a} - \mathbf{1}). \quad (27)$$

The gradient of the cost function with respect to the vector \mathbf{b} is

$$\nabla_{\mathbf{b}} L(\mathbf{z}, \mathbf{a}, \mathbf{b}) = \frac{1}{\sigma_n^2} \sum_{k=1}^P (\mathbf{A} \mathbf{W}_k \mathbf{z} + \mathbf{b} - \mathbf{y}_k) + \frac{1}{\sigma_b^2} \mathbf{b}. \quad (28)$$

The gradient descent procedure begins with an initial estimate of the HR image \mathbf{z} , gains \mathbf{a} , and biases \mathbf{b} . The initial estimate $\mathbf{z}(0)$ of the HR image is chosen to be a low-pass filtered and interpolated version of the first observed frame \mathbf{y}_1 . The initial gain estimate is chosen to be $\mathbf{a}(0) = \mathbf{1}$, where $\mathbf{1}$ is an $M \times 1$ vector of ones. The initial bias estimate is chosen to be $\mathbf{b}(0) = \mathbf{0}$, where $\mathbf{0}$ is an $M \times 1$ vector of zeros. The gradient descent update for an iteration $m = 0, 1, 2, \dots$ is computed using

$$\mathbf{z}(m+1) = \mathbf{z}(m) - \varepsilon(m) \mathbf{g}_z(m), \quad (29)$$

$$\mathbf{a}(m+1) = \mathbf{a}(m) - \varepsilon(m) \mathbf{g}_a(m), \quad (30)$$

and

$$\mathbf{b}(m+1) = \mathbf{b}(m) - \varepsilon(m) \mathbf{g}_b(m), \quad (31)$$

where

$$\mathbf{g}_z(m) = \nabla_z L(\mathbf{z}, \mathbf{a}, \mathbf{b}) \Big|_{\mathbf{z}=\mathbf{z}(m), \mathbf{a}=\mathbf{a}(m), \mathbf{b}=\mathbf{b}(m)}, \quad (32)$$

$$\mathbf{g}_a(m) = \nabla_a L(\mathbf{z}, \mathbf{a}, \mathbf{b}) \Big|_{\mathbf{z}=\mathbf{z}(m), \mathbf{a}=\mathbf{a}(m), \mathbf{b}=\mathbf{b}(m)}, \quad (33)$$

and

$$\mathbf{g}_b(m) = \nabla_b L(\mathbf{z}, \mathbf{a}, \mathbf{b}) \Big|_{\mathbf{z}=\mathbf{z}(m), \mathbf{a}=\mathbf{a}(m), \mathbf{b}=\mathbf{b}(m)}. \quad (34)$$

The step size $\varepsilon(m)$ for a given iteration m is optimized by minimizing

$$L(\mathbf{z}(m+1), \mathbf{a}(m+1), \mathbf{b}(m+1)) = L(\mathbf{z}(m) - \varepsilon(m)\mathbf{g}_z(m), \mathbf{a}(m) - \varepsilon(m)\mathbf{g}_a(m), \mathbf{b}(m) - \varepsilon(m)\mathbf{g}_b(m)) \quad (35)$$

with respect to $\varepsilon(m)$.

The derivative of (35) with respect to $\varepsilon(m)$ is calculated in Appendix A Section 1. The result is set equal to zero, yielding the following result:

$$\begin{aligned} 0 = & \left[2 \cdot \frac{1}{\sigma_z^2} \sum_{k=1}^P (\bar{\mathbf{g}}(m)^T \bar{\mathbf{g}}(m)) \right] \cdot \varepsilon(m)^3 + \left[-3 \cdot \frac{1}{\sigma_z^2} \sum_{k=1}^P (\bar{\mathbf{g}}(m)^T \bar{\mathbf{z}}(m)) \right] \cdot \varepsilon(m)^2 \\ & + \left[\frac{1}{\sigma_a^2} \sum_{k=1}^P (\bar{\mathbf{z}}(m)^T \bar{\mathbf{z}}(m) - 2 \cdot \bar{\mathbf{y}}(m)^T \bar{\mathbf{g}}(m)) + \mathbf{g}_z(m)^T \mathbf{C}_z^{-1} \mathbf{g}_z(m) + \frac{1}{\sigma_a^2} \mathbf{g}_a(m)^T \mathbf{g}_a(m) + \frac{1}{\sigma_b^2} \mathbf{g}_b(m)^T \mathbf{g}_b(m) \right] \cdot \varepsilon(m) \\ & + \left[\frac{1}{\sigma_z^2} \sum_{k=1}^P (\bar{\mathbf{y}}(m)^T \bar{\mathbf{z}}(m)) - \mathbf{z}(m)^T \mathbf{C}_z^{-1} \mathbf{g}_z(m) - \frac{1}{\sigma_a^2} (\mathbf{a}(m) - \mathbf{1})^T \mathbf{g}_a(m) - \frac{1}{\sigma_b^2} \mathbf{b}(m)^T \mathbf{g}_b(m) \right] \end{aligned} \quad (36)$$

where

$$\bar{\mathbf{g}}(m) = \mathbf{G}_A(m) \mathbf{W}_k \mathbf{g}_z(m), \quad (37)$$

$$\bar{\mathbf{z}}(m) = \mathbf{A}(m) \mathbf{W}_k \mathbf{g}_z(m) + \mathbf{G}_A(m) \mathbf{W}_k \mathbf{z}(m) + \mathbf{g}_b(m), \quad (38)$$

$$\bar{\mathbf{y}}(m) = \mathbf{y}_k - \mathbf{A}(m) \mathbf{W}_k \mathbf{z}(m) - \mathbf{b}(m), \quad (39)$$

and \mathbf{G}_A is the $M \times M$ diagonal matrix that contains the elements of \mathbf{g}_a on its main diagonal.

Equation (36) has three solutions, two of which are imaginary and one of which is real. The real solution is chosen as the optimal step size $\varepsilon(m)$, and the gradient descent update is performed

using Equations (29), (30) and (31). This process is continued until the cost changes by less than a predetermined percentage or until a maximum number of iterations is reached.

D. Conjugate-Gradient Optimization

Another approach to finding an optimal solution for the HR image \mathbf{z} , gains \mathbf{a} , and biases \mathbf{b} is to apply a conjugate-gradient procedure. Conjugate-gradient is an iterative technique that is similar to gradient descent. Conjugate-gradient is considered advantageous over gradient descent since it is generally able to converge more quickly with only minor additional computation. The steps presented here to solve for the HR image \mathbf{z} , gains \mathbf{a} , and biases \mathbf{b} are an extension of the approach outlined in [39] which solves for only the HR image.

The conjugate-gradient update for an iteration $m = 0, 1, 2, \dots$ is computed using

$$\mathbf{z}(m+1) = \mathbf{z}(m) - \varepsilon(m) \mathbf{d}_z(m), \quad (40)$$

$$\mathbf{a}(m+1) = \mathbf{a}(m) - \varepsilon(m) \mathbf{d}_a(m), \quad (41)$$

and

$$\mathbf{b}(m+1) = \mathbf{b}(m) - \varepsilon(m) \mathbf{d}_b(m). \quad (42)$$

Here ε is the step size and \mathbf{d}_z , \mathbf{d}_a and \mathbf{d}_b are the conjugate-gradient vectors of size $N \times 1$, $M \times 1$, and $M \times 1$ respectively. At the initial update for iteration $m = 0$, the gradient descent vectors in (32), (33) and (34) are used to define the conjugate-gradient vectors to be

$$\mathbf{d}_z(0) = -\mathbf{g}_z(0), \quad (43)$$

$$\mathbf{d}_a(0) = -\mathbf{g}_a(0) \quad (44)$$

and

$$\mathbf{d}_b(0) = -\mathbf{g}_b(0). \quad (45)$$

For updates of subsequent iterations $m = 1, 2, \dots$ the conjugate-gradient vectors are

$$\mathbf{d}_z(m+1) = -\mathbf{g}_z(m+1) + \frac{\mathbf{g}_z^T(m+1)\mathbf{g}_z(m+1)}{\mathbf{g}_z^T(m)\mathbf{g}_z(m)} \mathbf{d}_z(m), \quad (46)$$

$$\mathbf{d}_a(m+1) = -\mathbf{g}_a(m+1) + \frac{\mathbf{g}_a^T(m+1)\mathbf{g}_a(m+1)}{\mathbf{g}_a^T(m)\mathbf{g}_a(m)}\mathbf{d}_a(m), \quad (47)$$

and

$$\mathbf{d}_b(m+1) = -\mathbf{g}_b(m+1) + \frac{\mathbf{g}_b^T(m+1)\mathbf{g}_b(m+1)}{\mathbf{g}_b^T(m)\mathbf{g}_b(m)}\mathbf{d}_b(m). \quad (48)$$

The step size $\varepsilon(m)$ for a given iteration m is optimized by minimizing

$$L(\mathbf{z}(m+1), \mathbf{a}(m+1), \mathbf{b}(m+1)) = L(\mathbf{z}(m) - \varepsilon(m)\mathbf{d}_z(m), \mathbf{a}(m) - \varepsilon(m)\mathbf{d}_a(m), \mathbf{b}(m) - \varepsilon(m)\mathbf{d}_b(m)) \quad (49)$$

with respect to $\varepsilon(m)$.

The derivative of (49) with respect to $\varepsilon(m)$ is calculated in Appendix A Section 2. The result is set equal to zero, yielding the following result:

$$\begin{aligned} 0 = & \left[2 \cdot \frac{1}{\sigma_a^2} \sum_{k=1}^P (\bar{\mathbf{d}}(m)^T \bar{\mathbf{d}}(m)) \right] \cdot \varepsilon(m)^3 + \left[-3 \cdot \frac{1}{\sigma_a^2} \sum_{k=1}^P (\bar{\mathbf{d}}(m)^T \tilde{\mathbf{z}}(m)) \right] \cdot \varepsilon(m)^2 \\ & + \left[\frac{1}{\sigma_a^2} \sum_{k=1}^P (\tilde{\mathbf{z}}(m)^T \tilde{\mathbf{z}}(m) - 2 \cdot \bar{\mathbf{y}}(m)^T \bar{\mathbf{d}}(m)) + \mathbf{d}_z(m)^T \mathbf{C}_z^{-1} \mathbf{d}_z(m) + \frac{1}{\sigma_a^2} \mathbf{d}_a(m)^T \mathbf{d}_a(m) + \frac{1}{\sigma_b^2} \mathbf{d}_b(m)^T \mathbf{d}_b(m) \right] \cdot \varepsilon(m) \\ & + \frac{1}{\sigma_a^2} \sum_{k=1}^P (\bar{\mathbf{y}}(m)^T \tilde{\mathbf{z}}(m)) - \mathbf{z}(m)^T \mathbf{C}_z^{-1} \mathbf{d}_z(m) - \frac{1}{\sigma_a^2} (\mathbf{a}(m) - \mathbf{1})^T \mathbf{d}_a(m) - \frac{1}{\sigma_b^2} \mathbf{b}(m)^T \mathbf{d}_b(m) \end{aligned} \quad (50)$$

where

$$\bar{\mathbf{d}}(m) = \mathbf{D}_A(m) \mathbf{W}_k \mathbf{d}_z(m), \quad (51)$$

$$\tilde{\mathbf{z}}(m) = \mathbf{A}(m) \mathbf{W}_k \mathbf{d}_z(m) + \mathbf{D}_A(m) \mathbf{W}_k \mathbf{z}(m) + \mathbf{d}_b(m), \quad (52)$$

and \mathbf{D}_A is the $M \times M$ diagonal matrix that contains the elements of \mathbf{d}_a on its main diagonal.

Equation (50) has three solutions, two of which are imaginary and one of which is real. The real solution is chosen as the optimal step size $\varepsilon(m)$, and the conjugate-gradient update is performed using Equations (40), (41) and (42). This process is continued until the cost changes by less than a predetermined percentage or until a maximum number of iterations is reached.

E. Bias-Only Simplification

If the gain nonuniformity parameters are assumed to be unity, the MAP estimation framework reduces to a useful version of the MAP SR-NUC algorithm that estimates only the HR image and the bias nonuniformity parameters. Under these conditions, the bias-only version is able to produce an adequate nonuniformity correction and an accurate estimate of the HR image with fewer calculations than the full MAP SR-NUC algorithm.

This approach, referred to here as the Bias-Only MAP SR-NUC algorithm, was co-developed by the author and published in [5]. Originally, this version of the algorithm was derived from a model that included only the HR image and bias nonuniformity. Here, it is shown that the results are equivalent when the full SR-NUC algorithm is employed but with constant unity gain.

The assumption that the gain nonuniformity parameters are unity denotes that the vector \mathbf{a} is the $M \times 1$ vector of all ones and \mathbf{A} is the $M \times M$ identity matrix. The cost function in (23) then reduces to

$$L(\mathbf{z}, \mathbf{b}, \mathbf{a}) = \frac{1}{2\sigma_n^2} \sum_{k=1}^P (\mathbf{y}_k - \mathbf{W}_k \mathbf{z} - \mathbf{b})^T (\mathbf{y}_k - \mathbf{W}_k \mathbf{z} - \mathbf{b}) + \frac{1}{2} \mathbf{z}^T \mathbf{C}_z^{-1} \mathbf{z} + \frac{1}{2\sigma_b^2} \mathbf{b}^T \mathbf{b}. \quad (53)$$

The cost function in (53) is no longer a function of \mathbf{a} , so it can be rewritten as

$$L(\mathbf{z}, \mathbf{b}) = \frac{1}{2\sigma_n^2} \sum_{k=1}^P (\mathbf{y}_k - \mathbf{W}_k \mathbf{z} - \mathbf{b})^T (\mathbf{y}_k - \mathbf{W}_k \mathbf{z} - \mathbf{b}) + \frac{1}{2} \mathbf{z}^T \mathbf{C}_z^{-1} \mathbf{z} + \frac{1}{2\sigma_b^2} \mathbf{b}^T \mathbf{b}. \quad (54)$$

The gradient descent optimization described in Section C requires knowledge of the gradients of the cost function with respect to the vectors \mathbf{z} and \mathbf{b} . The gradient of the cost function in (54) with respect to the vector \mathbf{z} is

$$\nabla_{\mathbf{z}} L(\mathbf{z}, \mathbf{b}) = \frac{1}{\sigma_n^2} \sum_{k=1}^P \mathbf{W}_k^T (\mathbf{W}_k \mathbf{z} + \mathbf{b} - \mathbf{y}_k) + \mathbf{C}_z^{-1} \mathbf{z}, \quad (55)$$

and the gradient of (54) with respect to the vector \mathbf{b} is

$$\nabla_{\mathbf{b}} L(\mathbf{z}, \mathbf{b}) = \frac{1}{\sigma_n^2} \sum_{k=1}^P (\mathbf{W}_k \mathbf{z} + \mathbf{b} - \mathbf{y}_k) + \frac{1}{\sigma_b^2} \mathbf{b}. \quad (56)$$

Since \mathbf{a} is the $M \times 1$ vector of all ones and \mathbf{A} is the $M \times M$ identity matrix, and noting that the gradient of (48) with respect to the vector \mathbf{a} is

$$\nabla_{\mathbf{a}} L(\mathbf{z}, \mathbf{b}) = \mathbf{0}, \quad (57)$$

the expression in Equation (36) reduces to

$$0 = \left[\frac{1}{\sigma_n^2} \sum_{k=1}^P \left((\mathbf{W}_k \mathbf{g}_z(m) + \mathbf{g}_b(m))^T (\mathbf{W}_k \mathbf{g}_z(m) + \mathbf{g}_b(m)) \right) + \mathbf{g}_z^T(m) C_z^{-1} \mathbf{g}_z(m) + \frac{1}{\sigma_b^2} \mathbf{g}_b^T(m) \mathbf{g}_b(m) \right] \varepsilon(m) \\ + \left[\frac{1}{\sigma_n^2} \sum_{k=1}^P \left((\mathbf{y}_k - \mathbf{W}_k \mathbf{z}(m) - \mathbf{b}(m))^T (\mathbf{W}_k \mathbf{g}_z(m) + \mathbf{g}_b(m)) \right) - \mathbf{z}^T(m) C_z^{-1} \mathbf{g}_z(m) - \frac{1}{\sigma_b^2} \mathbf{b}^T(m) \mathbf{g}_b(m) \right] \quad (58)$$

Solving for $\varepsilon(m)$ and reordering terms yields

$$\varepsilon(m) = \frac{\frac{1}{\sigma_n^2} \sum_{k=1}^P (\mathbf{W}_k \mathbf{g}_z(m) + \mathbf{g}_b(m))^T (\mathbf{W}_k \mathbf{z}(m) + \mathbf{b}(m) - \mathbf{y}_k) + \mathbf{g}_z^T(m) C_z^{-1} \mathbf{z}(m) + \frac{1}{\sigma_b^2} \mathbf{g}_b^T(m) \mathbf{b}(m)}{\frac{1}{\sigma_n^2} \sum_{k=1}^P (\mathbf{W}_k \mathbf{g}_z(m) + \mathbf{g}_b(m))^T (\mathbf{W}_k \mathbf{g}_z(m) + \mathbf{g}_b(m)) + \mathbf{g}_z^T(m) C_z^{-1} \mathbf{g}_z(m) + \frac{1}{\sigma_b^2} \mathbf{g}_b^T(m) \mathbf{g}_b(m)} \quad (59)$$

Note that the key results in (54), (55), (56) and (59) match the equivalent results in [5].

CHAPTER IV

EXPERIMENTAL RESULTS

In this chapter, a number of experimental results are presented to demonstrate the efficacy of the MAP estimator. The first set of results uses simulated imagery to allow for quantitative analysis. The second set uses real data from a forward looking infrared (FLIR) imager to evaluate the algorithm under real-world conditions.

Several variations of the MAP-SR NUC algorithm are examined in this chapter. The differences relate to which parameters are simultaneously estimated by the MAP estimator. The details of each variation are listed in Table 2.

	Estimates HR Image	Estimates Gains	Estimates Biases
MAP SR-NUC	✓	✓	✓
Bias-Only MAP SR-NUC	✓		✓
MAP NUC		✓	✓
Bias-Only MAP NUC			✓

Table 2. Variations of the MAP SR-NUC Algorithm.

A. Simulated Data

To provide a means for quantitative performance evaluation, the single 8-bit HR grayscale image shown in Figure 18(a) is used to create a simulated set of LR frames. Specifically, the HR image is translated by random pixel shifts, downsampled, and corrupted by nonuniformity and noise to create a set of 64 “observed” frames. A scatter plot of the random motion parameters used to create the frames is shown in Figure 19. Relatively large shifts are

used to provide diversity for gain nonuniformity estimation. Downsampling is performed using $L_x = 4$ horizontally and $L_y = 4$ vertically. The artificially introduced gain nonuniformity, bias nonuniformity, and noise have Gaussian distributions with variances $\sigma_a^2 = 0.2$, $\sigma_b^2 = 40$, and $\sigma_n^2 = 1$ respectively. The gain and bias nonuniformity parameters used to create the simulated frames are shown in Figure 20. The nonuniformity parameters are held constant across the entire frame sequence, but an independent set of noise parameters is used to corrupt each individual frame.

The first simulated LR image, translated slightly and downsampled but not yet corrupted by nonuniformity or noise, is shown in Figure 18(b). The first observed LR image corrupted by nonuniformity and noise is shown in Figure 18(c). This set of 64 LR frames provides the basis for quantitatively evaluating performance. The results of applying NUC algorithms and SR algorithms to this data set can be compared with the original HR image and with the nonuniformity that was originally used to corrupt the HR frame.

In the following results, the gradient descent procedure outlined in Chapter III Section C is utilized. The gradient descent is allowed 20 iterations, which typically results in the cost decreasing by less than 0.01% at the final iteration. Additionally, exact random motion parameters are used in order to assess the estimator independently from the motion estimation. Finally, the mean absolute error (MAE) metric defined in Chapter II is calculated using the center 100x100 pixels within LR image results and the center 400x400 within HR image results.

1. MAP SR-NUC Results

The MAP SR-NUC algorithm is used to process the $P = 64$ frames. Figure 21 shows that, as expected, the value of the cost function decreases with each iteration. The output of the joint MAP SR-NUC algorithm, shown in Figure 22(a), closely resembles the original HR image and shows no visible nonuniformity. Figure 22(b) shows that the bulk of the gain estimates are random in nature, and a close inspection shows that they generally match the true gain parameters. The dark regions near the edges of the array of gain parameters are caused by frame-

to-frame motion that produces incomplete sets of matching HR image information. "Edge effects" such as these are common in image processing and are considered immaterial to the overall performance of the algorithm. The algorithm has difficulty estimating the gain parameters in the lower right of the array because most of the input scene information is at similar signal levels. The bias estimates shown in Figure 22(c) closely match the true bias parameters.

To produce these results, the convergence of the gain parameters is prevented during the first four iterations of the gradient descent procedure. This allows the HR image estimate to initially converge to a somewhat accurate result. Simulations have shown that if gain convergence is not prevented (for at least two iterations), then the HR image will fail to converge regardless of the number of iterations that are allowed. It is believed that this is a consequence of the large number of parameters that are being simultaneously estimated. Use of an alternative optimization technique may avoid this requirement. Throughout the remainder of the simulations in this chapter, however, gain parameter convergence is prevented for the first four iterations.

2. NUC Performance

There are several variations of the MAP SR-NUC algorithm, each of which provides nonuniformity correction. The nonuniformity parameters can be estimated jointly with the HR image parameters or can be estimated alone (which is equivalent to the MAP SR-NUC algorithm with $L_x = L_y = 1$). Additionally, the MAP SR-NUC algorithm can be reduced to a bias-only version that assumes $\mathbf{a} = \mathbf{1}$ and estimates only the bias nonuniformity parameters. The NUC capabilities of the following four variations are evaluated here:

- MAP SR-NUC algorithm
- Bias-Only MAP SR-NUC algorithm ($\mathbf{a} = \mathbf{1}$)
- MAP NUC algorithm ($L_x = L_y = 1$)
- Bias-Only MAP NUC algorithm ($L_x = L_y = 1, \mathbf{a} = \mathbf{1}$)

Two other scene-based NUC approaches are chosen as benchmarks. The first is the bias correction of the registration-based NUC algorithm proposed in [17]. The second is the local constant statistics (LCS) NUC method presented in [10-12] that estimates both gain and bias parameters. In place of the documented steepest descent approach, the LCS algorithm is implemented using a linear least squares fit.

Initially, the estimates of the nonuniformity parameters provided by each algorithm are evaluated against the known parameters used to create the sequence. In Figure 23(a), the mean absolute error of the gain estimates versus the original gain parameters is plotted as a function of the number of input frames. For those algorithms that do not estimate gain parameters, unity gain is assumed. The results show that the joint MAP SR-NUC algorithm provides a slightly better estimate of the gain parameters than does the MAP NUC algorithm, and that both MAP approaches outperform the benchmark LCS NUC algorithm. Figure 23(b) shows that the joint MAP SR-NUC algorithm also offers the best estimate of the bias parameters. It is evident, however, that the error of the bias estimates is generally high for all of the algorithms. This is because the gain nonuniformity that is present in the data is incorrectly included in the bias estimates (as discussed in Chapter II Section B). Even the techniques that include gain nonuniformity in their models tend to include some amount of gain nonuniformity in their bias estimates. Interestingly, an inaccurate set of gain and bias parameters may perform an extremely accurate correction at a single operating point, but generally will not perform well across the dynamic range. These two performance scenarios are examined in the following paragraphs.

The performance of a scene-based NUC algorithm can be partially measured by its ability to correct the input frame sequence used as the basis for its nonuniformity parameter estimates. Figure 24 shows the first image in the simulated frame sequence processed using each scene-based NUC approach. All demonstrate improvement upon the corrupted image shown in Figure 18(c) and are very similar to the LR frame prior to nonuniformity correction shown in Figure 18(b). To further evaluate the NUC performance of the algorithms, the absolute error of the

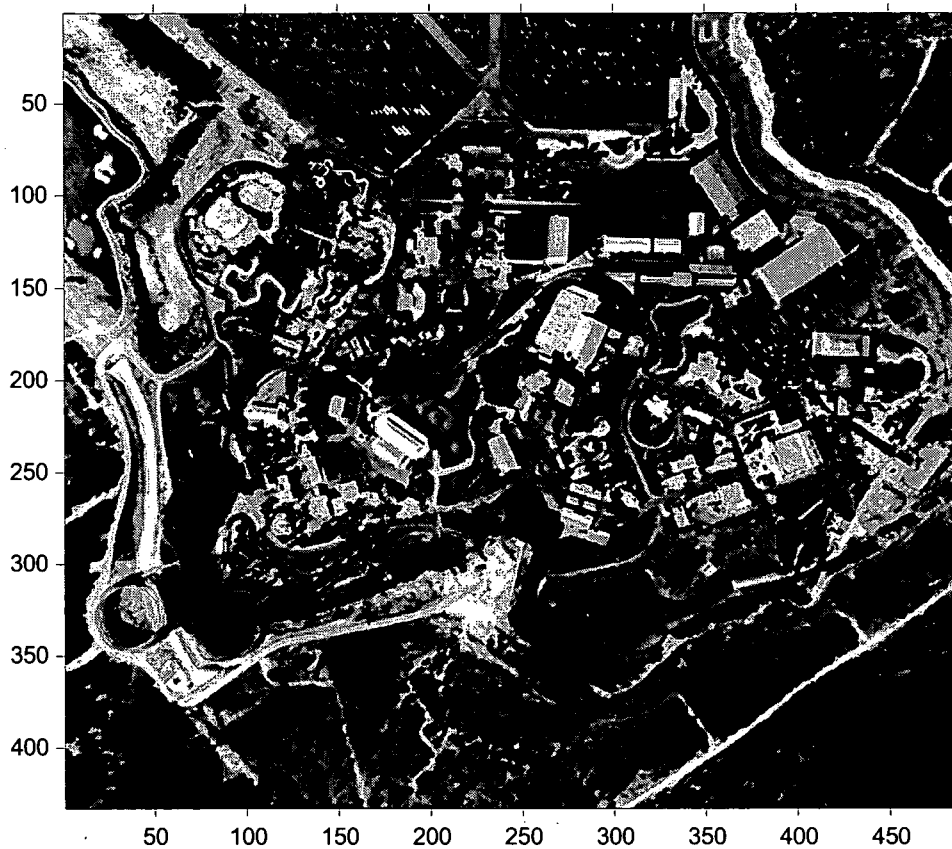
images in Figures 24(a-f) versus the image in Figure 18(b) is calculated. The results shown in Figures 25(a-f) use one grayscale value to display 0.5 counts of error, which makes the error twice as evident as it would be on a standard 8-bit display. To avoid edge effects, only the center 100×100 of each image is shown. The LCS error image indicates significant levels of medium frequency error, which is due to the lack of frame-to-frame motion in the LR frame sequence. The algorithms that only support bias nonuniformity estimation show a moderate level of error, most of which is high frequency in nature. Finally, the MAP NUC and MAP SR-NUC approaches, which estimate both gain and bias nonuniformity, show very little error at all.

The set of simulated LR frames corrected using the NUC estimates of each algorithm is compared with the set of simulated LR frames prior to corruption by nonuniformity. The error plots in Figure 26 show that the joint MAP SR-NUC and the MAP NUC algorithms outperform the three algorithms that estimate bias parameters only, and significantly outperform the LCS NUC algorithm. For a small number of frames P , the Bias-Only MAP SR-NUC algorithm outperforms the Bias-Only MAP NUC algorithm slightly, and the MAP SR-NUC algorithm outperforms the MAP NUC algorithm slightly. These results indicate that estimating nonuniformity parameters jointly with HR image parameters leads to a more accurate NUC, possibly because access to an HR image makes interpolation more accurate. Additionally, when given enough frames, those algorithms that estimate only bias nonuniformity approach one level of error while those algorithms that estimate both gain and bias nonuniformity approach a second, lower level of error (with the exception of the LCS NUC algorithm).

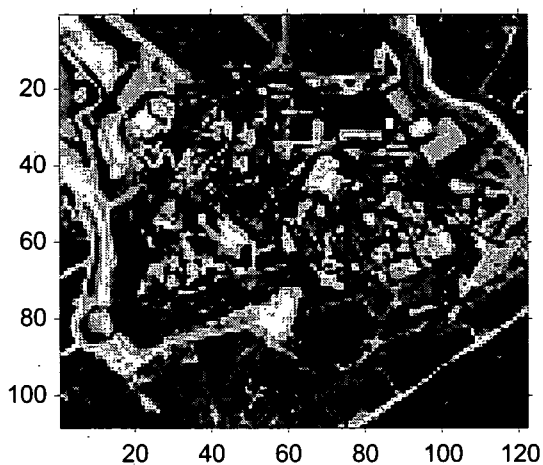
Scene-based NUC performance can also be measured by the ability to use nonuniformity estimates to correct future frame sequences. It is possible that the signal levels within these unknown frames may utilize different portions of the dynamic range than the original frame sequence, so it is important that nonuniformity parameters provide accurate correction across the entire dynamic range. Performance is measured using simulated "blackbody" images, which are frames of constant signal level. These blackbody images are created for points spanning the

dynamic range and are then corrupted by nonuniformity in the same manner as the LR frames are corrupted. The NUC parameters estimated by each algorithm are then used to correct these frames. Figure 27 shows the results of the correction on the center 100×100 pixels of a blackbody frame at a 150 digital count signal level. All images are displayed with each grayscale value representing one digital count of error and with middle gray at 150 digital counts, so a perfectly corrected frame would be middle gray with no variations. The LCS algorithm is able to remove most of the strong high frequency nonuniformity, but significant medium frequency components remain. The bias-only algorithms are significantly outperformed by the MAP SR-NUC and MAP NUC algorithms, and the MAP SR-NUC results are slightly better than the MAP NUC results. Both of these algorithms have some minor difficulty towards the lower-right of the FPA. This is a location where most of the input frame sequence information is at intensities in the same portion of the dynamic range, making it difficult to accurately estimate gain parameters.

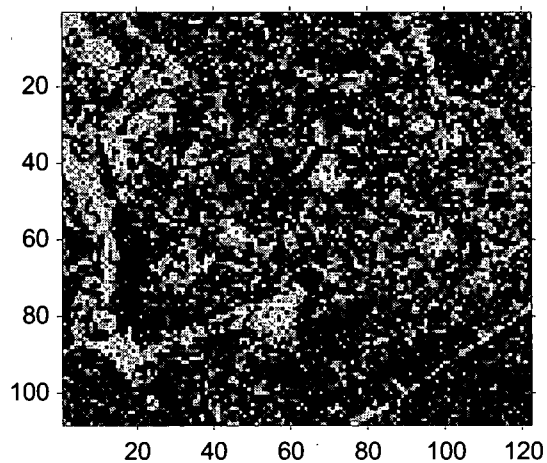
Next, blackbody frames corrected using the NUC estimates of each algorithm are compared with the original uncorrupted blackbody frames. Figure 28 shows MAE versus blackbody frame signal level. Near the average scene value of the original data set, all algorithms provide an accurate correction. However, away from the average scene value, the algorithms that perform gain correction offer significantly better performance than those that perform a bias-only correction. In particular, the MAP SR-NUC and MAP NUC approaches fare better than the LCS algorithm, with the MAP SR-NUC algorithm narrowly providing the best overall performance.



(a)



(b)



(c)

Figure 18. Creation of the simulated data set. (a) Grayscale image used to create the set of simulated frames (b) First simulated LR image not yet corrupted by nonuniformity (c) First observed LR image corrupted by nonuniformity and noise.

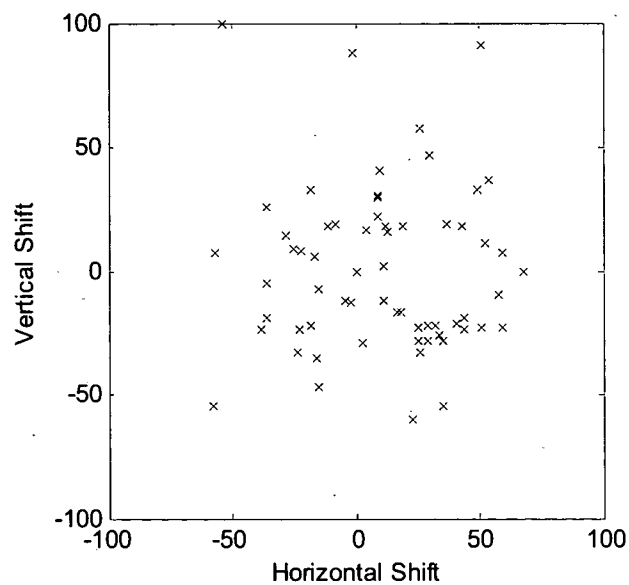


Figure 19. Random pixel shifts used to create the set of $P = 64$ simulated frames

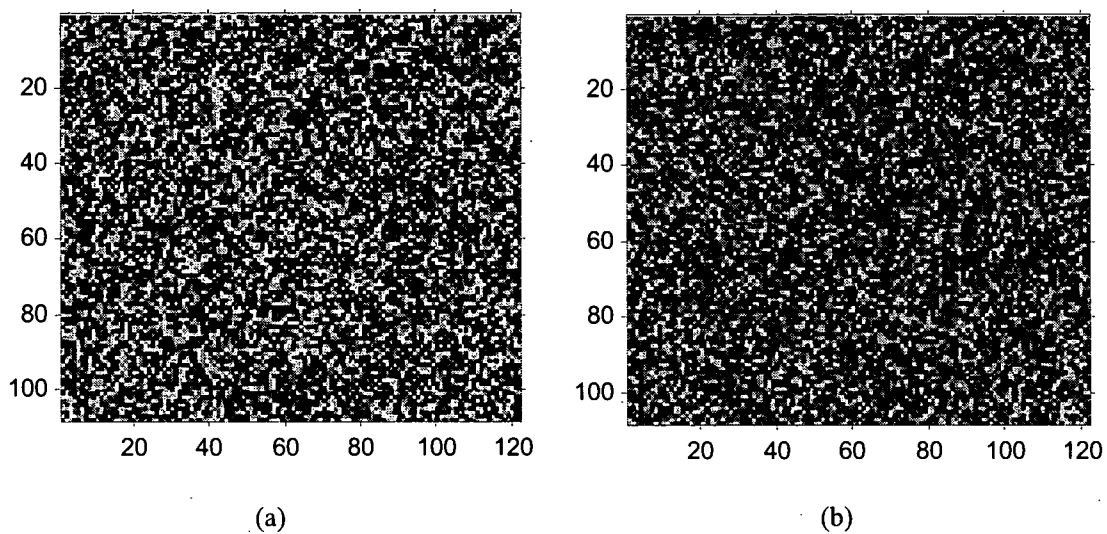


Figure 20. Nonuniformity parameters used to create the set of simulated frames (a) gain (b) bias

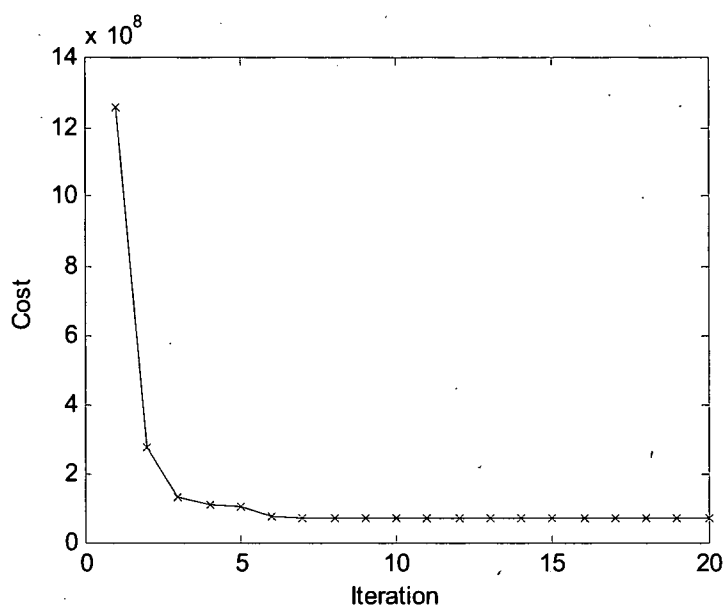
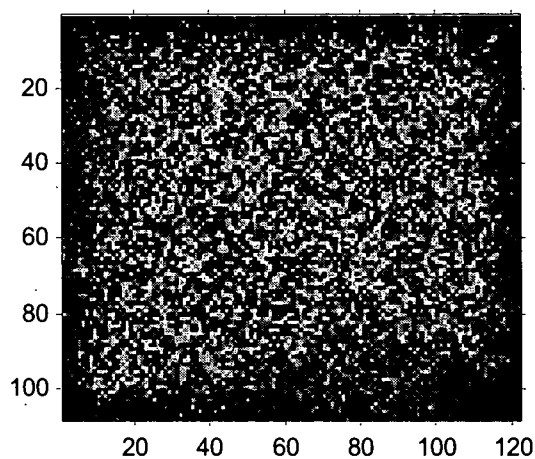


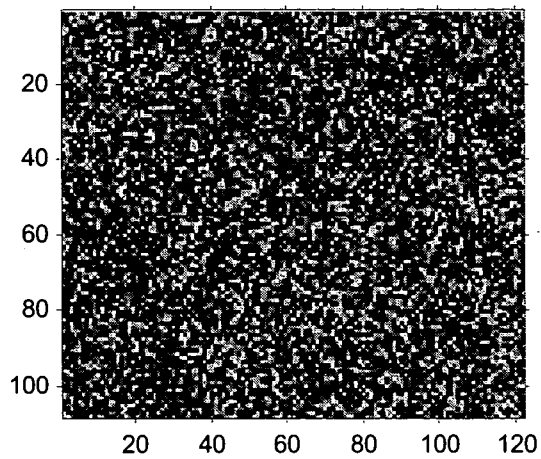
Figure 21. Value of the MAP SR-NUC cost function when processing the $P = 64$ frame simulated data set.



(a)

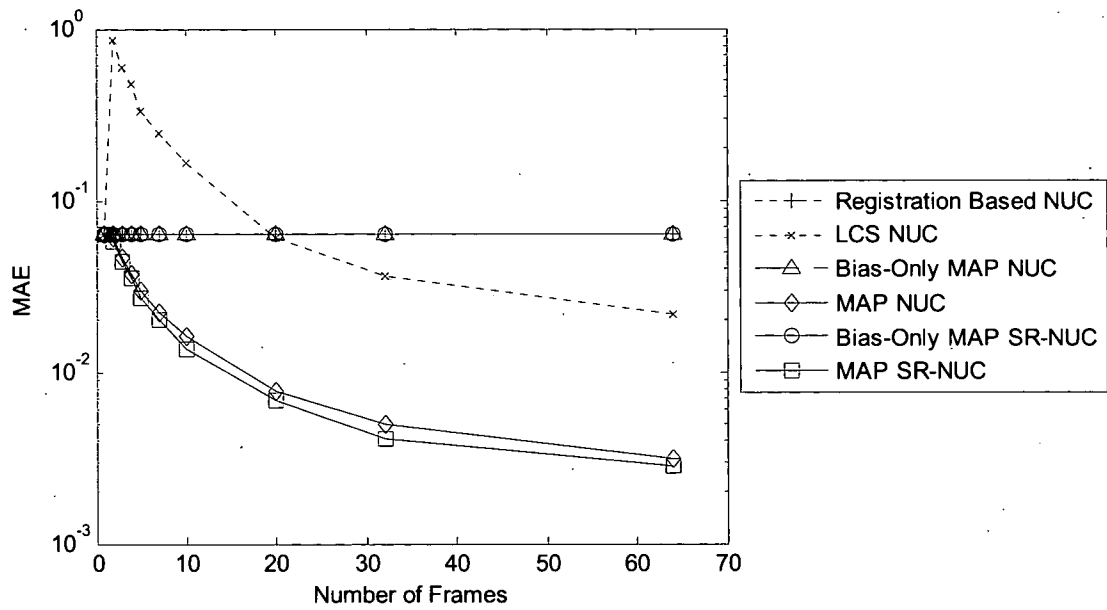


(b)

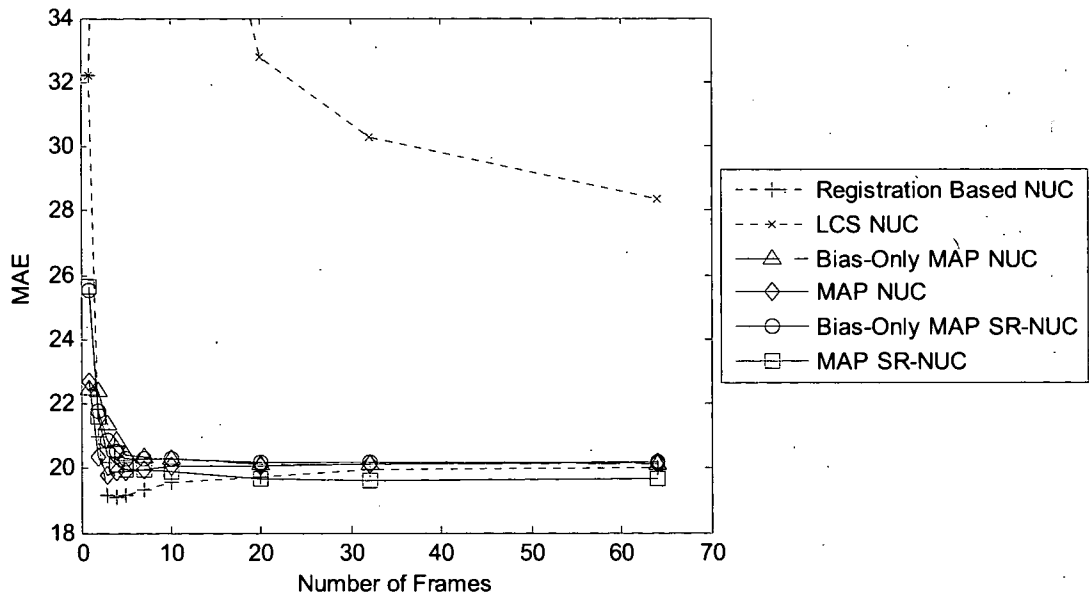


(c)

Figure 22. MAP SR-NUC estimates of the (a) HR image, (b) gain parameters, and (c) bias parameters.



(a)



(b)

Figure 23. Mean absolute error of the (a) gain estimates and (b) bias estimates as a function of the number of input frames P .

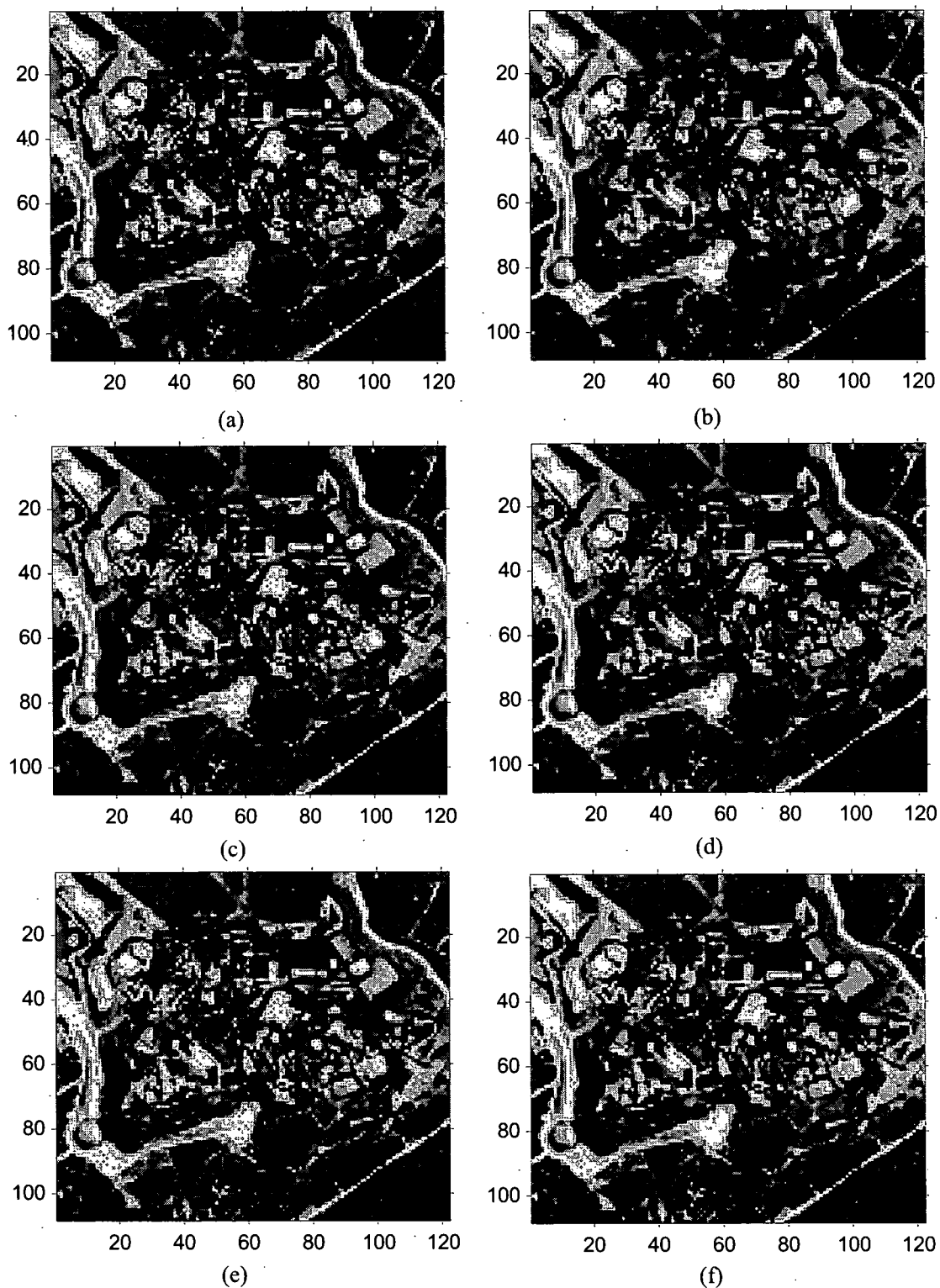
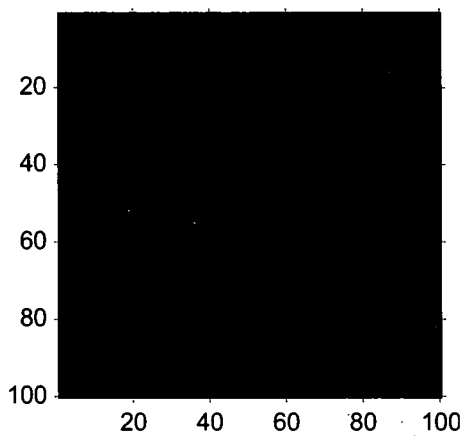
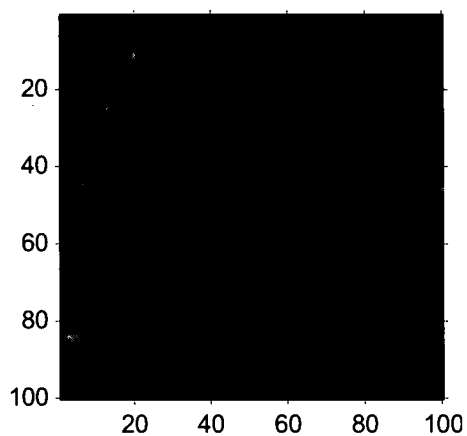


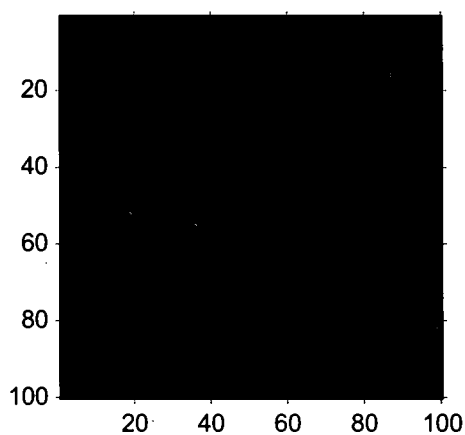
Figure 24. Images corrected for nonuniformity using (a) registration-based (b) local constant statistics (c) Bias-Only MAP NUC (d) MAP NUC (e) Bias-Only MAP SR-NUC (f) MAP SR-NUC



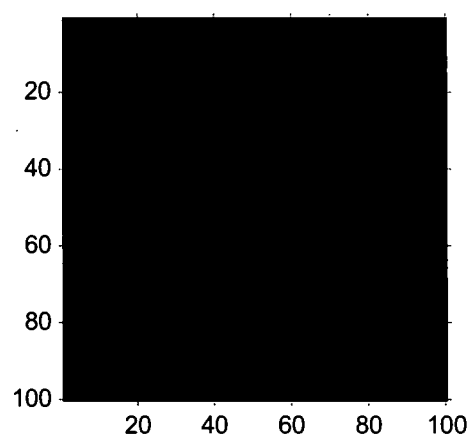
(a)



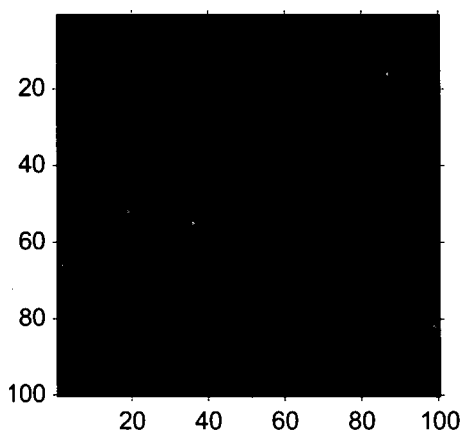
(b)



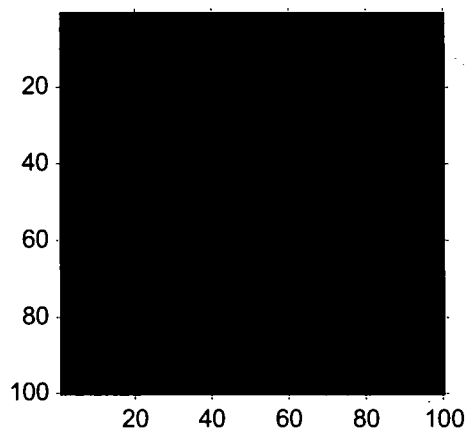
(c)



(d)



(e)



(f)

Figure 25. Absolute error of the nonuniformity correction when using (a) registration-based (b) local constant statistics (c) Bias-Only MAP NUC (d) MAP NUC (e) Bias-Only MAP SR-NUC (f) MAP SR-NUC. All images are displayed using the same scaling, where black is zero error and white is 128 counts of error.

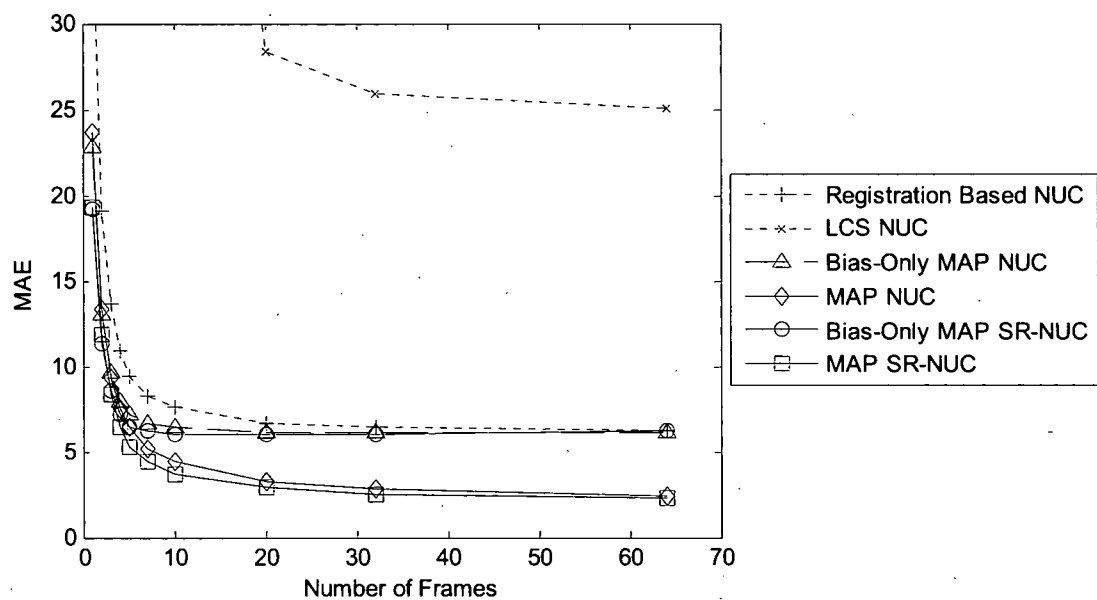
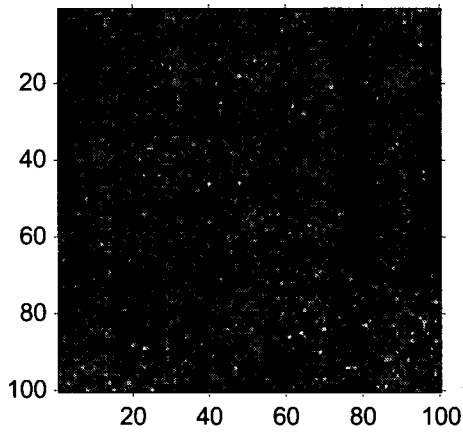
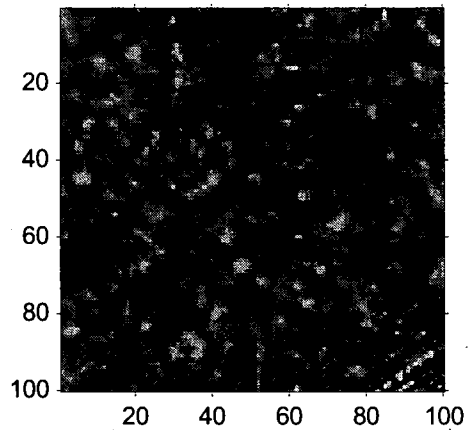


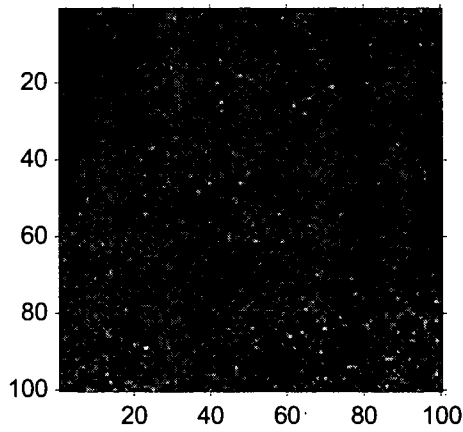
Figure 26. Mean absolute error of the set of simulated LR frames corrected using estimated NUC parameters.



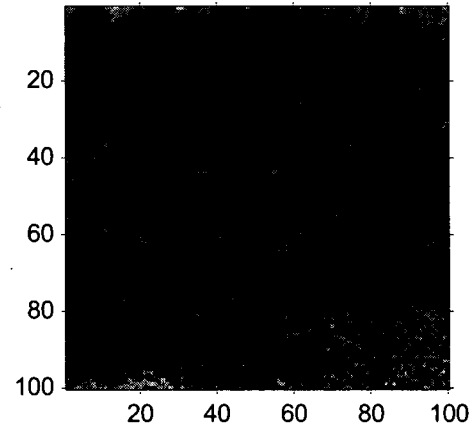
(a)



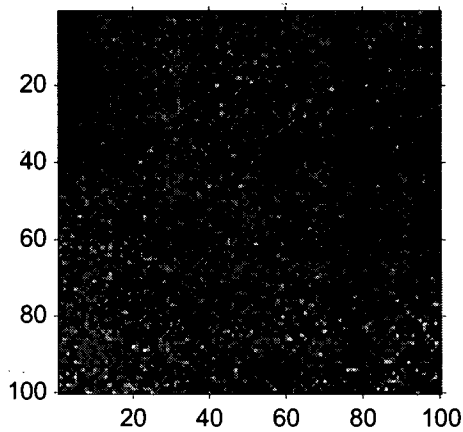
(b)



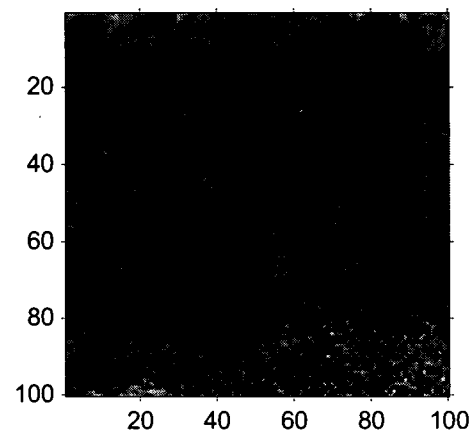
(c)



(d)



(e)



(f)

Figure 27. Simulated 150 count blackbody image nonuniformity corrected using (a) registration-based (b) local constant statistics (c) Bias-Only MAP NUC (d) MAP NUC (e) Bias-Only MAP SR-NUC (f) MAP SR-NUC. All images are displayed using the same scaling, where middle gray is 150 digital counts and each grayscale value represents one digital count of error.

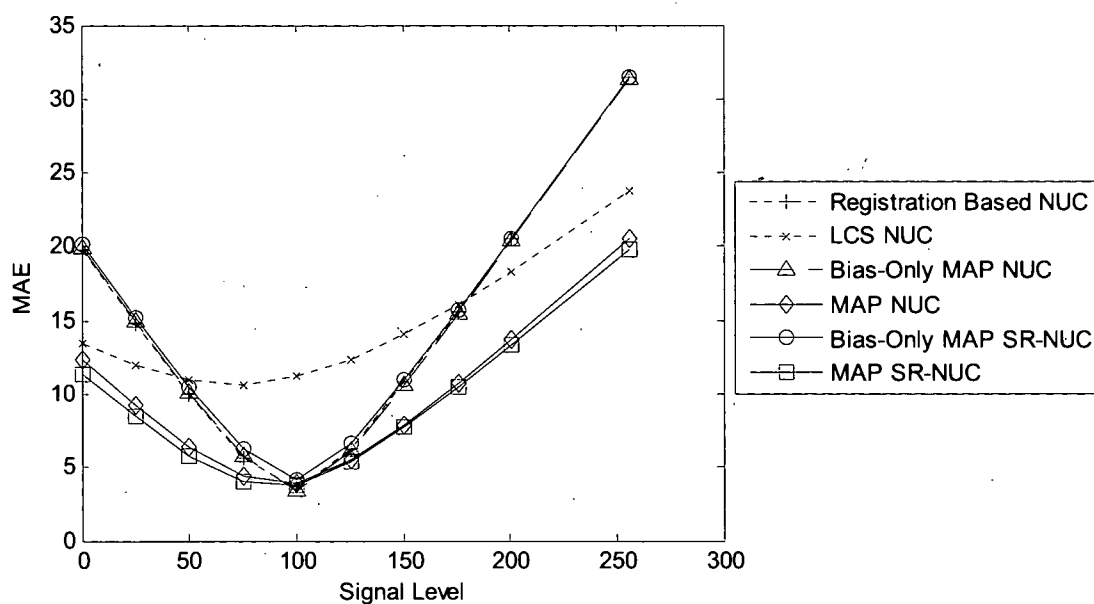


Figure 28. Mean absolute error of simulated blackbody frames corrected using estimated NUC parameters. Samples cover the entire 8-bit input dynamic range.

2. SR Performance

In the present context where input frames contain high levels of nonuniformity, SR must be evaluated in conjunction with NUC. The following combinations of nonuniformity correction and HR image estimation are examined:

- Registration-based NUC followed by bilinear interpolation
- Local constant statistics NUC followed by bilinear interpolation
- MAP NUC followed by bilinear interpolation
- MAP SR-NUC
- MAP NUC followed by MAP SR
- Bias-Only MAP SR-NUC
- Bias-Only MAP NUC followed by MAP SR

The pure MAP SR algorithm is obtained using the MAP estimator presented here without the bias terms, and is essentially the same as that in [38, 39]. The HR image results for these seven approaches when $P = 64$ frames are displayed in Figures 29-35.

Figure 36 plots the MAE of the HR image estimates versus the number of input frames for five of the combinations listed above. The error plot shows that the two combinations that incorporate SR outperform the three combinations that utilize bilinear interpolation. In particular, MAP SR shows significantly less error than bilinear interpolation when both use the same MAP NUC technique for nonuniformity correction. Figures 29-31 show that the interpolation-based combinations lack high frequency detail. Figures 32-33 demonstrate that the combination of NUC and SR provides significant high frequency information. In particular, the HR image estimate of MAP NUC followed by MAP SR in Figure 33 is remarkably similar to the original HR image in Figure 18(a).

Figure 37 compares the MAE of the combinations that involve both MAP NUC and MAP SR. For a large number of frames ($P \geq 20$), MAP NUC followed by MAP SR demonstrates a

remarkable level of performance. The HR image estimate of the MAP SR-NUC algorithm has slightly more error than the other approaches. It is believed that the MAP SR-NUC algorithm has difficulty because of the sheer number of parameters that must be jointly estimated (1.5x more than either MAP NUC or Bias-Only MAP SR-NUC). The Bias-Only MAP SR-NUC and Bias-Only MAP NUC followed by MAP SR approaches converge to approximately the same level of error, suggesting a limit to SR performance when gain nonuniformity is not accounted for. The HR image results in Figures 29-35 for $P = 64$ frames support the above discussion.

Figure 37 shows that for a small number of frames, the joint MAP SR-NUC approaches contain less HR image error than the corresponding two-step methods. The HR output images for these approaches are shown in Figures 38-41 for $P = 7$ frames. The adverse effects of nonuniformity errors are more evident in the two-step algorithm results in Figures 38 and 40 than in the joint SR-NUC algorithm results in Figures 39 and 41. The high frequency error that is evident in the two-step algorithm results may be a consequence of interpolation errors in the motion model. Such errors are reduced for the joint SR-NUC approaches because interpolation is performed on the HR grid. For a small number of frames ($P < 10$), the joint MAP SR-NUC approach offers the most accurate HR image performance.

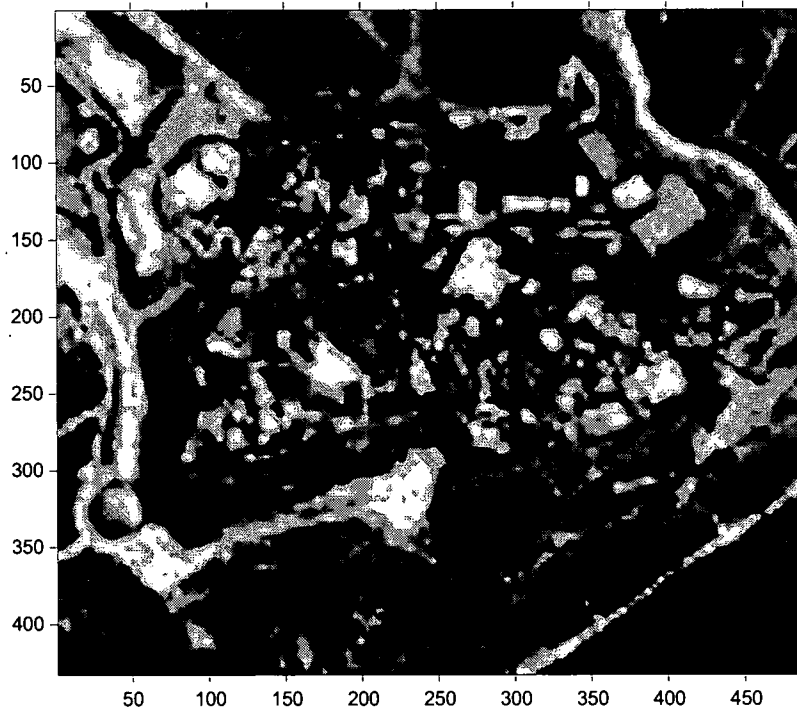


Figure 29. HR image output of registration-based NUC followed by bilinear interpolation when $P = 64$ frames.

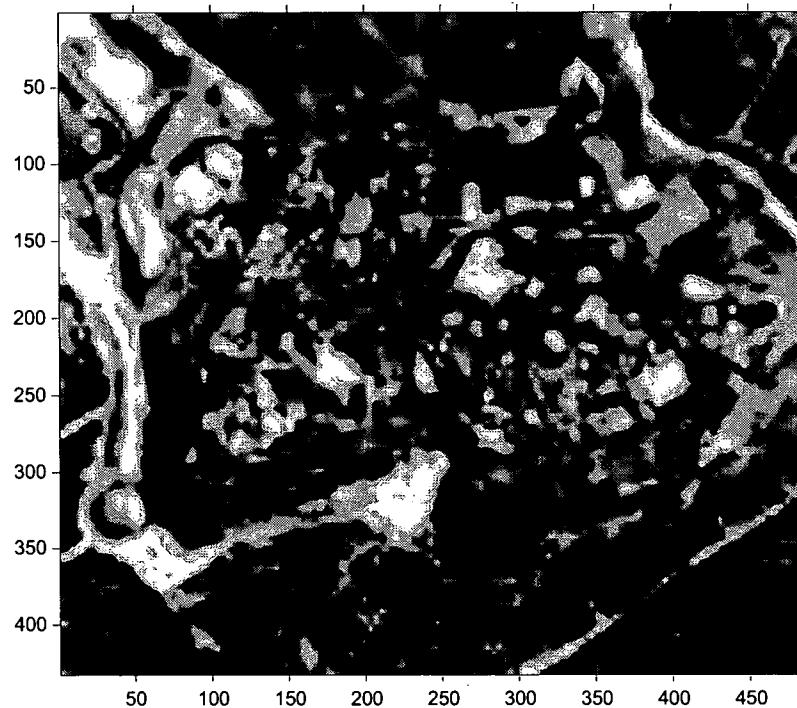


Figure 30. HR image output of local constant statistics NUC followed by bilinear interpolation when $P = 64$ frames.

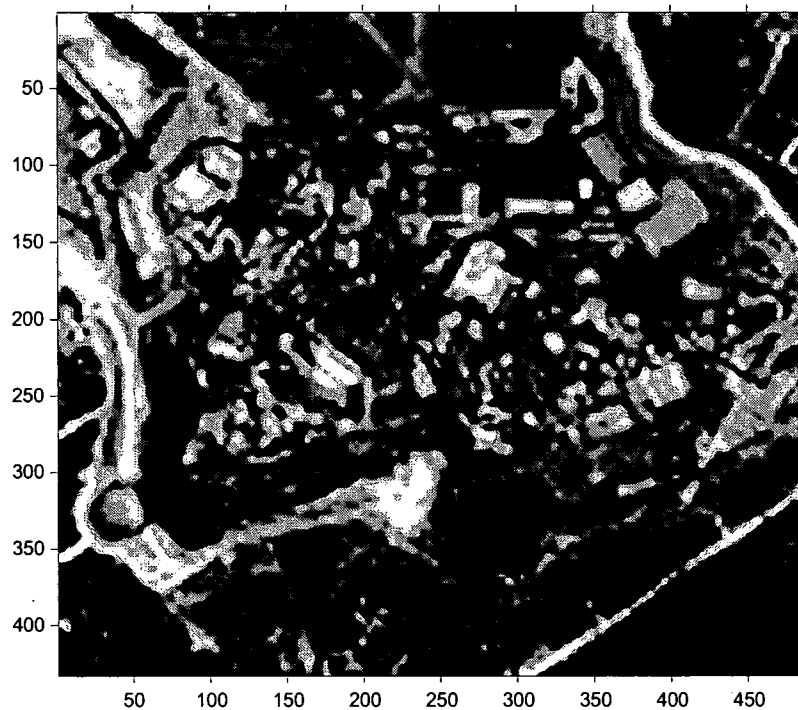


Figure 31. HR image output of MAP NUC followed by bilinear interpolation when $P = 64$ frames.

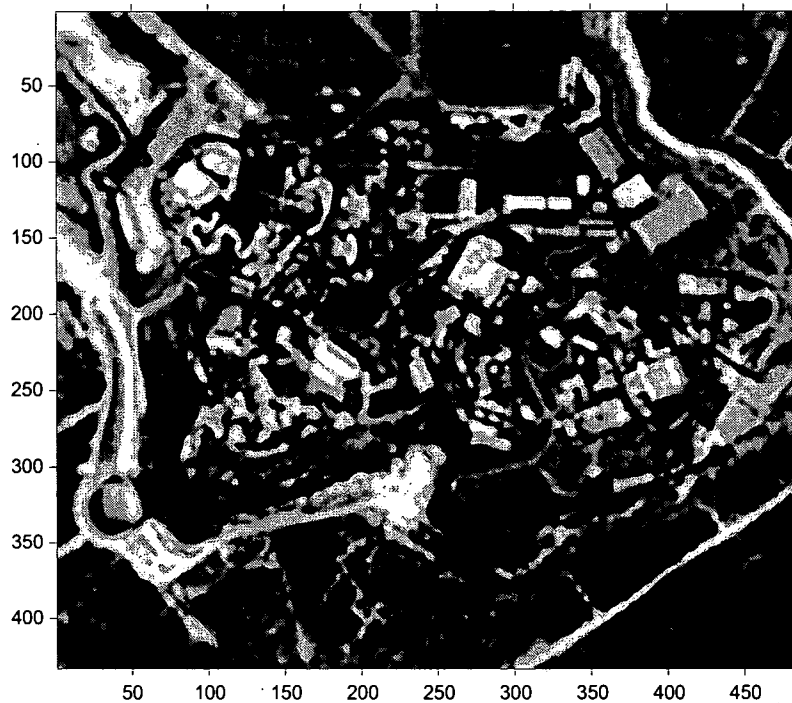


Figure 32. HR image output of MAP SR-NUC when $P = 64$ frames.

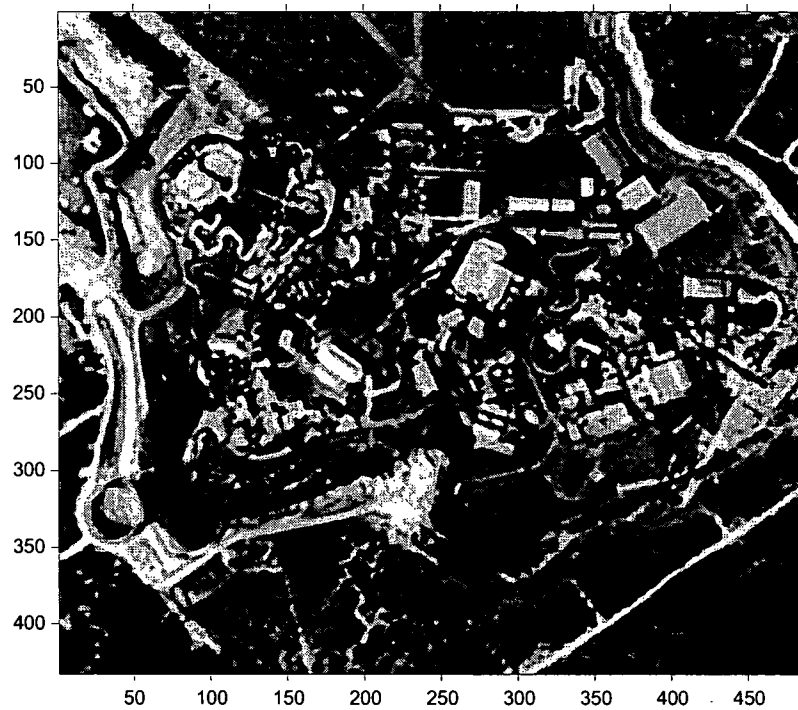


Figure 33. HR image output of MAP NUC followed by MAP SR when $P = 64$ frames.

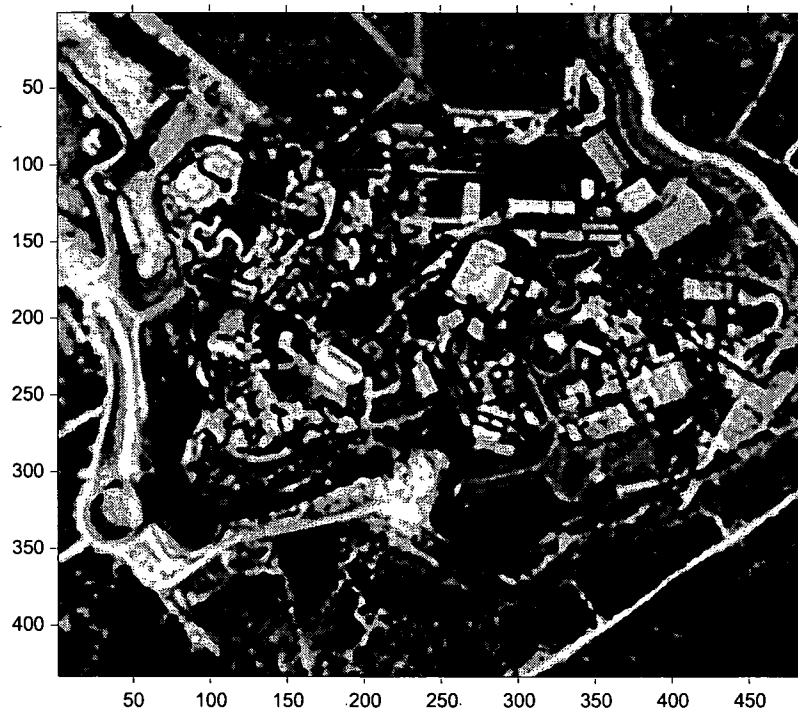


Figure 34. HR image output of Bias-Only MAP SR-NUC when $P = 64$ frames.



Figure 35. HR image output of Bias-Only MAP NUC followed by Bias-Only MAP SR when $P = 64$ frames.

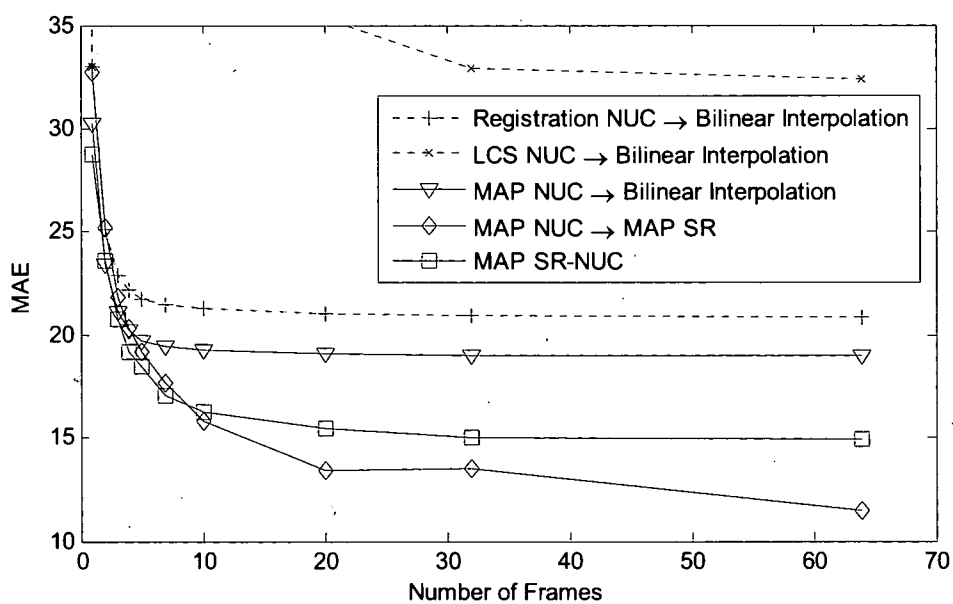


Figure 36. Mean absolute error of the HR image estimates of five combinations of NUC and HR image estimation approaches.

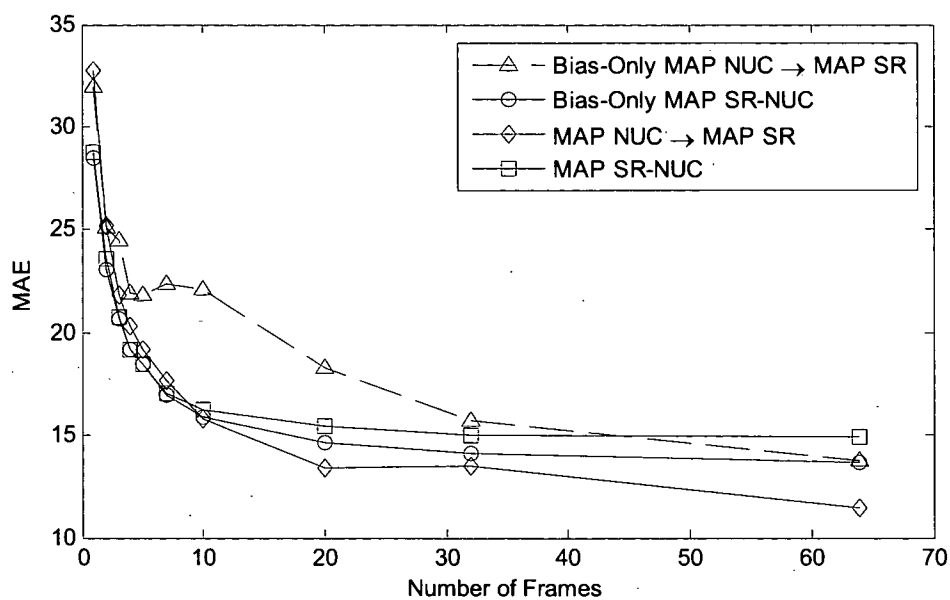


Figure 37. Mean absolute error of the HR image estimates of four MAP approaches that perform both NUC and HR image estimation.

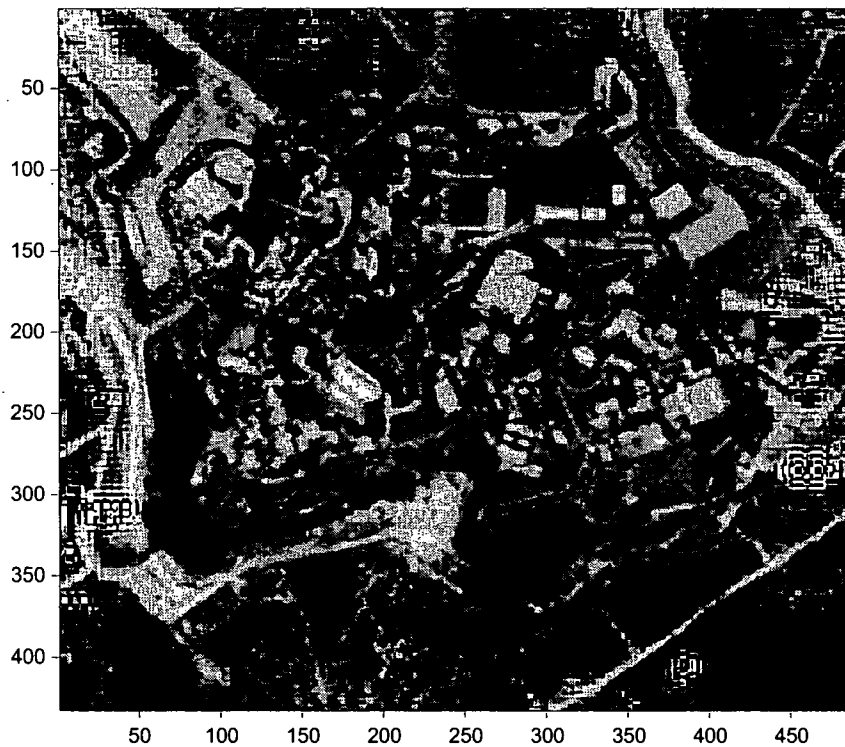


Figure 38. HR image output of MAP NUC followed by MAP SR when $P = 7$ frames.

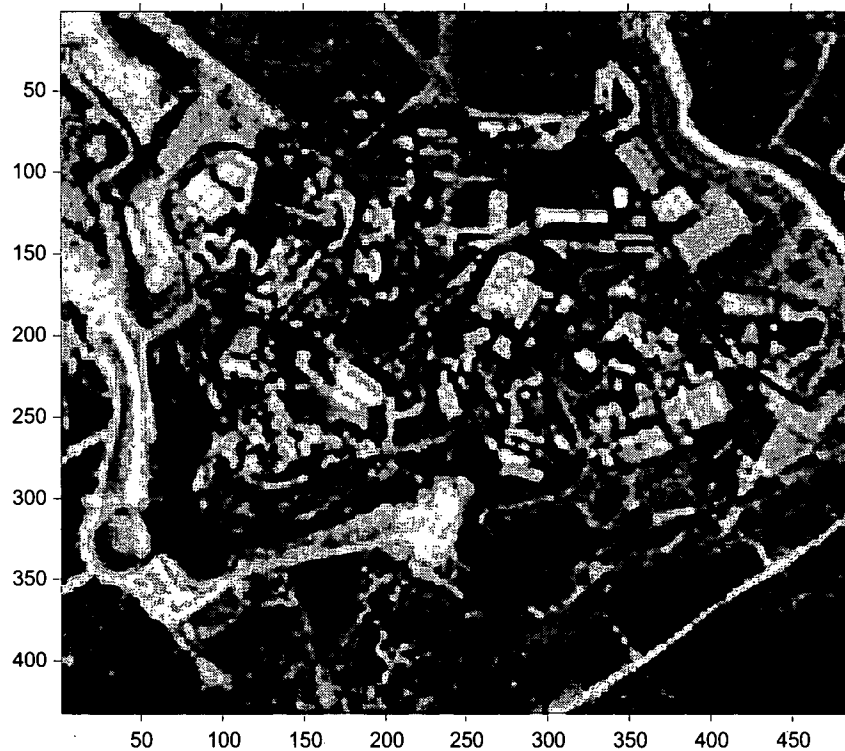


Figure 39. HR image output of MAP SR-NUC when $P = 7$ frames.

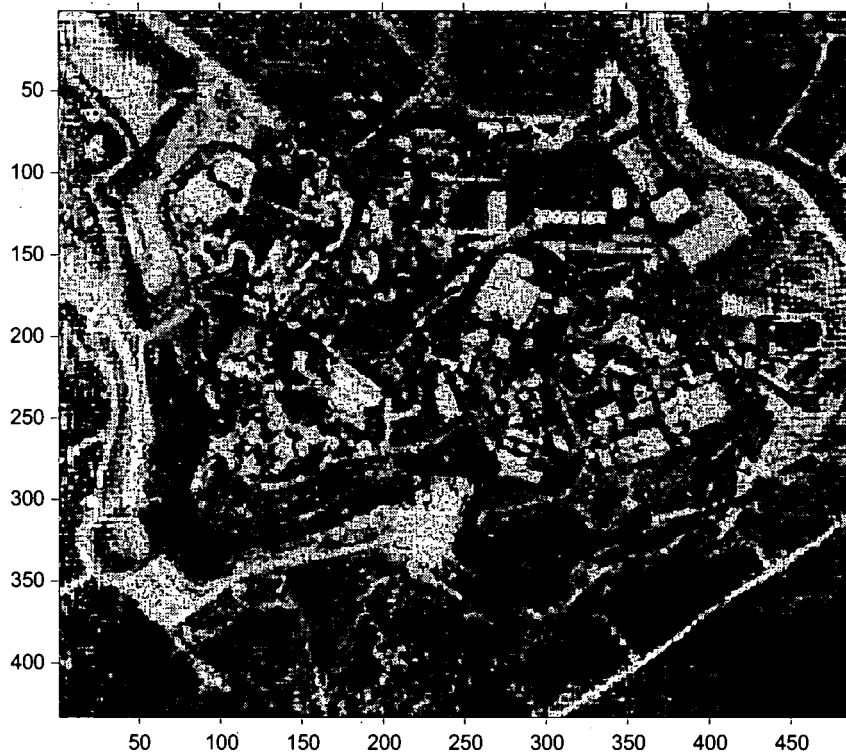


Figure 40. HR image output of Bias-Only MAP NUC followed by MAP SR when $P = 7$ frames.



Figure 41. HR image output of Bias-Only MAP SR-NUC when $P = 7$ frames.

B. Infrared Video

This section presents results obtained by applying the proposed algorithm to two real forward looking infrared (FLIR) video sequences. The sequences are captured using two imagers with different characteristics. One has a standard pixel size and undersamples the scene incident upon the FPA by $3.5\times$. The second has a much larger pixel pitch, resulting in the scene being undersampled by $8.33\times$. The mixture of a configuration that is fairly standard and a configuration that is very conducive to SR provides an excellent vehicle for evaluating the MAP SR-NUC algorithm.

1. First FPA Frame Sequence

The FLIR imager used to capture this sequence contains a 640×512 infrared FPA composed of Indium-Antimonide (InSb) detectors with a wavelength spectral response of $3\text{-}5\mu\text{m}$ and produces 14-bit data. The individual detectors are set on a $28\mu\text{m}$ pitch, yielding a 35.7 cycles/mm sampling frequency. The system is equipped with an $f/4$ lens, resulting in a 62.5 cycles/mm cutoff frequency. Thus the imager undersamples the scene by a factor of $3.5\times$.

The first full observed frame is shown in Figure 42(a), and a center 128×128 region of interest within this frame is shown in Figure 42(b). The data is processed with the SR-NUC algorithm using the variances derived in Chapter II. From Table 1, $\sigma_a^2 = 0.06^2$, $\sigma_b^2 = 480^2$, and $\sigma_n^2 = 10^2$. The approximate variance of the first observed frame is calculated and used to set $\sigma_z^2 = 300$. The motion parameters are estimated from the observed LR frames using the image registration technique detailed in [39, 40]. A low-pass pre-filter is used to reduce the effects of the nonuniformity on registration accuracy [42, 45].

The HR image output of the joint MAP SR-NUC algorithm for $L_x = L_y = 4$ and $P = 60$ frames is shown in Figure 43(a). The first LR frame corrected using the estimated gain and bias parameters followed by bilinear interpolation is shown in Figure 43(b). Note that the MAP SR-NUC image in Figure 43(a) provides more detail, including sufficient detail to read the word

“RANGER” on the side of the truck, than the image in Fig. 43(b) that is obtained using bilinear interpolation. Also note that the gain and bias corrected image in Figure 43(b) exhibits none of the nonuniformity that is evident in Figure 42.

Figures 44 and 45 display the results of other processing the frames sequences using other approaches. The Bias-Only MAP SR-NUC image output in Figure 44(a) is very similar to the MAP SR-NUC result. The result of the MAP NUC followed by MAP SR approach in Figure 44(b) shows even more crisp detail than the MAP SR-NUC result. In fact, Figure 46 shows that enough enhancement has been provided to make the lettering on the license plate barely readable. Finally, the benchmark algorithms are evaluated in Figure 45. The registration-based NUC is able to remove most of the nonuniformity from the image while the LCS NUC algorithm does not. Neither interpolated result exhibits the level of detail found in the SR-based results.

2. Second FPA Frame Sequence

The FLIR imager used to capture this sequence contains a 128×128 infrared FPA and produces 16-bit data. The FPA is composed of Indium-Antimonide (InSb) detectors with a wavelength spectral response of 3-5 μ m. The system is equipped with an $f/3$ 100mm diameter lens, yielding a cutoff frequency of 83.3 cycles/mm. The system has square detectors with a spacing of 50 μ m, yielding a sampling frequency of 20 cycles/mm. This results in the scene being undersampled by a factor of 8.33 \times .

The first observed frame is shown in Figure 47(a). The data is processed using the SR-NUC algorithm for $L_x = L_y = 4$ and $P = 50$. In the absence of archived data sets, the variance parameters are estimated to be $\sigma_a^2 = 1$, $\sigma_b^2 = 2000^2$, $\sigma_n^2 = 10^2$, and $\sigma_z^2 = 400^2$. It has been observed that the MAP algorithm is not highly sensitive to these parameters and their relative values are all that impact the result. Again, the motion parameters are estimated from the observed imagery using the registration technique in [39, 40] with a low-pass pre-filter used to reduce the effects of the nonuniformity on registration accuracy.

The output of the joint MAP SR-NUC algorithm shown in Figure 47(b) is a significant improvement over the observed, nonuniform frame in Figure 47(a). The Bias-Only MAP SR-NUC result in Figure 48(a) offers HR performance similar to the MAP SR-NUC result but some residual nonuniformity is present. The HR image output of the MAP NUC followed by MAP SR approach in Figure 48(b) shows slightly better detail than the others. Figure 49 shows that both benchmark algorithms exhibit noticeable low-frequency error caused mainly by regions in the scene that saturate the FPA. Saturated regions tend to affect all of the examined algorithms, and all algorithms would benefit from modifications that allow saturated data to be ignored in the estimation process.

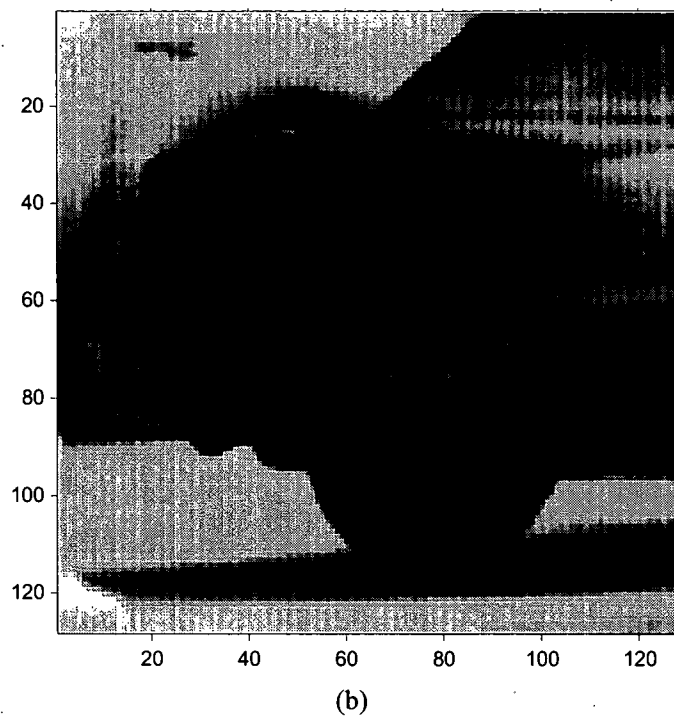
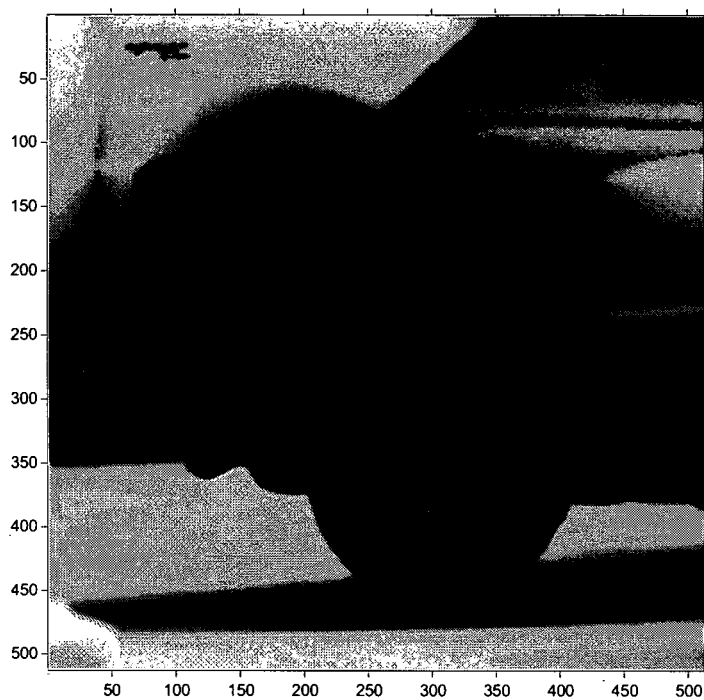
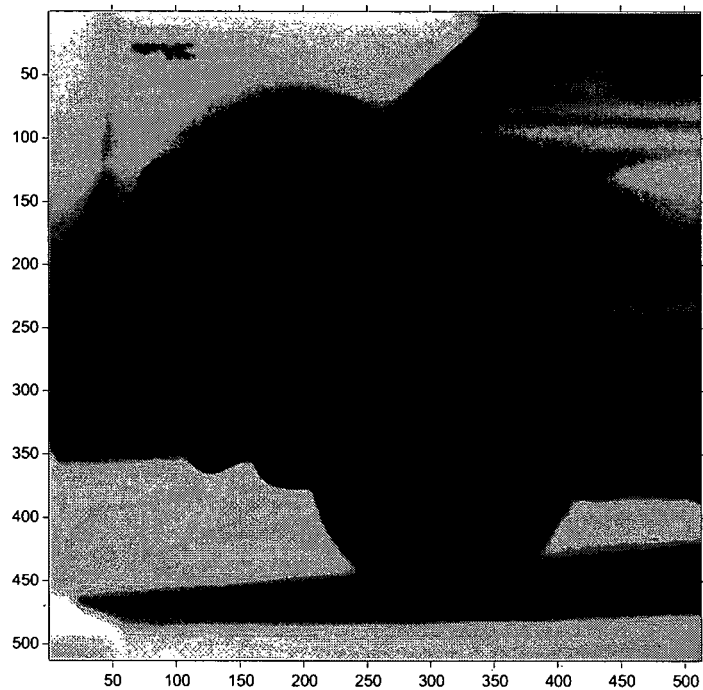


Figure 42. First uncorrected image sequence. (a) Observed frame one low-resolution image (b) observed frame one low-resolution image region of interest

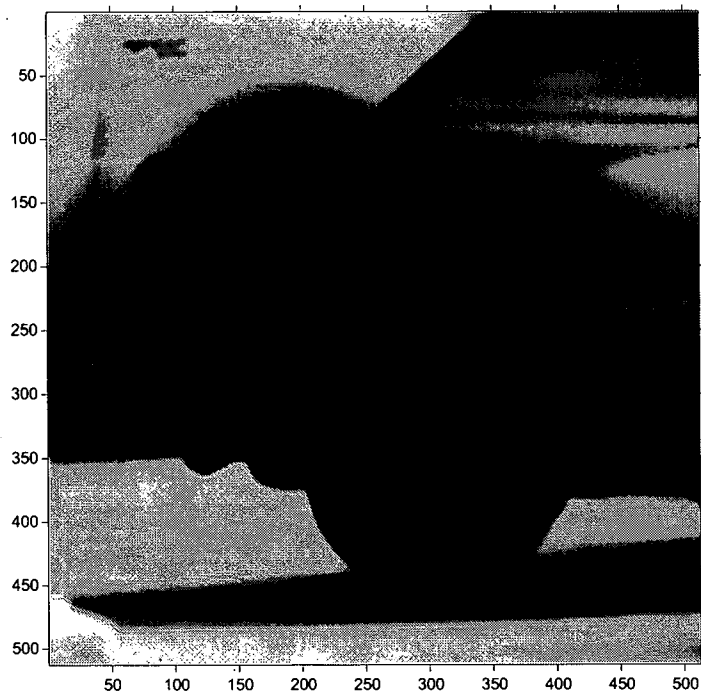


(a)

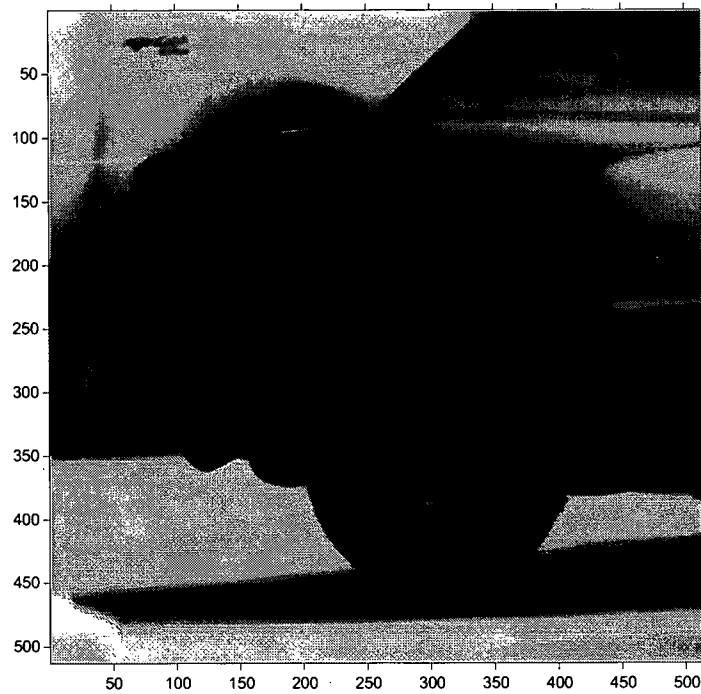


(b)

Figure 43. First image sequence frame one region of interest restored (a) using the MAP SR-NUC algorithm (b) low-resolution region of interest corrected then enlarged using bilinear interpolation

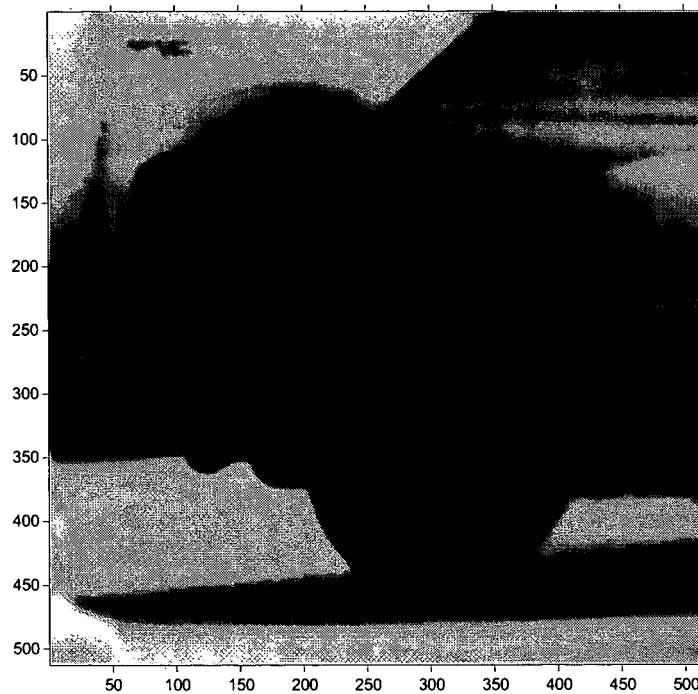


(a)

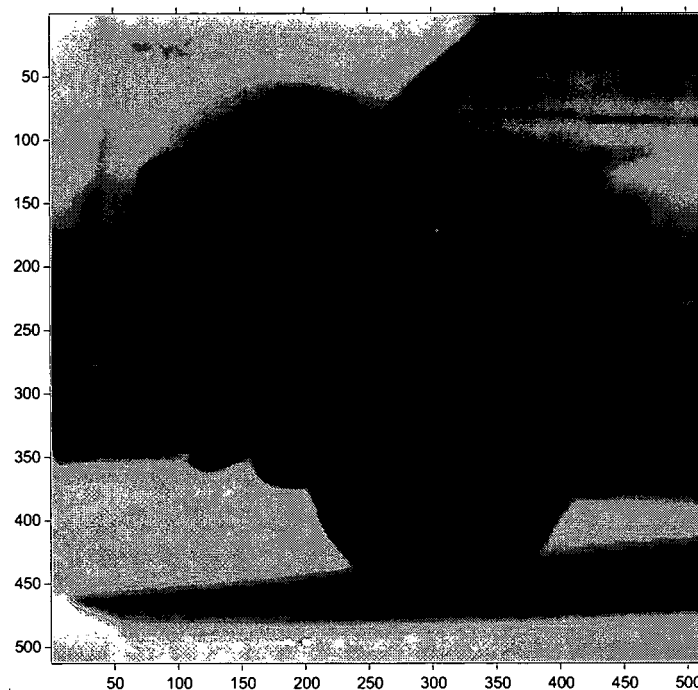


(b)

Figure 44. First image sequence frame one region of interest restored using alternate versions of the MAP SR-NUC algorithm. (a) Bias-Only MAP SR-NUC (b) MAP NUC followed by MAP SR

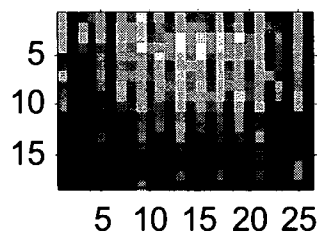


(a)

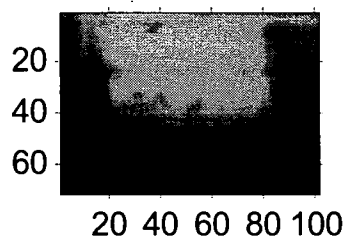


(b)

Figure 45. First image sequence frame one region of interest restored using benchmark NUC algorithms then enlarged using bilinear interpolation. (a) registration-based (b) local constant statistics



(a)



(b)

Figure 46. First image sequence frame one license plate region of interest (a) observed frame (b) restored using MAP NUC followed by MAP SR

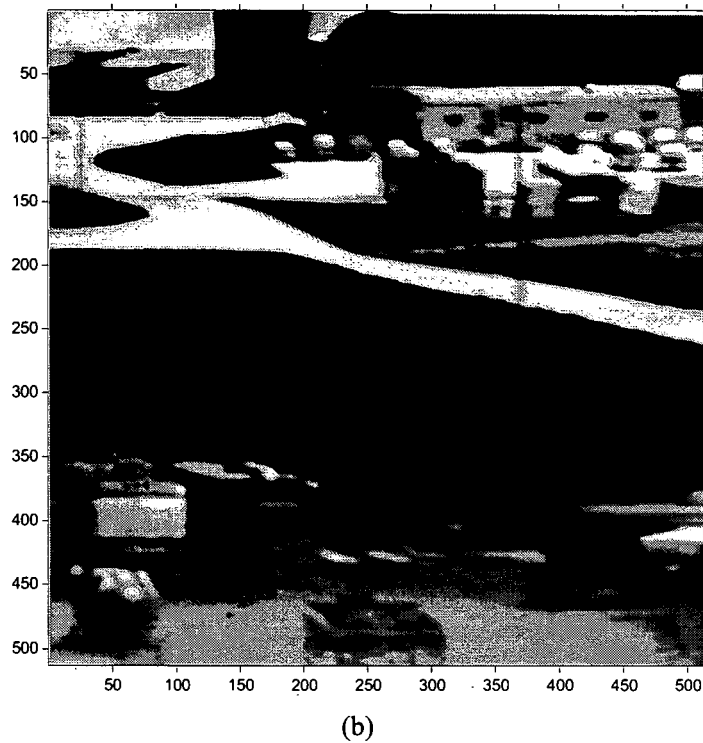
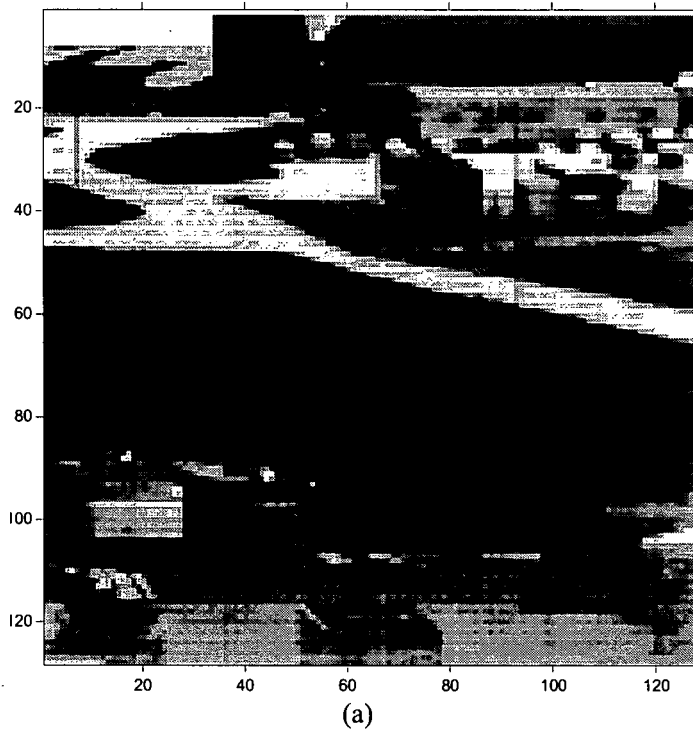
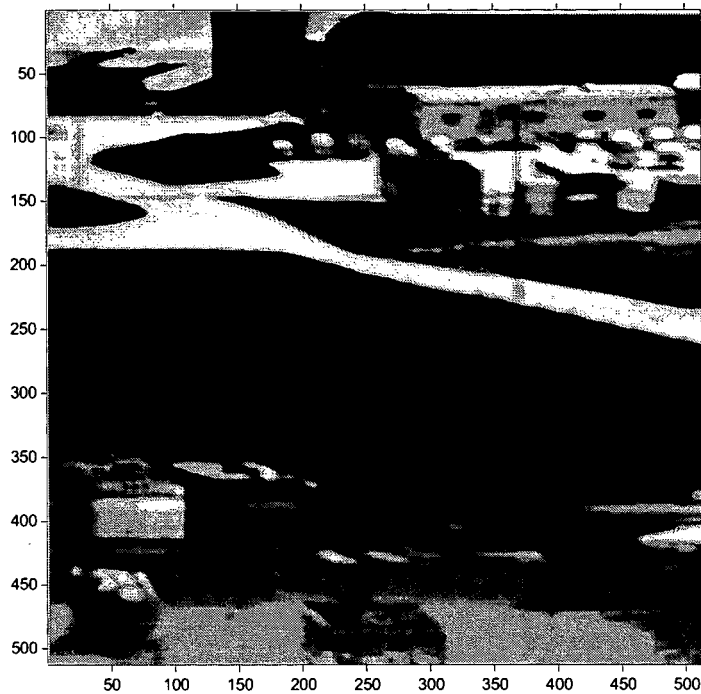
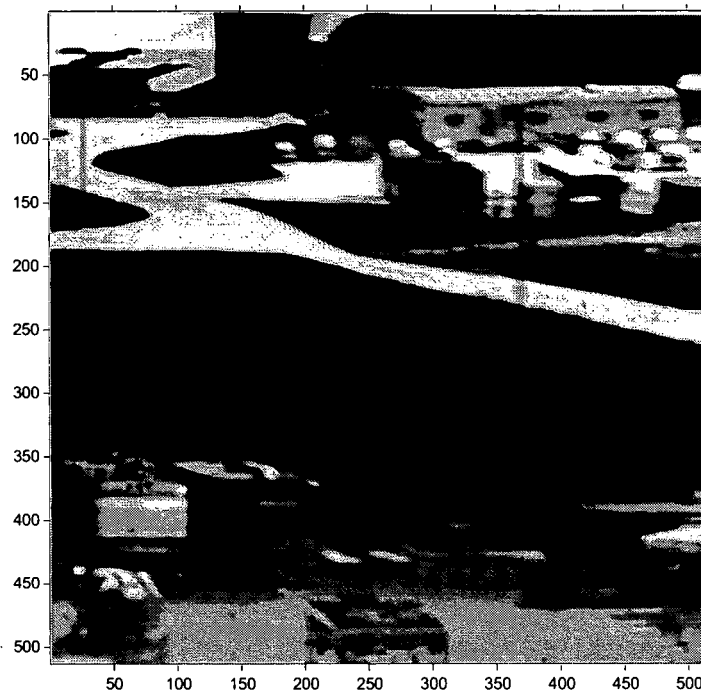


Figure 47. Second uncorrected image sequence (a) observed frame one low-resolution image (b) restored using the MAP SR-NUC algorithm

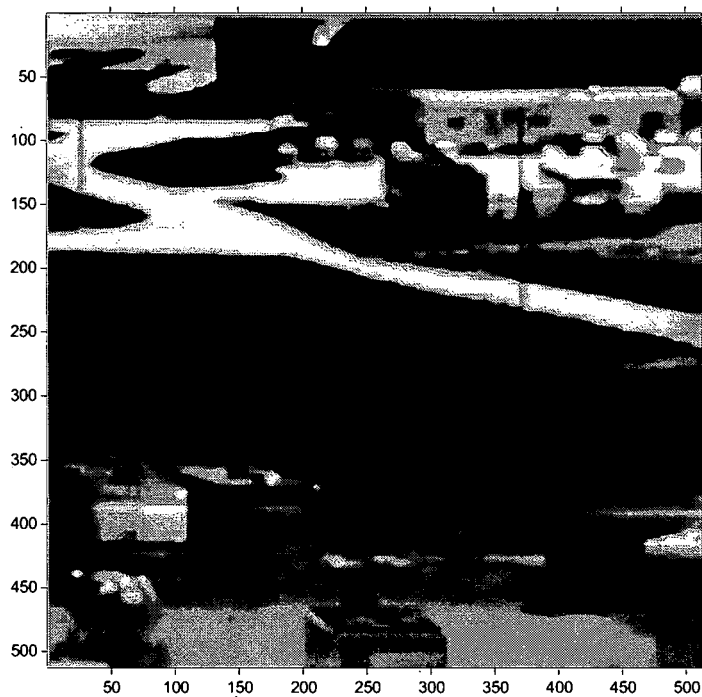


(a)

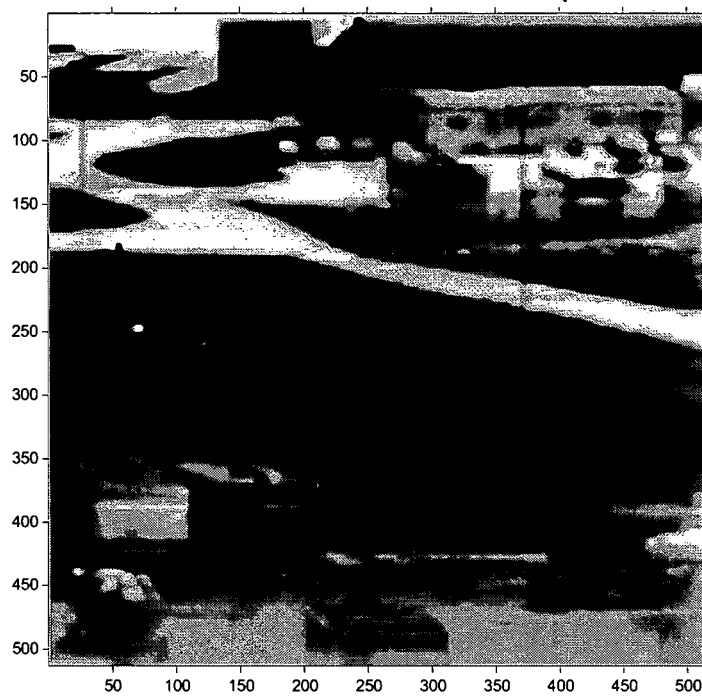


(b)

Figure 48. Second image sequence frame one restored using alternate versions of the MAP SR-NUC algorithm. (a) Bias-Only MAP SR-NUC (b) MAP NUC followed by MAP SR



(a)



(b)

Figure 49. Second image sequence frame one restored using benchmark NUC algorithms then enlarged using bilinear interpolation. (a) registration-based (b) local constant statistics

CHAPTER V

CONCLUSIONS

Three variations of the MAP SR-NUC algorithm have been developed. The full MAP SR-NUC algorithm jointly estimates the gain and bias nonuniformity parameters and an HR image from a sequence of nonuniform LR frames. This full version provides the best overall NUC and, when a limited number of frames are available, also provides the best HR image result. The MAP NUC algorithm estimates gain and bias nonuniformity parameters alone. This algorithm offers a NUC that is almost as good as the full version and, when combined with a subsequent SR, serves as a basis for the best overall SR results. The Bias-Only MAP SR-NUC algorithm estimates bias nonuniformity parameters and an HR image. This variation provides decent results with fewer computations.

The nonuniformity correction of the MAP SR-NUC algorithm is excellent and has better NUC performance than the other examined approaches, especially those that support only bias nonuniformity correction. The MAP SR-NUC algorithm is more accurate than the others near the average scene intensity level, and it also offers the best correction across the remainder of the dynamic range. This allows the nonuniformity parameters estimated by the MAP SR-NUC algorithm to be used to correct future frame sequences of different signal levels without the need for further nonuniformity parameter estimation. Both the characterization in Chapter II and the experimental results in Chapter IV indicate that the type of gain nonuniformity correction offered by the MAP SR-NUC and MAP NUC algorithms is necessary for a high level of NUC performance. Experimental results show that the ability of MAP SR-NUC to estimate nonuniformity jointly with SR provides a slightly more accurate correction than performing MAP

NUC alone. In situations where only a small number of frames are available, the advantages of MAP SR-NUC are even more apparent. This demonstrates that estimating nonuniformity parameters jointly with HR image parameters leads to a more accurate NUC, possibly because access to an HR image makes interpolation more accurate.

MAP SR-NUC also provides adequate SR enhancement. When a small number of frames is available, it provides a better HR image estimate than the other examined approaches. This is because the algorithm has better knowledge of the NUC parameters since they are estimated jointly with the HR image. This conclusion is supported by an examination of the Bias-Only version of the algorithm which also exhibits the advantages of using the joint estimation approach. For larger numbers of frames, the SR performance of the MAP SR-NUC algorithm is currently limited by the sheer number of gain, bias, and HR image parameters that be estimated.

MAP NUC has proven to be a powerful new form of scene-based NUC correction. The NUC performance is close to that of the joint MAP SR-NUC approach but requires less computation. Performing MAP NUC then applying a subsequent SR algorithm provides excellent HR image estimation when given a sufficient number of frames. Evidence shows that the gain nonuniformity parameters provided by the MAP NUC algorithm allow SR results to improve beyond the apparent performance limit experienced when gain nonuniformity is not corrected.

A bias-only version of the MAP SR-NUC algorithm is also presented. It is able to perform NUC accurately at the current scene point and provides decent HR image results. In situations where reduced computations or reduced resources are necessary, the Bias-Only MAP SR-NUC algorithm may provide an adequate solution.

Future improvements to the MAP SR-NUC algorithm will be directed at improved regularization approaches and optimization techniques that may improve convergence. It is believed that once the large number of parameters can be better estimated, the MAP SR-NUC

algorithm will provide SR performance equal to MAP NUC with subsequent SR applied but using a smaller number of frames. And if the convergence problem can be solved, then the MAP SR-NUC estimate of the gain nonuniformity parameters may be improved by including a second LR image sequence in the model. The second set of frames may offer a greater diversity of signal levels, which would increase gain estimation accuracy and allow improved NUC performance across the dynamic range.

In summary, the MAP SR-NUC algorithm offers novel advances in both the super-resolution and scene-based NUC signal processing areas. By combining scene-based NUC and SR, it is demonstrated that superior results are possible compared with the more conventional approach of performing scene-based NUC followed by independent SR. Additionally, when the MAP algorithm is applied without SR, the algorithm represents a novel and promising scene-based NUC technique that accurately corrects for both gain and bias nonuniformity. Future improvements offer the opportunity for even better performance.

APPENDIX A

OPTIMUM STEP SIZE DERIVATION

1. Gradient Descent Step Size

One approach to finding an optimal solution for the HR image \mathbf{z} , gains \mathbf{a} , and biases \mathbf{b} with respect to the cost function $L(\mathbf{z}, \mathbf{a}, \mathbf{b})$ is to apply a gradient descent procedure. This requires knowledge of the gradient of the cost function with respect to \mathbf{z} , the gradient of the cost function with respect to \mathbf{a} , and the gradient of the cost function with respect to \mathbf{b} .

In Chapter II, the cost function for simultaneous SR and NUC is found to be

$$L(\mathbf{z}, \mathbf{a}, \mathbf{b}) = \frac{1}{2\sigma_n^2} \sum_{k=1}^P (\mathbf{y}_k - \mathbf{A}\mathbf{W}_k\mathbf{z} - \mathbf{b})^T (\mathbf{y}_k - \mathbf{A}\mathbf{W}_k\mathbf{z} - \mathbf{b}) + \frac{1}{2} \mathbf{z}^T \mathbf{C}_z^{-1} \mathbf{z} + \frac{1}{2\sigma_a^2} (\mathbf{a} - \mathbf{1})^T (\mathbf{a} - \mathbf{1}) + \frac{1}{2\sigma_b^2} \mathbf{b}^T \mathbf{b}. \quad (60)$$

In Chapter II, the gradient of the function in (60) with respect to the vector \mathbf{z} is found to be

$$\nabla_{\mathbf{z}} L(\mathbf{z}, \mathbf{a}, \mathbf{b}) = \frac{1}{\sigma_n^2} \sum_{k=1}^P \mathbf{W}_k^T \mathbf{A}^T (\mathbf{y}_k - \mathbf{A}\mathbf{W}_k\mathbf{z} - \mathbf{b}) + \mathbf{C}_z^{-1} \mathbf{z}, \quad (61)$$

the gradient of the cost function with respect to the vector \mathbf{a} is found to be

$$\nabla_{\mathbf{a}} L(\mathbf{z}, \mathbf{a}, \mathbf{b}) = \frac{1}{\sigma_a^2} \sum_{k=1}^P \mathbf{z}^T \mathbf{W}_k^T (\mathbf{A}\mathbf{W}_k\mathbf{z} + \mathbf{b} - \mathbf{y}_k) + \frac{1}{\sigma_a^2} (\mathbf{a} - \mathbf{1}), \quad (62)$$

and the gradient of the cost function with respect to the vector \mathbf{b} is found to be

$$\nabla_{\mathbf{b}} L(\mathbf{z}, \mathbf{a}, \mathbf{b}) = \frac{1}{\sigma_n^2} \sum_{k=1}^P (\mathbf{A}\mathbf{W}_k\mathbf{z} + \mathbf{b} - \mathbf{y}_k) + \frac{1}{\sigma_b^2} \mathbf{b}. \quad (63)$$

The gradient descent procedure begins with an initial estimate of the HR image \mathbf{z} , gains \mathbf{a} , and biases \mathbf{b} . The initial estimate $\mathbf{z}(0)$ of the HR image is chosen to be a low-pass filtered and interpolated version of the first observed frame \mathbf{y}_1 . The initial gain estimate is chosen to be $\mathbf{a}(0) = \mathbf{1}$, where $\mathbf{1}$ is an $M \times 1$ vector of ones. The initial bias estimate is chosen to be $\mathbf{b}(0) = \mathbf{0}$, where $\mathbf{0}$

is an $M \times 1$ vector of zeros. The gradient descent update for an iteration $m = 0, 1, 2, \dots$ is computed using

$$\mathbf{z}(m+1) = \mathbf{z}(m) - \varepsilon(m) \mathbf{g}_z(m), \quad (64)$$

$$\mathbf{a}(m+1) = \mathbf{a}(m) - \varepsilon(m) \mathbf{g}_a(m), \quad (65)$$

and

$$\mathbf{b}(m+1) = \mathbf{b}(m) - \varepsilon(m) \mathbf{g}_b(m), \quad (66)$$

where

$$\mathbf{g}_z(m) = \nabla_z L(\mathbf{z}, \mathbf{a}, \mathbf{b}) \Big|_{\mathbf{z}=\mathbf{z}(m), \mathbf{a}=\mathbf{a}(m), \mathbf{b}=\mathbf{b}(m)}, \quad (67)$$

$$\mathbf{g}_a(m) = \nabla_a L(\mathbf{z}, \mathbf{a}, \mathbf{b}) \Big|_{\mathbf{z}=\mathbf{z}(m), \mathbf{a}=\mathbf{a}(m), \mathbf{b}=\mathbf{b}(m)} \quad (68)$$

and

$$\mathbf{g}_b(m) = \nabla_b L(\mathbf{z}, \mathbf{a}, \mathbf{b}) \Big|_{\mathbf{z}=\mathbf{z}(m), \mathbf{a}=\mathbf{a}(m), \mathbf{b}=\mathbf{b}(m)} \quad (69)$$

The step size $\varepsilon(m)$ for a given iteration m is optimized by minimizing

$$L(\mathbf{z}(m+1), \mathbf{a}(m+1), \mathbf{b}(m+1)) = L(\mathbf{z}(m) - \varepsilon(m) \mathbf{g}_z(m), \mathbf{a}(m) - \varepsilon(m) \mathbf{g}_a(m), \mathbf{b}(m) - \varepsilon(m) \mathbf{g}_b(m)) \quad (70)$$

with respect to $\varepsilon(m)$. Taking the derivative of (70) with respect to $\varepsilon(m)$ and defining \mathbf{G}_A to be the $M \times M$ diagonal matrix that contains the elements of \mathbf{g}_a on its main diagonal yields

$$\nabla_\varepsilon [L(\mathbf{z}(m+1), \mathbf{a}(m+1), \mathbf{b}(m+1))] = \nabla_\varepsilon \left[\begin{aligned} & \frac{1}{2\sigma_n^2} \sum_{k=1}^P \left[\left(\mathbf{y}_k - (\mathbf{A}(m) - \varepsilon(m) \mathbf{G}_A(m)) \mathbf{W}_k (\mathbf{z}(m) - \varepsilon(m) \mathbf{g}_z(m)) - (\mathbf{b}(m) - \varepsilon(m) \mathbf{g}_b(m)) \right)^T \right. \\ & \left. \cdot \left(\mathbf{y}_k - (\mathbf{A}(m) - \varepsilon(m) \mathbf{G}_A(m)) \mathbf{W}_k (\mathbf{z}(m) - \varepsilon(m) \mathbf{g}_z(m)) - (\mathbf{b}(m) - \varepsilon(m) \mathbf{g}_b(m)) \right) \right] \\ & + \frac{1}{2} (\mathbf{z}(m) - \varepsilon(m) \mathbf{g}_z(m))^T \mathbf{C}_z^{-1} (\mathbf{z}(m) - \varepsilon(m) \mathbf{g}_z(m)) \\ & + \frac{1}{2\sigma_a^2} ((\mathbf{a}(m) - \varepsilon(m) \mathbf{g}_a(m)) - \mathbf{1})^T ((\mathbf{a}(m) - \varepsilon(m) \mathbf{g}_a(m)) - \mathbf{1}) \\ & + \frac{1}{2\sigma_b^2} (\mathbf{b}(m) - \varepsilon(m) \mathbf{g}_b(m))^T (\mathbf{b}(m) - \varepsilon(m) \mathbf{g}_b(m)) \end{aligned} \right] \quad (71)$$

Given two generic $M \times 1$ matrices \mathbf{e} and \mathbf{f} ,

$$\nabla_a [\mathbf{e}^T \mathbf{A} \mathbf{f}] = \mathbf{e}^T \mathbf{f} \quad (72)$$

and

$$\nabla_{\mathbf{A}}[\mathbf{e}^T \mathbf{A}^T \mathbf{A} \mathbf{f}] = 2\mathbf{e}^T \mathbf{A} \mathbf{f} \quad (73)$$

apply since \mathbf{A} is a diagonal matrix. Using these results, the derivative in (71) is

$$\begin{aligned} \nabla_{\epsilon}[L(\mathbf{z}(m+1), \mathbf{a}(m+1), \mathbf{b}(m+1))] = & \frac{1}{2\sigma_n^2} \sum_{k=1}^P \left[2 \cdot \begin{pmatrix} \mathbf{y}_k - (\mathbf{A}(m) - \epsilon(m) \mathbf{G}_A(m)) \mathbf{W}_k (\mathbf{z}(m) - \epsilon(m) \mathbf{g}_z(m)) \\ -(\mathbf{b}(m) - \epsilon(m) \mathbf{g}_b(m)) \end{pmatrix}^T \right. \\ & \left. \cdot (-(-\mathbf{A}(m) \mathbf{W}_k \mathbf{g}_z(m) - \mathbf{G}_A(m) \mathbf{W}_k \mathbf{z}(m) + 2\mathbf{G}_A(m) \mathbf{W}_k \mathbf{g}_z(m) \epsilon(m)) + \mathbf{g}_b(m)) \right] \\ & + \frac{1}{2} \cdot 2 \cdot (\mathbf{z}(m) - \epsilon(m) \mathbf{g}_z(m))^T \mathbf{C}_z^{-1} (-\mathbf{g}_z(m)) \\ & + \frac{1}{2\sigma_a^2} \cdot 2 \cdot (\mathbf{a}(m) - \epsilon(m) \mathbf{g}_a(m) - \mathbf{1})^T (-\mathbf{g}_a(m)) \\ & + \frac{1}{2\sigma_b^2} \cdot 2 \cdot (\mathbf{b}(m) - \epsilon(m) \mathbf{g}_b(m))^T (-\mathbf{g}_b(m)) \end{aligned} \quad (74)$$

Equation (74) can be reduced to

$$\begin{aligned} \nabla_{\epsilon}[L(\mathbf{z}(m+1), \mathbf{a}(m+1), \mathbf{b}(m+1))] = & \frac{1}{\sigma_n^2} \sum_{k=1}^P \left[\begin{pmatrix} \mathbf{y}_k - \mathbf{A}(m) \mathbf{W}_k \mathbf{z}(m) + \mathbf{A}(m) \mathbf{W}_k \mathbf{g}_z(m) \cdot \epsilon(m) + \mathbf{G}_A(m) \mathbf{W}_k \mathbf{z}(m) \cdot \epsilon(m) \\ -\mathbf{G}_A(m) \mathbf{W}_k \mathbf{g}_z(m) \cdot \epsilon(m)^2 - \mathbf{b}(m) + \mathbf{g}_b(m) \cdot \epsilon(m) \end{pmatrix}^T \right. \\ & \left. \cdot (\mathbf{A}(m) \mathbf{W}_k \mathbf{g}_z(m) + \mathbf{G}_A(m) \mathbf{W}_k \mathbf{z}(m) - 2\mathbf{G}_A(m) \mathbf{W}_k \mathbf{g}_z(m) \cdot \epsilon(m) + \mathbf{g}_b(m)) \right] \\ & + (\mathbf{g}_z^T(m) \mathbf{C}_z^{-1} \mathbf{g}_z(m) \cdot \epsilon(m) - \mathbf{z}^T \mathbf{C}_z^{-1} \mathbf{g}_z(m)) \\ & + \frac{1}{\sigma_a^2} (\mathbf{g}_a^T(m) \mathbf{g}_a(m) \cdot \epsilon(m) - \mathbf{a}^T(m) \mathbf{g}_a(m) + \mathbf{1}^T \mathbf{g}_a(m)) \\ & + \frac{1}{\sigma_b^2} (\mathbf{g}_b^T(m) \mathbf{g}_b(m) \cdot \epsilon(m) - \mathbf{b}^T(m) \mathbf{g}_b(m)) \end{aligned} \quad (75)$$

Grouping like terms in (75) yields

$$\begin{aligned} \nabla_{\epsilon}[L(\mathbf{z}(m+1), \mathbf{a}(m+1), \mathbf{b}(m+1))] = & \frac{1}{\sigma_n^2} \sum_{k=1}^P \left[\begin{pmatrix} (-\mathbf{G}_A(m) \mathbf{W}_k \mathbf{g}_z(m)) \cdot \epsilon(m)^2 + (\mathbf{A}(m) \mathbf{W}_k \mathbf{g}_z(m) + \mathbf{G}_A(m) \mathbf{W}_k \mathbf{z}(m) + \mathbf{g}_b(m)) \cdot \epsilon(m) \\ + (\mathbf{y}_k - \mathbf{A}(m) \mathbf{W}_k \mathbf{z}(m) - \mathbf{b}(m)) \end{pmatrix}^T \right. \\ & \left. \cdot ((-2\mathbf{G}_A(m) \mathbf{W}_k \mathbf{g}_z(m)) \cdot \epsilon(m) + (\mathbf{A}(m) \mathbf{W}_k \mathbf{g}_z(m) + \mathbf{G}_A(m) \mathbf{W}_k \mathbf{z}(m) + \mathbf{g}_b(m))) \right] \\ & + ((\mathbf{g}_z^T(m) \mathbf{C}_z^{-1} \mathbf{g}_z(m)) \cdot \epsilon(m) + (-\mathbf{z}^T \mathbf{C}_z^{-1} \mathbf{g}_z(m))) \\ & + \frac{1}{\sigma_a^2} ((\mathbf{g}_a^T(m) \mathbf{g}_a(m)) \cdot \epsilon(m) + (-\mathbf{a}^T(m) \mathbf{g}_a(m) + \mathbf{1}^T \mathbf{g}_a(m))) \\ & + \frac{1}{\sigma_b^2} ((\mathbf{g}_b^T(m) \mathbf{g}_b(m)) \cdot \epsilon(m) + (-\mathbf{b}^T(m) \mathbf{g}_b(m))) \end{aligned} \quad (76)$$

Collecting terms according to power of $\epsilon(m)$ allows (76) to be rewritten as

$$\begin{aligned}
\nabla_{\epsilon} [L(z(m+1), a(m+1), b(m+1))] = & \left[2 \cdot \frac{1}{\sigma_n^2} \sum_{k=1}^P \left((G_A(m) W_k g_z(m))^T (G_A(m) W_k g_z(m)) \right) \right] \cdot \epsilon(m)^3 \\
& + \left[-\frac{1}{\sigma_n^2} \sum_{k=1}^P \left((G_A(m) W_k g_z(m))^T (A(m) W_k g_z(m) + G_A(m) W_k z(m) + g_b(m)) \right) \right. \\
& \quad \left. + (A(m) W_k g_z(m) + G_A(m) W_k z(m) + g_b(m))^T (2G_A(m) W_k g_z(m)) \right) \right] \cdot \epsilon(m)^2 \\
& + \left[\frac{1}{\sigma_n^2} \sum_{k=1}^P \left((A(m) W_k g_z(m) + G_A(m) W_k z(m) + g_b(m))^T \right. \right. \\
& \quad \left. (A(m) W_k g_z(m) + G_A(m) W_k z(m) + g_b(m)) \right. \\
& \quad \left. - 2((y_k - A(m) W_k z(m) - b(m))^T (G_A(m) W_k g_z(m))) \right. \\
& \quad \left. + g_z^T(m) C_z^{-1} g_z(m) + \frac{1}{\sigma_a^2} g_a^T(m) g_a(m) + \frac{1}{\sigma_b^2} g_b^T(m) g_b(m) \right) \right] \cdot \epsilon(m) \\
& + \left[\frac{1}{\sigma_n^2} \sum_{k=1}^P \left((y_k - A(m) W_k z(m) - b(m))^T (A(m) W_k g_z(m) + G_A(m) W_k z(m) + g_b(m)) \right) \right. \\
& \quad \left. - z^T(m) C_z^{-1} g_z(m) - \frac{1}{\sigma_a^2} (a(m) - 1)^T g_a(m) - \frac{1}{\sigma_b^2} b^T(m) g_b(m) \right]
\end{aligned} \tag{77}$$

Since the two quantities within the $\epsilon(m)^2$ term are constants, they can be combined:

$$\begin{aligned}
\nabla_{\epsilon} [L(z(m+1), a(m+1), b(m+1))] = & \left[2 \cdot \frac{1}{\sigma_n^2} \sum_{k=1}^P \left((G_A(m) W_k g_z(m))^T (G_A(m) W_k g_z(m)) \right) \right] \cdot \epsilon(m)^3 \\
& + \left[-3 \frac{1}{\sigma_n^2} \sum_{k=1}^P \left((G_A(m) W_k g_z(m))^T (A W_k g_z(m) + G_A(m) W_k z + g_b(m)) \right) \right] \cdot \epsilon(m)^2 \\
& + \left[\frac{1}{\sigma_n^2} \sum_{k=1}^P \left((A W_k g_z(m) + G_A(m) W_k z + g_b(m))^T \right. \right. \\
& \quad \left. (A W_k g_z(m) + G_A(m) W_k z + g_b(m)) \right. \\
& \quad \left. - 2((y_k - A W_k z - b))^T (G_A(m) W_k g_z(m)) \right. \\
& \quad \left. + g_z^T(m) C_z^{-1} g_z(m) + \frac{1}{\sigma_a^2} g_a^T(m) g_a(m) + \frac{1}{\sigma_b^2} g_b^T(m) g_b(m) \right) \right] \cdot \epsilon(m) \\
& + \left[\frac{1}{\sigma_n^2} \sum_{k=1}^P \left((y_k - A W_k z - b)^T (A W_k g_z(m) + G_A(m) W_k z + g_b(m)) \right) - z^T C_z^{-1} g_z(m) \right. \\
& \quad \left. - \frac{1}{\sigma_a^2} (a - 1)^T g_a(m) - \frac{1}{\sigma_b^2} b^T g_b(m) \right]
\end{aligned} \tag{78}$$

Defining terms in (78) as

$$\bar{g}(m) = G_A(m) W_k g_z(m), \tag{79}$$

$$\bar{z}(m) = A(m) W_k g_z(m) + G_A(m) W_k z(m) + g_b(m), \text{ and} \tag{80}$$

$$\bar{y}(m) = y_k - A(m) W_k z(m) - b(m) \tag{81}$$

and setting the derivative with respect to $\epsilon(m)$ in (78) to zero yields

$$\begin{aligned}
0 = & \left[2 \cdot \frac{1}{\sigma_n^2} \sum_{k=1}^P \left(\bar{\mathbf{g}}(m)^T \bar{\mathbf{g}}(m) \right) \right] \cdot \varepsilon(m)^3 + \left[-3 \cdot \frac{1}{\sigma_n^2} \sum_{k=1}^P \left(\bar{\mathbf{g}}(m)^T \bar{\mathbf{z}}(m) \right) \right] \cdot \varepsilon(m)^2 \\
& + \left[\frac{1}{\sigma_n^2} \sum_{k=1}^P \left(\bar{\mathbf{z}}(m)^T \bar{\mathbf{z}}(m) - 2 \cdot \bar{\mathbf{y}}(m)^T \bar{\mathbf{g}}(m) \right) + \mathbf{g}_z(m)^T C_z^{-1} \mathbf{g}_z(m) + \frac{1}{\sigma_a^2} \mathbf{g}_a(m)^T \mathbf{g}_a(m) + \frac{1}{\sigma_b^2} \mathbf{g}_b(m)^T \mathbf{g}_b(m) \right] \cdot \varepsilon(m) \\
& + \left[\frac{1}{\sigma_n^2} \sum_{k=1}^P \left(\bar{\mathbf{y}}(m)^T \bar{\mathbf{z}}(m) \right) - \mathbf{z}(m)^T C_z^{-1} \mathbf{g}_z(m) - \frac{1}{\sigma_a^2} (\mathbf{a}(m) - \mathbf{1})^T \mathbf{g}_a(m) - \frac{1}{\sigma_b^2} \mathbf{b}(m)^T \mathbf{g}_b(m) \right]
\end{aligned} \tag{82}$$

Equation (82) has three solutions, two of which are imaginary and one of which is real. The real solution is chosen as the step size, and the gradient descent update is performed using Equations (64), (65), and (66).

This process is continued until the cost changes by less than a predetermined percentage or until a maximum number of iterations is reached.

2. Conjugate-Gradient Step Size

An alternative approach to finding an optimal solution for the HR image \mathbf{z} , gains \mathbf{a} and biases \mathbf{b} with respect to the cost function $L(\mathbf{z}, \mathbf{a}, \mathbf{b})$ is to apply a conjugate-gradient procedure. The steps presented here to solve for the HR image \mathbf{z} , gains \mathbf{a} , and biases \mathbf{b} are an extension of the approach outlined in [39] which solves for only the HR image.

In Chapter II, the cost function for simultaneous SR and NUC is found to be

$$L(\mathbf{z}, \mathbf{a}, \mathbf{b}) = \frac{1}{2\sigma_n^2} \sum_{k=1}^P (\mathbf{y}_k - \mathbf{A}\mathbf{W}_k \mathbf{z} - \mathbf{b})^T (\mathbf{y}_k - \mathbf{A}\mathbf{W}_k \mathbf{z} - \mathbf{b}) + \frac{1}{2} \mathbf{z}^T C_z^{-1} \mathbf{z} + \frac{1}{2\sigma_a^2} (\mathbf{a} - \mathbf{1})^T (\mathbf{a} - \mathbf{1}) + \frac{1}{2\sigma_b^2} \mathbf{b}^T \mathbf{b}. \tag{83}$$

In Chapter II, the gradient of the function in (83) with respect to the vector \mathbf{z} is found to be

$$\nabla_{\mathbf{z}} L(\mathbf{z}, \mathbf{a}, \mathbf{b}) = \frac{1}{\sigma_n^2} \sum_{k=1}^P \mathbf{W}_k^T \mathbf{A}^T (\mathbf{y} - \mathbf{A}\mathbf{W}_k \mathbf{z} - \mathbf{b}) + C_z^{-1} \mathbf{z}, \tag{84}$$

the gradient of the cost function with respect to the vector \mathbf{a} is found to be

$$\nabla_{\mathbf{a}} L(\mathbf{z}, \mathbf{a}, \mathbf{b}) = \frac{1}{\sigma_a^2} \sum_{k=1}^P \mathbf{z}^T \mathbf{W}_k^T (\mathbf{A}\mathbf{W}_k \mathbf{z} + \mathbf{b} - \mathbf{y}_k) + \frac{1}{\sigma_a^2} (\mathbf{a} - \mathbf{1}), \tag{85}$$

and the gradient of the cost function with respect to the vector \mathbf{b} is found to be

$$\nabla_{\mathbf{b}} L(\mathbf{z}, \mathbf{a}, \mathbf{b}) = \frac{1}{\sigma_n^2} \sum_{k=1}^P (\mathbf{A} \mathbf{W}_k \mathbf{z} + \mathbf{b} - \mathbf{y}_k) + \frac{1}{\sigma_b^2} \mathbf{b}. \quad (86)$$

The conjugate-gradient procedure begins with an initial estimate of the HR image \mathbf{z} , gains \mathbf{a} , and biases \mathbf{b} . The initial estimate $\mathbf{z}(0)$ of the HR image is chosen to be a low-pass filtered and interpolated version of the first observed frame \mathbf{y}_1 . The initial gain estimate is chosen to be $\mathbf{a}(0) = \mathbf{1}$, where $\mathbf{1}$ is an $M \times 1$ vector of ones. The initial bias estimate is chosen to be $\mathbf{b}(0) = \mathbf{0}$, where $\mathbf{0}$ is an $M \times 1$ vector of zeros. The conjugate-gradient update for an iteration $m = 0, 1, 2, \dots$ is computed using

$$\mathbf{z}(m+1) = \mathbf{z}(m) - \varepsilon(m) \mathbf{d}_z(m), \quad (87)$$

$$\mathbf{a}(m+1) = \mathbf{a}(m) - \varepsilon(m) \mathbf{d}_a(m), \quad (88)$$

and

$$\mathbf{b}(m+1) = \mathbf{b}(m) - \varepsilon(m) \mathbf{d}_b(m). \quad (89)$$

Here ε is the step size and \mathbf{d}_z , \mathbf{d}_a and \mathbf{d}_b are the conjugate-gradient vectors of size $N \times 1$, $M \times 1$ and $M \times 1$ respectively. At the initial update for iteration $m = 0$, the gradient descent vectors in (26), (27), and (28) are used to define the conjugate-gradient vectors to be

$$\mathbf{d}_z(0) = -\mathbf{g}_z(0), \quad (90)$$

$$\mathbf{d}_a(0) = -\mathbf{g}_a(0) \quad (91)$$

and

$$\mathbf{d}_b(0) = -\mathbf{g}_b(0). \quad (92)$$

For updates of subsequent iterations $m = 1, 2, \dots$ the conjugate-gradient vectors are defined to be

$$\mathbf{d}_z(m+1) = -\mathbf{g}_z(m+1) + \frac{\mathbf{g}_z^T(m+1) \mathbf{g}_z(m+1)}{\mathbf{g}_z^T(m) \mathbf{g}_z(m)} \mathbf{d}_z(m), \quad (93)$$

$$\mathbf{d}_a(m+1) = -\mathbf{g}_a(m+1) + \frac{\mathbf{g}_a^T(m+1) \mathbf{g}_a(m+1)}{\mathbf{g}_a^T(m) \mathbf{g}_a(m)} \mathbf{d}_a(m), \quad (94)$$

and

$$\mathbf{d}_b(m+1) = -\mathbf{g}_b(m+1) + \frac{\mathbf{g}_b^T(m+1)\mathbf{g}_b(m+1)}{\mathbf{g}_b^T(m)\mathbf{g}_b(m)}\mathbf{d}_b(m). \quad (95)$$

The step size $\varepsilon(m)$ for a given iteration m is optimized by minimizing

$$L(\mathbf{z}(m+1), \mathbf{a}(m+1), \mathbf{b}(m+1)) = L(\mathbf{z}(m) - \varepsilon(m)\mathbf{d}_z(m), \mathbf{a}(m) - \varepsilon(m)\mathbf{d}_a(m), \mathbf{b}(m) - \varepsilon(m)\mathbf{d}_b(m)). \quad (96)$$

with respect to $\varepsilon(m)$. Taking the derivative of (96) with respect to $\varepsilon(m)$ and defining \mathbf{D}_A to be the $M \times M$ diagonal matrix that contains the elements of \mathbf{d}_a on its main diagonal yields

$$\nabla_\varepsilon [L(\mathbf{z}(m+1), \mathbf{a}(m+1), \mathbf{b}(m+1))] = \nabla_\varepsilon \left[\begin{aligned} & \frac{1}{2\sigma_n^2} \sum_{k=1}^p \left[\left(\mathbf{y}_k - (\mathbf{A}(m) - \varepsilon(m)\mathbf{D}_A(m))\mathbf{W}_k(\mathbf{z}(m) - \varepsilon(m)\mathbf{d}_z(m)) - (\mathbf{b}(m) - \varepsilon(m)\mathbf{d}_b(m)) \right)^T \right. \\ & \left. \cdot \left(\mathbf{y}_k - (\mathbf{A}(m) - \varepsilon(m)\mathbf{D}_A(m))\mathbf{W}_k(\mathbf{z}(m) - \varepsilon(m)\mathbf{d}_z(m)) - (\mathbf{b}(m) - \varepsilon(m)\mathbf{d}_b(m)) \right) \right] \\ & + \frac{1}{2} (\mathbf{z}(m) - \varepsilon(m)\mathbf{d}_z(m))^T \mathbf{C}_z^{-1} (\mathbf{z}(m) - \varepsilon(m)\mathbf{d}_z(m)) \\ & + \frac{1}{2\sigma_a^2} ((\mathbf{a}(m) - \varepsilon(m)\mathbf{d}_a(m)) - \mathbf{1})^T ((\mathbf{a}(m) - \varepsilon(m)\mathbf{d}_a(m)) - \mathbf{1}) \\ & + \frac{1}{2\sigma_b^2} (\mathbf{b}(m) - \varepsilon(m)\mathbf{d}_b(m))^T (\mathbf{b}(m) - \varepsilon(m)\mathbf{d}_b(m)) \end{aligned} \right] \quad (97)$$

Using the results in (72) and (73), the derivative in (97) is

$$\begin{aligned} \nabla_\varepsilon [L(\mathbf{z}(m+1), \mathbf{a}(m+1), \mathbf{b}(m+1))] = & \frac{1}{2\sigma_n^2} \sum_{k=1}^p \left[2 \cdot \begin{pmatrix} \mathbf{y}_k - (\mathbf{A}(m) - \varepsilon(m)\mathbf{D}_A(m))\mathbf{W}_k(\mathbf{z}(m) - \varepsilon(m)\mathbf{d}_z(m)) \\ -(\mathbf{b}(m) - \varepsilon(m)\mathbf{d}_b(m)) \end{pmatrix}^T \right. \\ & \left. \cdot \begin{pmatrix} -(\mathbf{A}(m)\mathbf{W}_k\mathbf{d}_z(m) - \mathbf{D}_A(m)\mathbf{W}_k\mathbf{z}(m) + 2\mathbf{D}_A(m)\mathbf{W}_k\mathbf{d}_z(m)\varepsilon(m) + \mathbf{d}_b(m)) \\ -(-\mathbf{A}(m)\mathbf{W}_k\mathbf{d}_z(m) - \mathbf{D}_A(m)\mathbf{W}_k\mathbf{z}(m) + 2\mathbf{D}_A(m)\mathbf{W}_k\mathbf{d}_z(m)\varepsilon(m) + \mathbf{d}_b(m)) \end{pmatrix} \right] \\ & + \frac{1}{2} \cdot 2 \cdot (\mathbf{z}(m) - \varepsilon(m)\mathbf{d}_z(m))^T \mathbf{C}_z^{-1} (-\mathbf{d}_z(m)) \\ & + \frac{1}{2\sigma_a^2} \cdot 2 \cdot (\mathbf{a}(m) - \varepsilon(m)\mathbf{d}_a(m) - \mathbf{1})^T (-\mathbf{d}_a(m)) \\ & + \frac{1}{2\sigma_b^2} \cdot 2 \cdot (\mathbf{b}(m) - \varepsilon(m)\mathbf{d}_b(m))^T (-\mathbf{d}_b(m)) \end{aligned} \quad (98)$$

Equation (98) can be reduced to

$$\begin{aligned} \nabla_\varepsilon [L(\mathbf{z}(m+1), \mathbf{a}(m+1), \mathbf{b}(m+1))] = & \frac{1}{\sigma_n^2} \sum_{k=1}^p \left[\begin{pmatrix} \mathbf{y}_k - \mathbf{A}(m)\mathbf{W}_k\mathbf{z}(m) + \mathbf{A}(m)\mathbf{W}_k\mathbf{d}_z(m) \cdot \varepsilon(m) + \mathbf{D}_A(m)\mathbf{W}_k\mathbf{z}(m) \cdot \varepsilon(m) \\ -\mathbf{D}_A(m)\mathbf{W}_k\mathbf{d}_z(m) \cdot \varepsilon(m)^2 - \mathbf{b}(m) + \mathbf{d}_b(m) \cdot \varepsilon(m) \end{pmatrix}^T \right. \\ & \left. \cdot \begin{pmatrix} \mathbf{A}(m)\mathbf{W}_k\mathbf{d}_z(m) + \mathbf{D}_A(m)\mathbf{W}_k\mathbf{z}(m) - 2\mathbf{D}_A(m)\mathbf{W}_k\mathbf{d}_z(m) \cdot \varepsilon(m) + \mathbf{d}_b(m) \\ (\mathbf{A}(m)\mathbf{W}_k\mathbf{d}_z(m) + \mathbf{D}_A(m)\mathbf{W}_k\mathbf{z}(m) - 2\mathbf{D}_A(m)\mathbf{W}_k\mathbf{d}_z(m) \cdot \varepsilon(m) + \mathbf{d}_b(m)) \end{pmatrix} \right] \\ & + (\mathbf{d}_z^T(m)\mathbf{C}_z^{-1}\mathbf{d}_z(m) \cdot \varepsilon(m) - \mathbf{z}^T\mathbf{C}_z^{-1}\mathbf{d}_z(m)) \\ & + \frac{1}{\sigma_a^2} (\mathbf{d}_a^T(m)\mathbf{d}_a(m) \cdot \varepsilon(m) - \mathbf{a}^T(m)\mathbf{d}_a(m) + \mathbf{1}^T\mathbf{d}_a(m)) \\ & + \frac{1}{\sigma_b^2} (\mathbf{d}_b^T(m)\mathbf{d}_b(m) \cdot \varepsilon(m) - \mathbf{b}^T(m)\mathbf{d}_b(m)) \end{aligned} \quad (99)$$

Grouping like terms in (99) yields

$$\begin{aligned} \nabla_{\varepsilon} [L(z(m+1), a(m+1), b(m+1))] = & \frac{1}{\sigma_n^2} \sum_{k=1}^P \left[\left((-D_A(m) W_k d_z(m)) \cdot \varepsilon(m)^2 + (A(m) W_k d_z(m) + D_A(m) W_k z(m) + d_b(m)) \cdot \varepsilon(m) \right)^T \right. \\ & \left. + (y_k - A(m) W_k z(m) - b(m)) \right. \\ & \left. \cdot ((-2D_A(m) W_k d_z(m)) \cdot \varepsilon(m) + (A(m) W_k d_z(m) + D_A(m) W_k z(m) + d_b(m))) \right. \\ & \left. + ((d_z^T(m) C_z^{-1} d_z(m)) \cdot \varepsilon(m) + (-z^T(m) C_z^{-1} d_z(m))) \right. \\ & \left. + \frac{1}{\sigma_a^2} ((d_a^T(m) d_a(m)) \cdot \varepsilon(m) + (-a^T(m) d_a(m) + 1^T d_a(m))) \right. \\ & \left. + \frac{1}{\sigma_b^2} ((d_b^T(m) d_b(m)) \cdot \varepsilon(m) + (-b^T(m) d_b(m))) \right] \end{aligned} \quad (100)$$

Collecting terms according to power of $\varepsilon(m)$ allows (100) to be rewritten as

$$\begin{aligned} \nabla_{\varepsilon} [L(z(m+1), a(m+1), b(m+1))] = & \left[2 \cdot \frac{1}{\sigma_n^2} \sum_{k=1}^P ((D_A(m) W_k d_z(m))^T (D_A(m) W_k d_z(m))) \right] \cdot \varepsilon(m)^3 \\ & + \left[-\frac{1}{\sigma_n^2} \sum_{k=1}^P \left((D_A(m) W_k d_z(m))^T (A(m) W_k d_z(m) + D_A(m) W_k z(m) + d_b(m)) \right. \right. \\ & \left. \left. + (A(m) W_k d_z(m) + D_A(m) W_k z(m) + d_b(m))^T (2D_A(m) W_k d_z(m)) \right) \right] \cdot \varepsilon(m)^2 \\ & + \left[\frac{1}{\sigma_n^2} \sum_{k=1}^P \left((A(m) W_k d_z(m) + D_A(m) W_k z(m) + d_b(m))^T \right. \right. \\ & \left. \left(A(m) W_k d_z(m) + D_A(m) W_k z(m) + d_b(m) \right) \right. \\ & \left. - 2((y_k - A(m) W_k z(m) - b(m)))^T (D_A(m) W_k d_z(m)) \right. \\ & \left. + d_z^T(m) C_z^{-1} d_z(m) + \frac{1}{\sigma_a^2} d_a^T(m) d_a(m) + \frac{1}{\sigma_b^2} d_b^T(m) d_b(m) \right) \right] \cdot \varepsilon(m) \\ & + \left[\frac{1}{\sigma_n^2} \sum_{k=1}^P ((y_k - A(m) W_k z(m) - b(m))^T (A(m) W_k d_z(m) + D_A(m) W_k z(m) + d_b(m))) \right. \\ & \left. - z^T(m) C_z^{-1} d_z(m) - \frac{1}{\sigma_a^2} (a(m) - 1)^T d_a(m) - \frac{1}{\sigma_b^2} b(m)^T d_b(m) \right] \end{aligned} \quad (101)$$

Since the two quantities within the $\varepsilon(m)^2$ term are constants, they can be combined:

$$\begin{aligned}
\nabla_{\epsilon} [L(\mathbf{z}(m+1), \mathbf{a}(m+1), \mathbf{b}(m+1))] = & \left[2 \cdot \frac{1}{\sigma_n^2} \sum_{k=1}^P \left((\mathbf{D}_A(m) \mathbf{W}_k \mathbf{d}_z(m))^T (\mathbf{D}_A(m) \mathbf{W}_k \mathbf{d}_z(m)) \right) \right] \cdot \epsilon(m)^3 \\
& + \left[-3 \cdot \frac{1}{\sigma_n^2} \sum_{k=1}^P \left((\mathbf{D}_A(m) \mathbf{W}_k \mathbf{d}_z(m))^T (\mathbf{A} \mathbf{W}_k \mathbf{d}_z(m) + \mathbf{D}_A(m) \mathbf{W}_k \mathbf{z} + \mathbf{d}_b(m)) \right) \right] \cdot \epsilon(m)^2 \\
& + \left[\frac{1}{\sigma_n^2} \sum_{k=1}^P \left(\begin{aligned} & (\mathbf{A} \mathbf{W}_k \mathbf{d}_z(m) + \mathbf{D}_A(m) \mathbf{W}_k \mathbf{z} + \mathbf{d}_b(m))^T \\ & (\mathbf{A} \mathbf{W}_k \mathbf{d}_z(m) + \mathbf{D}_A(m) \mathbf{W}_k \mathbf{z} + \mathbf{d}_b(m)) \\ & - 2((\mathbf{y}_k - \mathbf{A} \mathbf{W}_k \mathbf{z} - \mathbf{b}))^T (\mathbf{D}_A(m) \mathbf{W}_k \mathbf{d}_z(m)) \\ & + \mathbf{d}_z(m)^T \mathbf{C}_z^{-1} \mathbf{d}_z(m) + \frac{1}{\sigma_a^2} \mathbf{d}_a(m)^T \mathbf{d}_a(m) + \frac{1}{\sigma_b^2} \mathbf{d}_b(m)^T \mathbf{d}_b(m) \end{aligned} \right) \right] \cdot \epsilon(m) \\
& + \left[\frac{1}{\sigma_n^2} \sum_{k=1}^P \left((\mathbf{y}_k - \mathbf{A} \mathbf{W}_k \mathbf{z} - \mathbf{b})^T (\mathbf{A} \mathbf{W}_k \mathbf{d}_z(m) + \mathbf{D}_A(m) \mathbf{W}_k \mathbf{z} + \mathbf{d}_b(m)) \right) - \mathbf{z}^T \mathbf{C}_z^{-1} \mathbf{d}_z(m) \right. \\
& \left. - \frac{1}{\sigma_a^2} (\mathbf{a} - \mathbf{1})^T \mathbf{d}_a(m) - \frac{1}{\sigma_b^2} \mathbf{b}^T \mathbf{d}_b(m) \right] \cdot \epsilon(m)
\end{aligned} \tag{102}$$

Defining terms in (102) as

$$\bar{\mathbf{d}}(m) = \mathbf{D}_A(m) \mathbf{W}_k \mathbf{d}_z(m) \tag{103}$$

and

$$\bar{\mathbf{z}}(m) = \mathbf{A}(m) \mathbf{W}_k \mathbf{d}_z(m) + \mathbf{D}_A(m) \mathbf{W}_k \mathbf{z}(m) + \mathbf{d}_b(m) \tag{104}$$

and setting the derivative with respect to $\epsilon(m)$ in (102) to zero yields

$$\begin{aligned}
0 = & \left[2 \cdot \frac{1}{\sigma_n^2} \sum_{k=1}^P (\bar{\mathbf{d}}(m)^T \bar{\mathbf{d}}(m)) \right] \cdot \epsilon(m)^3 + \left[-3 \cdot \frac{1}{\sigma_n^2} \sum_{k=1}^P (\bar{\mathbf{d}}(m)^T \bar{\mathbf{z}}(m)) \right] \cdot \epsilon(m)^2 \\
& + \left[\frac{1}{\sigma_n^2} \sum_{k=1}^P \left(\bar{\mathbf{z}}(m)^T \bar{\mathbf{z}}(m) - 2 \cdot \bar{\mathbf{y}}(m)^T \bar{\mathbf{d}}(m) \right) + \mathbf{d}_z(m)^T \mathbf{C}_z^{-1} \mathbf{d}_z(m) + \frac{1}{\sigma_a^2} \mathbf{d}_a(m)^T \mathbf{d}_a(m) + \frac{1}{\sigma_b^2} \mathbf{d}_b(m)^T \mathbf{d}_b(m) \right] \cdot \epsilon(m) \\
& + \frac{1}{\sigma_n^2} \sum_{k=1}^P (\bar{\mathbf{y}}(m)^T \bar{\mathbf{z}}(m)) - \mathbf{z}(m)^T \mathbf{C}_z^{-1} \mathbf{d}_z(m) - \frac{1}{\sigma_a^2} (\mathbf{a}(m) - \mathbf{1})^T \mathbf{d}_a(m) - \frac{1}{\sigma_b^2} \mathbf{b}(m)^T \mathbf{d}_b(m)
\end{aligned} \tag{105}$$

Equation (105) has three solutions, two of which are imaginary and one of which is real.

The real solution is chosen as the step size, and the conjugate-gradient update is performed using Equations (87), (88), and (89).

This process is continued until the cost changes by less than a predetermined percentage or until a maximum number of iterations is reached.

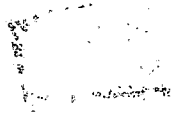
BIBLIOGRAPHY

1. D. Scribner, M. Kruer, and J. Killiany, "Infrared Focal Plane Array Technology," *Proceedings of the IEEE*, Vol. 79, pp. 66-85, 1991.
2. W. Gross, T. Hierl, and M. Schultz, "Correctability and long-term stability of infrared focal plane arrays," *Optical Engineering*, vol. 38, pp. 862-869, 1999.
3. D. Perry and E. Dereniak, "Linear theory of nonuniformity correction in infrared staring sensors," *Optical Engineering*, vol. 32, pp. 1854-1859, 1993.
4. M. Nelson, J. Johnson, and T. Lomheim, "General noise processes in hybrid infrared focal plane arrays," *Optical Engineering*, vol. 30, pp. 1682-1700, 1991.
5. R. C. Hardie and D. R. Droege, "A MAP Estimator for Simultaneous Super-Resolution and Detector Nonuniformity Correction," *EURASIP Journal on Applied Signal Processing*, Vol. 2007, Article ID 89354, (11 pages).
6. P. M. Narendra and N. A. Foss, "Shutterless fixed pattern noise correction for infrared imaging arrays," *Proceedings of the SPIE-International Society of Optical Engineering, Technical Issues in Focal Plane Development*, vol. 282, pp. 44-51, 1981.
7. J. G. Harris, "Continuous-time calibration of VLSI sensors for gain and offset variations," *Proceedings of the SPIE International Symposium on Aerospace and Dual-Use Photonics, Smart Focal Plane Arrays and Focal Plane Array Testing*, M. Wigdor and M. A. Massie, eds., vol. 2474, pp. 23-33, 1995.
8. J. G. Harris and Y.-M. Chiang, "Nonuniformity correction using constant average statistics constraint: Analog and digital implementations," *Proceedings of the SPIE Aerospace/Defense Sensing and Controls, 1997, Infrared Technology and Applications XXIII*, B. F. Anderson and M. Strojnik, eds., vol. 3061, pp. 895-905, 1997.
9. Y.-M. Chiang and J. G. Harris, "An analog integrated circuit for continuous-time gain and offset calibration of sensor arrays," *J. Analog Integr. Circuits Signal Process.*, vol. 12, pp. 231-238, 1997.
10. D. A. Scribner, K. A. Sarkady, J. T. Caulfield, M. R. Kruer, G. Katz, C. J. Gridley, and C. Herman, "Nonuniformity correction for staring focal plane arrays using scene-based techniques," in *Proceedings of the SPIE: Infrared Detectors and Focal Plane Arrays*, E. L. Dereniak and R. E. Sampson, Eds., vol. 1308. The International Society for Optical Engineering, Sept. 1990, pp. 224-233.
11. D. A. Scribner, K. A. Sarkady, M. R. Kruer, J. T. Caulfield, J. D. Hunt, and C. Herman, "Adaptive nonuniformity correction for IR focal plane arrays using neural networks," in

- Proceedings of the SPIE: Infrared Sensors: Detectors, Electronics, and Signal Processing*, T. S. Jayadev, Ed., vol. 1541. The International Society for Optical Engineering, Nov. 1991, pp. 100–109.
12. D. A. Scribner, K. A. Sarkady, M. R. Kruer, J. T. Caulfield, J. Hunt, M. Colbert, and M. Descour, "Adaptive retina-like preprocessing for imaging detector arrays," vol. 3. San Francisco, CA: IEEE International Conference on Neural Networks, Feb. 1993, pp. 1955–1960.
 13. B. Narayanan, R. C. Hardie, and R. A. Muse, "Scene-based nonuniformity correction technique that exploits knowledge of the focal-plane array readout architecture," *Applied Optics*, vol. 44, no. 17, pp. 3482–3491, June 2005.
 14. R. C. Hardie and M. M. Hayat, "A nonlinear-filter based approach to detector nonuniformity correction," in *Proceedings of the IEEE: Nonlinear Signal and Image Processing*, vol. 79, no. 1. Institute of Electrical and Electronic Engineers, pp. 66–85, June 2001, invited.
 15. M. M. Hayat, S. N. Torres, E. Armstrong, S. C. Cain, and B. Yasuda, "Statistical algorithm for nonuniformity correction in focal-plane arrays," *Applied Optics*, vol. 38, pp. 772–780, Mar. 1999.
 16. S. N. Torres and M. M. Hayat, "Kalman filtering for adaptive nonuniformity correction in infrared focal plane arrays," *Journal of the Optical Society of America A*, vol. 20, no. 3, pp. 470–480, Mar. 2003.
 17. R. Hardie, M. Hayat, E. Armstrong, and B. Yasuda, "Scene-based nonuniformity correction with video sequences and registration," *Applied Optics*, vol. 39, no. 8, pp. 1241–1250, Mar. 2000.
 18. B. M. Ratliff, M. M. Hayat, and R. C. Hardie, "An algebraic algorithm for nonuniformity correction in focal plane arrays," *Journal of the Optical Society of America A*, vol. 19, no. 9, pp. 1737–1747, Sept. 2002.
 19. B. M. Ratliff, M. M. Hayat, and J. S. Tyo, "Radiometrically accurate scene-based nonuniformity correction for array sensors," *Journal of the Optical Society of America A*, vol. 20, no. 10, pp. 1890–1899, Oct. 2003.
 20. B. M. Ratliff, M. M. Hayat, and J. Tyo, "Generalized algebraic nonuniformity correction algorithm," *Journal of the Optical Society of America A*, vol. 22, no. 2, pp. 239–249, 2005.
 21. U. Sakoglu, R. C. Hardie, M. M. Hayat, B. M. Ratliff, and J. S. Tyo, "An algebraic restoration method for estimating fixed-pattern noise in infrared imagery from a video sequence," in *49th Annual Meeting of the SPIE: Applications of Digital Image Processing XXVII*, pp. 69–79.
 22. W. F. O'Neil, "Dithered scan detector compensation," *Proceedings of the 1993 Meeting of the Infrared Information Symposium (IRIS) Specialty Group on Passive Sensors*, 1993.
 23. W. F. O'Neil, "Experimental verification of dithered scan non-uniformity correction," *Proceedings of the 1996 Meeting of the Infrared Information Symposium (IRIS) Specialty Group on Passive Sensors*, vol. 1, pp. 329–339, 1997.

24. S. Cain, E. Armstrong, and B. Yasuda, "Joint estimation of image, shifts, and nonuniformities from IR images," in *Infrared Information Symposium (IRIS) on Passive Sensors, Infrared Information Analysis Center, ERIM International, Ann Arbor, Mich.*, 1997.
25. S. Cain, E. Armstrong, and B. Yasuda, "Joint estimation of image, shifts, and nonuniformities from IR images," in *Infrared Information Symposium (IRIS) on Passive Sensors, Infrared Information Analysis Center, ERIM International, Ann Arbor, Mich.*, 1997.
26. W. J. Smith, *Modern Optical Engineering*, McGraw-Hill, New York, NY, pp. 160-163, 2000.
27. R. H. Vollmerhausen, *et al.*, "Modeling Sampled Imagers," *The Targeting Task Performance (TPP) Metric*, Technical Report AMSEL-NV-TR-230, Night Vision and Electronic Sensors Directorate, U. S. Army CERCEC, January 2005.
28. S. C. Park, M. K. Park, and M. G. Kang, "Super-resolution image reconstruction: A technical overview," *IEEE Signal Processing Mag.*, pp. 21-36, May 2003.
29. S. Borman, "Topics in multiframe superresolution restoration," Ph.D. Dissertation, University of Notre Dame, April 2004.
30. M. S. Alam, J. G. Bogner, R. C. Hardie and B. J. Yasuda, "Infrared Image Registration and High Resolution Reconstruction Using Multiple Translationally Shifted Aliased Video Frames," *IEEE Transactions on Instrumentation and Measurement*, Vol. 49, 2000, pp. 915-923.
31. B. Narayanan, R. C. Hardie, K. E. Barner, and M. Shao, "A Computationally Efficient Super-Resolution Algorithm for Video Processing Using Partition Filters," to appear in *IEEE Transactions on Circuits and Systems for Video Technology*, April 2007.
32. R. C. Hardie, "Fast Super-Resolution using an Adaptive Wiener Filter," submitted to *IEEE Transactions on Image Processing*, May 2007 (in review).
33. J. M. Schuler and D. A. Scribner, "Increasing Spatial Resolution Through Temporal Super-Sampling of Digital Video," *Optical Engineering*, Vol. 38, 1999, pp. 801-805.
34. R. R. Schultz and R. L. Stevenson, "A Bayesian approach to image extension for improved definition," *IEEE Trans. Image Processing*, vol. 3, no. 3, pp. 233-242, May 1994.
35. P. Cheeseman, B. Kanefsky, R. Kraft, J. Stutz, and R. Hanson, "Super-resolved surface reconstruction from multiple images," NASA Tech. Rep. FIA-94-12, Moffett Field, CA, Dec 1994.
36. R. R. Schultz and R. L. Stevenson, "A Bayesian approach to image expansion for improved definition," *IEEE Transactions on Image Processing*, vol. 3, no. 3, pp. 233-242, May 1994.
37. S. C. Cain, R. C. Hardie, and E. E. Armstrong, "Restoration of aliased video sequences via a maximum-likelihood approach," in *National Infrared Information Symposium (IRIS) on Passive Sensors*, Monterey, CA, Mar. 1996.
38. R. C. Hardie, K. J. Barnard, and E. E. Armstrong, "Joint MAP registration and high-resolution image estimation using a sequence of undersampled images," *IEEE Trans. Image Processing*, vol. 6, no. 12, pp. 1621-1633, Dec 1997.

R702034455



39. R. C. Hardie, K. J. Barnard, J. G. Bogner, E. E. Armstrong, and E. A. Watson, "High resolution image reconstruction from a sequence of rotated and translated frames and its application to an infrared imaging system," *Optical Engineering*, vol. 37, no. 1, pp. 247-260, Jan. 1998.
40. M. Irani and S. Peleg, "Improving resolution by image registration," *CVGIP: Graphical Models and Image Processing*, vol. 53, no. 3, pp. 231-239, May 1991.
41. E. E. Armstrong, M. M. Hayat, R. C. Hardie, S. N. Torres, and B. J. Yasuda, "Nonuniformity correction for improved registration and high-resolution image reconstruction in IR imagery," in *Proceedings of the SPIE: Applications of Digital Image Processing XXII*, A. G. Tescher, Ed., vol. 3808. The International Society for Optical Engineering, Oct. 1999, pp. 150-161.
42. E. E. Armstrong, M. M. Hayat, R. C. Hardie, S. Torres, and B. Yasuda, "The advantage of nonuniformity correction pre-processing on infrared image registration," in *Annual Meeting of the SPIE*, ser. Application of Digital Image Processing XXII, Denver, Colorado, July 1999.
43. B. L. Bowerman and R. T. O'Connell, *Linear Statistical Models*, Second Edition, Duxbury Thompson Learning, Pacific Grove, CA, pp. 244-249, 1990.
44. R. Driggers, K. Krapels, S. Murrill, S. Young, M. Thielke, and J. Schuler, "Superresolution performance for undersampled imagers," *Optical Engineering*, 014002-1-9, 2005.
45. S. C. Cain, M. M. Hayat, and E. E. Armstrong, "Projection-based image registration in the presence of fixed-pattern noise," *IEEE Transactions on Image Processing*, vol. 10, no. 12, pp. 1860-1872, Dec. 2001.